Relevance of star-disc encounters in massive stellar clusters

-

From gas-embedded to dissolving populations

INAUGURAL-DISSERTATION

zur
Erlangung des Doktorgrades
der Mathematisch-Naturwissenschaftlichen Fakultät
der Universität zu Köln

vorgelegt von
Manuel Steinhausen
aus Solingen

Max-Planck-Institut für Radioastronomie Bonn
2013

Berichterstatter/in: Prof. Dr. Susanne Pfalzner ....

Prof. Dr. Joachim Krug ....

Tag der mündlichen Prüfung: 14. Mai 2013

Zusammenfassung

Die aktuelle Vorstellung von Sternenstehung besagt, dass Sterne nicht einzeln sondern bevorzugt in Sternhaufen entstehen. Als Folge des Entstehungsprozesses sind die jungen Sterne anfänglich von zirkumstellaren Scheiben umgeben, welche aus Staub und Gas bestehen. Bisherige Untersuchungen des Einflusses von Vorbeiflügen anderer Sternhaufenmitglieder auf diese Scheiben konzentrierten sich ausschließlich auf die frühe Phase der Sternhaufenentwicklung ($<$ 3 Millionen Jahre), während der die Sterne noch im Gas aus der Entstehungsphase eingebettet sind. In dieser Arbeit wurde der Einfluss eines störenden Sterns auf das Stern-Scheibe System während der *gesamten* ersten 15 Millionen Jahre der Entwicklung untersucht, also nicht nur die frühe, eingebettete Phase sondern auch die Expansionsphase des Sternhaufens nach dem Ausstoß des umgebenden Restgases.

Für die eingebettete Phase wurden speziell die Auswirkungen unterschiedlicher Massenverteilungen innerhalb der Scheiben auf Verluste durch Sternvorbeiflüge untersucht. Obwohl der Einfluss der Massenverteilung auf die Scheibenverluste in Einzelstößen sich teilweise stark unterscheidet, ist die Anzahl der Sterne mit gestörten Scheiben im Sternhaufen weitesgehend unabhängig vom anfänglichen Dichteprofil. Die Ausnahme bilden sehr dichte Sternhaufen, bei denen Scheibenmasseverluste in den Kernregionen von 40% für steile Masseverteilungen denen von 60% für anfänglich flache Masseverteilungen gegenüber stehen. Der Grund liegt in der Dominanz der massearmen Sterne in diesen Sternhaufen, welche aufgrund ihrer üblicherweise massiveren Stoßpartner die größte Abhängigkeit von der anfänglichen Massenverteilung zeigen.

Nachdem das Restgas aus dem Sternhaufen ausgestoßen wurde, verringert sich dessen stellare Dichte schnell. Dabei dehnt sich die dichte Kernregion um einen Faktor *zehn* aus und die Sterne des dünn bevölkerten, äußeren Randes verlassen den Sternhaufen. Somit nimmt die Zahl der Stöße deutlich ab und im Allgemeinen werden nur noch sehr wenige Scheiben während dieser Phase zerstört.

Eine Folge dieser dynamischen Entwicklung ist, dass die große Menge der stellaren Stöße in der Kernregion von eingebetteten Sternhaufen deutlich die beobachtete Scheibenhäufigkeit der im Sternhaufen verbleibenden Sterne prägt und somit eine nicht vorhandene Abnahme der Scheibenhäufigkeit mit dem Sternhaufenalter suggeriert. Der große Anteil der Sterne, die den Sternhaufen verlassen und in die Feldpopulation übergehen, wird wenig von den umliegenden Sternen beeinflusst, wodurch Planetenbildung in diesen Scheiben wesentlich begünstigt ist.

Abstract

Observations reveal that most stars do not form in isolation but as part of a star cluster. Initially, the young stars constituting these clusters are surrounded by circumstellar discs. Previous investigations concentrated on the consequences of stellar interactions for these circumstellar discs during the early phases (< 3 Myr), where the cluster is still embedded in its natal gas. By contrast, the relevance of star-disc encounters during the *entire* first 15 Myr of massive cluster development has been investigated in this work, including the gas-embedded and the cluster expansion phase.

In the embedded phase, the focus was on the influence of the initial shape of the disc-mass distribution. Although it has a significant impact on the relative disc-mass and angular momentum losses in certain single star-disc encounters, the fraction of stars with perturbed discs turns out to be fairly unaffected by the initial density profile. The exception are dense cluster environments, where disc destruction rates in the crowded core regions are 40% and 60% for steep and shallow disc-mass distributions, respectively. Here, the interactions of low-mass stars dominate, which show the largest dependency on the initial disc-mass distribution due to the generally high encounter mass ratios.

After the expulsion of the residual gas the stellar density drops rapidly so that the number of encounters is considerably lower, and very few discs are completely destroyed. The dense cluster core region expands by a factor of ten while most of the stars in the sparse cluster outskirts become unbound. A consequence of this cluster expansion is that the multitude of stellar encounters in the core regions of embedded clusters significantly shapes the disc properties of the remnant bound population, whereas the stars joining the field population are to a much lesser degree affected by encounters.

The expansion process strongly influences the observed disc fractions since it mimics a non-existent decrease with cluster age. Stars that are dispersed in the field most likely maintain their discs for a substantially prolonged time span and are, thus, more suitable for forming planetary systems.

Contents

1 Introduction

In accordance with currently accepted star formation scenarios, observations show that most, if not all, stars are initially surrounded by a circumstellar disc. There is increasing observational evidence that with time these discs become depleted of gas and dust and eventually disappear. A variety of physical mechanisms have been found to contribute to this evolutionary process, one of them gravitational star-disc interactions. In contrast to previous investigations of such stellar encounters (Clarke & Pringle, 1993; Hall *et al.*, 1996; Boffin *et al.*, 1998; Pfalzner, 2004; Olczak *et al.*, 2006) this study involves the treatment of arbitrary disc-mass distributions for the circumstellar discs. Due to the implementation of a flexible numerical scheme this is realized without the need for explicit simulations of the entire parameter space.

The importance of stellar encounters is induced by the fact that most young stars do not form in isolation but as part of a cluster environment. In general only a minor fraction of the Giant Molecular Cloud Complexes is converted into stars, which results in a protostellar cluster population that is initially surrounded by its natal gas. The residual gas is expelled by stellar winds, UV radiation and early supernova explosions of the massive stars within remarkably short timescales. Due to the gas expulsion the binding energy of the cluster is significantly reduced and the cluster starts to expand. On average, 90% of the clusters are completely dispersed into the field after about 10 Myr, only a small fraction remains bound as a stellar cluster (Lada & Lada, 2003). Even though this expansion plays an important role in the cluster evolution, the effect of stellar encounters under the predetermined conditions of an expanding cluster environment has not been treated so far. In the second part of the thesis, the importance of stellar encounters in such varying cluster environments will be investigated for different initial disc-mass distributions.

After about 10 Myr an average of 90% of clusters are completely dispersed into the field while only a small fraction remains bound as a stellar cluster (Lada & Lada, 2003). However, the effect of stellar encounters under the predetermined conditions of an expanding cluster environment has not been treated so far. The focus in the second part of the thesis is on the gravitational interactions of stellar members in such varying cluster environments.

Moreover, an evolutionary sequence for the density-radius relation of the most massive clusters in the Solar neighbourhood ($M_{\text{cluster}} > 10^3\,\mathrm{M}_{\odot}$) has been recently established by

Pfalzner (2009). The gas-embedded stellar populations expand rapidly during and after the gas is expelled ending up as sparse (leaky) OB associations after > 20 Myr. Here, for the first time the influence of such expanding cluster environments on stellar encounters will be presented. Various gas expulsion models have been configured that account for the different evolutionary phases of the stellar populations.

The aim of this work is to obtain an insight in the relevance of stellar encounters in authentic cluster environments.

1.1 Isolated star formation

The formation process of a single star is relatively well understood. The generally accepted picture begins with the collapse of a cold molecular cloud and ends when the star has stopped accreting its circumstellar material, entering the so-called zero-age main sequence (ZAMS). This period is very short compared to the entire lifetime of a star, given by

$$\text{lifetime} \approx 10^4 \left(\frac{m_\text{star}}{\mathrm{M}_\odot}\right)^{-2.5} \text{Myr.} \tag{1.1}$$

where the m_star is the stellar mass given in $\mathrm{M}_\odot$.

The youth of stars was suggested by their concentration near associations of high-mass stars. These have to be necessarily young (Ambartsumian, 1954), because due to their high masses and consequently high gravitational pressure the hydrogen burning will only last for a few Myrs. So the presence of high-mass stars demonstrates that star formation is an ongoing process in our Galaxy.

In Figure 1.1 a sketch of the star formation process including timescales and size relations is shown. Observations have found that giant molecular clouds (GMCs) with masses of $10^2 - 10^6$ $\mathrm{M}_\odot$, temperatures of $10 - 20$ K and sizes of $10 - 100$ pc (Larson, 2003) are potential sites of star formation. They are concentrated in the spiral arms of galaxies, surrounded by less dense envelopes of atomic gas. Molecular clouds with a mean density of $\approx 100\, H_2$ molecules per cm^3 (Blitz, 1993), entail atomic hydrogen to preferentially associate into molecular hydrogen H_2 ($\sim 90\%$), but there are also some other molecular structures found like CO_2. The abundance of molecules is strongly dependent on their formation rate on the surface of dust grains and thus increases with density. The formation of a star from a molecular cloud requires the resisting forces of turbulent motion, thermal gas pressure and magnetic fields to be smaller than the gravitational forces. Thus in particular the cold and dense molecular cloud regions are potential seeds for the star formation processes (Fig. 1.1a).

Such molecular clouds are typically of very low density, which means that they have to contract by a factor of several magnitudes to form a star. This enormous reduction in size means that any small initial rotation of the star-forming cloud results in large angular velocities due to angular momentum conservation, eventually causing the formation of a planetary disc. In summary, molecular clouds are transient structures that form, evolve and disperse very quickly, all in a time comparable to ~ 10 Myr (Hartmann, 2003; Elmegreen, 2000).

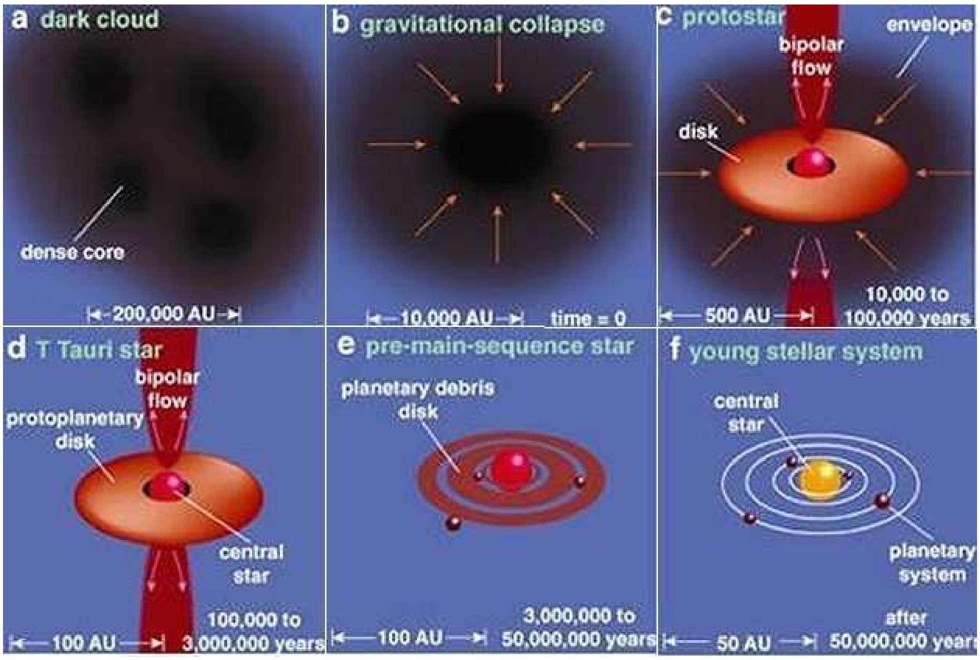

FIGURE 1.1: The process of star formation. Taken from Greene (2001).

The gravitational instabilities of the molecular cloud are a prerequisite for the formation of so-called *protostars*. The mass necessary to obtain such gravitationally unstable density fluctuations is the *Jeans mass*:

$$M_J = 5.57c^3\sqrt{\frac{\rho}{G^3}} \tag{1.2}$$

with the isothermal sound speed c and uniform density ρ. The Jeans instability leads to the formation of a core that starts to accrete material from the surrounding envelope (Fig. 1.1b). The accompanying release of kinetic energy heats the medium so that temperature and pressure at the center of the protostar increase. As its temperature approaches thousands of degrees, the protostar becomes visible as an infrared source.

During the initial collapse, the clump is transparent to its own radiation and the collapse proceeds rather quickly. With increasing density the clump becomes opaque, restraining the energy loss by infrared radiation. As a result, temperature and pressure in its center will start to ascend. At some point, the pressure stops the infall of gas onto the core and the object becomes temporarily stable as a protostar (Fig. 1.1c). The protostar has initially about 1% of the final stellar mass and continues growing by accreting material from the envelope via its protostellar disc.

One consequence of the collapse is that these evolved young stars, in case of $m_1 \leq 2\,\mathrm{M}_\odot$ known as T Tauri stars, are usually surrounded by massive, opaque circumstellar discs (Fig. 1.1d). Although the envelope disappears quickly - for a solar mass star the protostellar phase lasts about 100 000 yrs - disc material can still be accreted onto the stellar surface.

As a by-product of the star formation process planets might form from the debris circumstellar disc. Such pre-main sequence (PMS, Fig. 1.1e) stars radiate energy both from the heated disc mainly in the infrared and from the accretion of material onto the stellar surface at optical and ultraviolet wavelengths. A fraction of the material accreted onto the star is ejected perpendicular to the disk plane in a highly collimated stellar jet. A PMS star can lose up to 50% of its mass before reaching the main sequence.

This occurs typically after a few million years when thermonuclear fusion begins in the core and a strong stellar wind is produced which stops the infall of new mass. Since the circumstellar disc eventually dissipates, there must be other mechanisms to remove angular momentum from the disc. For example the formation of planets (Fig. 1.1f), binary or multiple systems or interactions with the stellar environment (Larson, 2009) are possible explanations.

1.2 Structure of circumstellar discs

There is increasing observational evidence that most, if not all, stars are initially surrounded by a circumstellar disc consisting of gas and dust. In the past decades such discs have been detected from optical, infrared and millimeter photometry of young stars. Measurements of long-wavelength bands showed an excess of emission above that expected from the stellar photosphere. This excess was interpreted as radiation emitted by a disc-like structure, which is heated via reprocessing of the central star's light and accretion luminosity.

The most efficient way to observe stellar discs is examining the L-band excess (Haisch *et al.*, 2001b), which refers to the near infrared. For example, Lada *et al.* (2000) found with this method a fraction of $80 - 85\%$ of all stars in the Trapezium cluster to be surrounded by discs. Here, the observed wavelength regime is of major importance since it restricts the observations to a certain part (temperature) within the disc.

Figure 1.2 illustrates the wavelength regions for the spectral energy distribution (SED) of a flaring protoplanetary disc. The model indicates a near-infrared bump due to the inner rim of the disc, infrared dust features from the warm surface layer, and the underlying continuum emission from the deeper (cooler) disc regions. Typically the near- and mid-

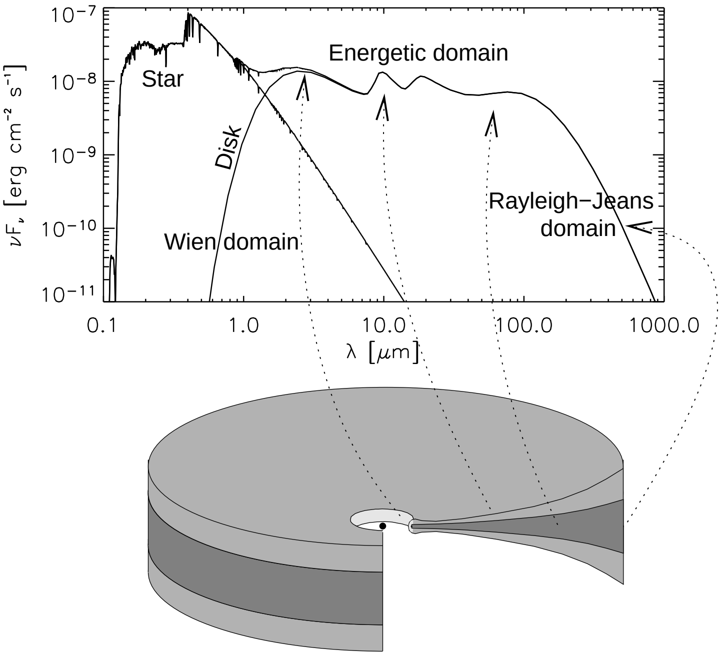

FIGURE 1.2: Build-up of the SED of a flaring protoplanetary disc ($r_{\mathrm{disc}} = 100\,\mathrm{AU}$). Scattering is not included here (Dullemond *et al.*, 2007).

infrared emission originate from small radii, while the far-infrared comes from the outer disc regions. The (sub-)millimeter radiation is mostly emitted from the mid-plane of the outer disc. Most observations are performed with the *Spitzer Space Telescope* and limited to $< 10\,\mathrm{AU}$ from the central star while a few discs in the Orion Nebula Cluster have been resolved beyond 50 AU in the optical with the *Hubble Space Telescope*. Recently, the ground-based *Atacama Large Millimeter Array* (ALMA) program started, which will focus on millimeter and sub-millimeter wavelengths and, thus, the more distant regions of circumstellar discs. In fact, a much lower disc fraction is found on scales of $> 50\,\mathrm{AU}$ compared to observations within distances of less than a few AU to the central star (e.g. Clarke, 2007).

Disc-mass distribution

To date, observational limitations have prevented a determination of the typical surface density of protoplanetary discs and its temporal development. This means a unique predetermined initial state for the disc-mass distribution is not well known. A wide variety of surface densities have been derived by fitting resolved millimeter continuum or line emission data with parametric disc structure models (e.g. Mundy *et al.*, 1996; Lay *et al.*, 1997) or in combination with broadband spectral energy distributions (SEDs) (Wilner *et al.*, 2000;

Testi *et al.*, 2001; Akeson *et al.*, 2002; Kitamura *et al.*, 2002; Andrews & Williams, 2007b). While those studies have profoundly shaped our knowledge of disc structures, all have fundamentally been limited by the low angular resolution of available data.

The standard fitting method is based on the assumption that the surface density Σ has a simple power-law dependence of the form

$$\Sigma(r) \propto r^{-p}, \tag{1.3}$$

out to some cut-off radius (e.g. Andrews & Williams, 2007a). Estimates based on numerical power-law models fitted to observational data lead to distribution indices p ranging roughly from $p = 0$ to $p = 2$. Recent studies have found even unexpected results, e.g. Isella *et al.* (2009) who measured distribution indices of $p < 0$.

Many theoretical studies use a crude approximation of the primordial solar disc (the Minimum Mass Solar Nebula, or MMSN) as a reference point, which is constructed by augmenting the current planet masses to match solar abundances, and then smearing those masses into concentric annuli. The result is fitted with a radial power law, $\Sigma \propto r^{-1.5}$ (Weidenschilling, 1977). Recently, Chiang & Laughlin (2012) determined a similar result for the Minimum Mass Extrasolar Nebula (MMEN) constructed from the Kepler catalog of extrasolar planets. They find a slightly steeper surface-density distribution, $\Sigma \propto r^{-1.6}$.

Analytical approaches also propose different disc-mass distribution indices. The most widely used model is that of a steady-state viscous accretion disc with a surface density distribution index of $p = 1$ (e.g. Hartmann *et al.*, 1998). However, simulations of the evolution of protostellar discs that form self-consistently from the collapse of a molecular cloud core yield a surface distribution index of $p = 1.5$ (Lin & Pringle, 1990; Hueso & Guillot, 2005; Vorobyov & Basu, 2007), while studies that include magnetised disc material have found a flatter disc-mass distribution of $p = 0.75$ (Shu *et al.*, 2007).

Despite the large range of existing distribution parameters upcoming observational results from *ALMA* will potentially provide further insights on the disc structures.

1.3 Dissolution of the circumstellar discs

With time, the protoplanetary discs surrounding new born stars become depleted of gas and dust and eventually disappear (Haisch *et al.*, 2001b; Hillenbrand, 2002; Sicilia-Aguilar *et al.*, 2006; Hernández *et al.*, 2007; Currie *et al.*, 2008; Hernández *et al.*, 2008; Mamajek, 2009; Massi *et al.*, 2010). The remnant circumstellar material will either be accreted onto its central star, dispersed into the interstellar medium, or aggregated to large protoplanetary bodies. In Figure 1.3 the disc fraction in stellar clusters, which are conglomerations of thousands of stars, are shown as a function of the mean cluster age. The cluster disc fraction (CDF) is a fundamental quantity, which is defined by the number of disc-less stars divided by the total number of stars and is often used as a global tracer of a clusters dynamical state. In general, observations indicate a strong decrease of the cluster disc fraction with increasing cluster age. Most of the discs are completely dissolved after about 6 Myr.

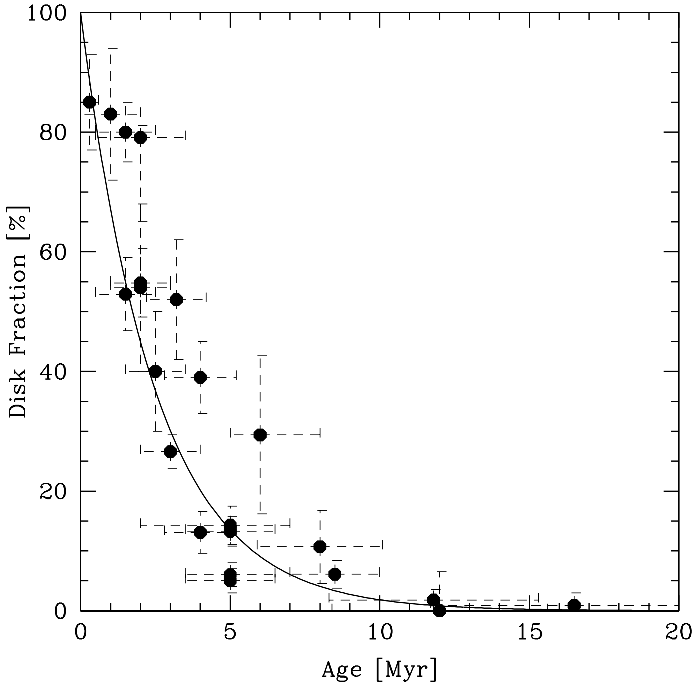

FIGURE 1.3: Cluster disc fraction as a function of the cluster age. The solid line shows an exponential fit. The Figure and data references are taken from Mamajek (2009).

The cluster disc fraction is not only a function of the cluster age but depends likewise on the stellar mass of the disc-surrounded star, the binary fraction, and the cluster density. Uniform observations of these effects are rather challenging, due to the large distances of even the nearest star forming regions ($>$ 100 pc Wilking *et al.*, 2008) and drastic observational limitations. In most cases the clusters are still embedded in their natal gas and, therefore, observations are restricted to long wavelength selections and sub-samples of the brighter high-mass stars, which are preferentially located in the central cluster regions.

Despite these limitations, it was found that disc lifetimes decrease for higher stellar masses (Hillenbrand *et al.*, 1992; Lada *et al.*, 2000; Stolte *et al.*, 2004; Carpenter *et al.*, 2006; Lada *et al.*, 2006; Kennedy & Kenyon, 2009) with dispersion timescales of only a few 10^5 yr for pre-main sequence stars of $2-8\,M_\odot$ - so-called Herbig Ae/Be stars (Alonso-Albi *et al.*, 2009). Kennedy & Kenyon (2009) analysed stellar disc fractions in nine young clusters by observing the infrared excess, a tracer for circumstellar discs heated by the central star,

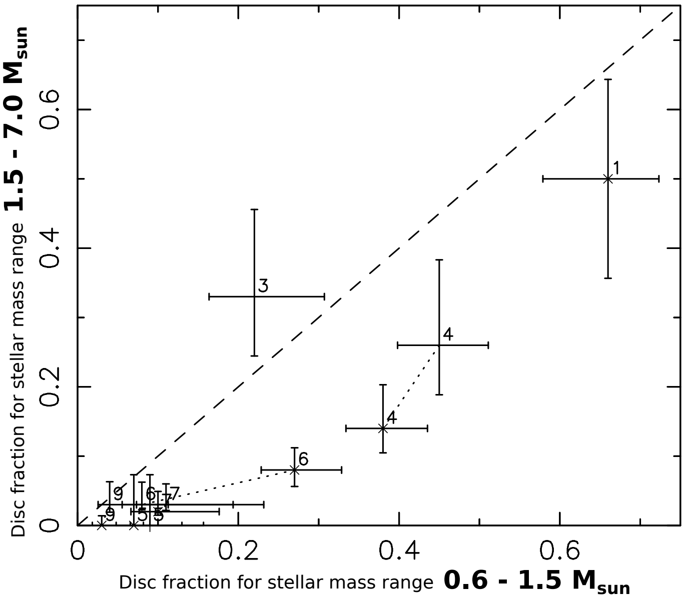

FIGURE 1.4: Shown are the disc fractions according to accretion signatures (×) and infrared excess (+) for two stellar mass bins. The dashed line indicates an equal disc fraction for the mass bins. The data results from observations of (1) Taurus, (3) IC348, (4) Tr37, (5) NGC2362, (6) OB1bc, (7) UpperSco, and (9) NGC7160 are presented. The Figure has been adapted from Kennedy & Kenyon (2009).

and the equivalent widths of Hα emission, which is a signature for accretion. Figure 1.4 shows their results by comparing the disc fraction of sun-like stars ($0.6 - 1.5\,M_\odot$) to the disc fraction of stars $> 1.5\,M_\odot$, using an equivalent number of stars for each mass bin. It can be seen that circumstellar discs around sun-like stars seem to survive longer than discs around high-mass stars. For lower masses they find no significant deviations. However, in other cases the disc fraction seems to decline towards very low stellar masses (Lada *et al.*, 2004, 2006; Oliveira *et al.*, 2006), which is mostly interpreted as sun-like stars providing the most favorable conditions for planet formation. Note that due to the large error ranges for disc fractions of low-mass stars these results have to be treated with caution.

Another significant influence on the cluster disc fraction is provided by binary or multiple stellar systems. Bouwman *et al.* (2006) found much shorter lifetimes of circumstellar discs around stars that are part of a binary system than those for single stars. According to their investigation the mean disc dissipation time for binaries is found to be about 5 Myr while discs around single stars survive roughly 9 Myr. Furthermore, Cieza *et al.* (2009) distinguished between tight and loose binary systems. They observed twice as much discs around binary systems with separations of $40 - 400\,$AU compared to the number of discs around *hard* binaries with separations $< 40\,$AU.

Furthermore, observations reveal that the cluster disc fraction depends strongly on the cluster density. Luhman *et al.* (2008) compare the disc fraction of the sparse cluster Chamaeleon I to the one of the denser stellar population of IC 348, both with cluster ages of about 2.5 Myr. For masses $> 1\,M_\odot$ they found significantly less dissolved discs in Chamaeleon I. Hence, they concluded a decreasing disc lifetime for high-density star forming regions.

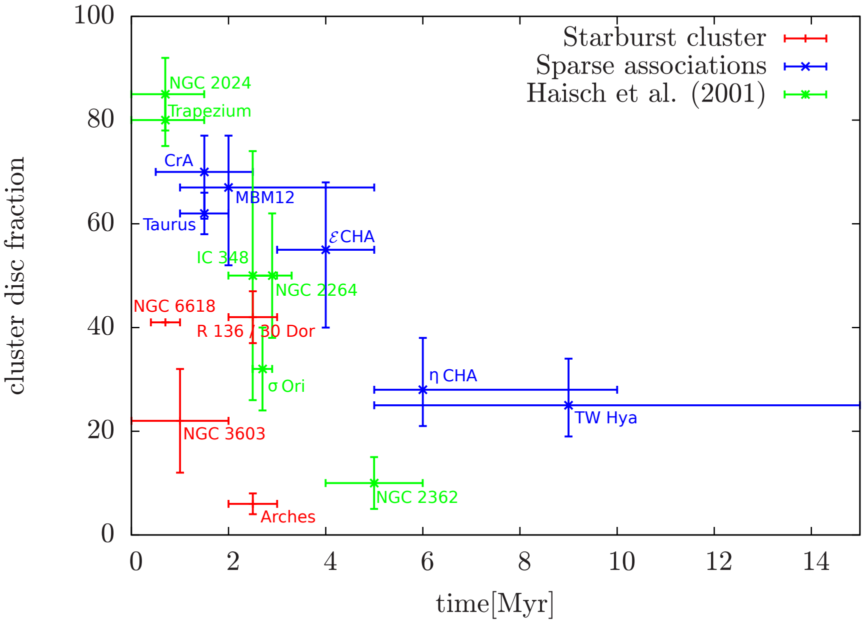

FIGURE 1.5: Shown is the cluster disc fraction as a function of the cluster age in Myr. The values for the starburst clusters (red) are taken from Stolte *et al.* (2010) (and references therein) while the sparse associations (blue) are taken from Fang *et al.* (2013) (and references therein). The remaining data points are taken from the sequence found by Haisch *et al.* (2001b) (and references therein). In most of the previous cases minor or even no errors have been specified for the cluster ages and disc fractions. Taking into account additional observations by several authors (Casey *et al.*, 1998; Webb *et al.*, 1999; Weintraub *et al.*, 2000; Sung & Bessell, 2004; Nisini *et al.*, 2005; Meyer & Wilking, 2009; Currie & Sicilia-Aguilar, 2011; Kudryavtseva *et al.*, 2012) the error bar estimates have been improved and now reflect an increased parameter range.

This would also suggest a spatial dependence of observational results. Stolte *et al.* (2010) surveyed the cluster disc fraction of B-type stars in the Arches cluster, one of the densest stellar populations in the Milky Way ($\rho_{\mathrm{core}} > 10^5\,M_\odot\,\mathrm{pc}^{-3}$) containing > 100 O-type stars (Figer *et al.*, 2002). They found a strong dependence of the disc fraction on the radial distance from the dense cluster center with an increasing excess fraction for larger radii. Similar results have been obtained for the starburst cluster NGC 3603 where the disc fraction increases with radius from 20% ($r < 0.6\,\mathrm{pc}$) to 40% ($0.8 < r < 1\,\mathrm{pc}$) (Stolte *et al.*, 2004). Similar results have been obtained for stellar populations in the Solar neighbourhood, like the Orion Nebula Cluster (Hillenbrand *et al.*, 1998).

In Figure 1.5 a combination of the established cluster disc fraction from Haisch *et al.* (2001b), Stolte *et al.* (2010) for massive compact starburst clusters, and the recently published results from Fang *et al.* (2013) representing sparse associations are shown as a function of the cluster age. Error estimates have been considerably improved by seeking for additional observational age and disc fraction data in the literature (see caption of Fig. 1.5). Apart from the generally expected decline of the cluster disc fraction with time, a significant difference in the slope emerges for the plotted density groups. The red data points represent the scope of the starburst clusters in which the circumstellar discs disperse very quickly (< 4 Myr). Stolte *et al.* (2010) interpreted these findings as a result of the high masses of the stars in their sample. Note, that the disc fraction of the inner core of 30 Doradus has not been resolved, which implies that the shown disc fraction might be an upper limit. While the data by Haisch *et al.* (2001b) is dominated by low-mass stars, starburst cluster observations are mostly limited to OB-type stars, due to their high densities and large distances. Fang *et al.* (2013) presented a study of sparse stellar associations covering various stellar mass ranges. As shown in Figure 1.5 by the blue crosses the cluster disc fractions of these stellar populations decrease much slower than the previous. After 6 Myr it is unclear if the discs will completely disappear or if a fraction of around 20% will maintain. Regardless of the stellar mass a dependence of the cluster disc fraction on the cluster density can be identified. While in dense clusters the discs disappear within a few Myr, circumstellar discs in sparse associations might survive for at least 10 Myr.

1.4 Interactions with the stellar environment

It is currently unclear which physical mechanism dominates the evolutionary disc destruction processes. Among the great variety of effects are internal processes such as viscous torques (e.g. Shu *et al.*, 1987), turbulent effects (Klahr & Bodenheimer, 2003), and magnetic fields (Balbus & Hawley, 2002), but as well external disc destruction processes like photoevaporation (Scally & Clarke, 2001; Clarke *et al.*, 2001; Matsuyama *et al.*, 2003; Johnstone *et al.*, 2004; Alexander *et al.*, 2005, 2006; Ercolano *et al.*, 2008; Drake *et al.*, 2009; Gorti & Hollenbach, 2009) and tidal interactions (Heller, 1993; Clarke & Pringle, 1993; Ostriker, 1994; Heller, 1995; Hall *et al.*, 1996; Hall, 1997; Larwood, 1997; Boffin *et al.*, 1998; Pfalzner, 2004; Pfalzner *et al.*, 2005a; Moeckel & Bally, 2006; Kley *et al.*, 2008).

Since it is long known that stars form not only in isolation but in stellar populations, like the Orion Nebula Cluster (ONC), star cluster regions became of major importance for studying disc destruction via external processes. Here, investigations seem to indicate that photoevaporation should by far dominate the disc destruction (Scally & Clarke, 2001; Balog *et al.*, 2008). During this process the perturbation of protoplanetary discs results from the UV radiation from massive stars. Hereby, the radiation interacts with the disc matter and thus accelerates preferentially light disc elements outwards. Another significant destruction mechanism, although often discarded as probably unimportant, is the influence on circumstellar discs by stellar encounters, which has already been suggested in the 90s by e.g. Clarke & Pringle (1993); Hall *et al.* (1996); Boffin *et al.* (1998). At that time first numerical simulations of selected stellar fly-by scenarios were performed, which already yielded substantial effects on the shape of the circumstellar discs.

The focus of the present numerical investigation will be on the effect of such gravitational star-disc interactions on the disc-mass distribution and, therefore, the mass and angular momentum of the discs. A star-disc encounter* can cause matter to become unbound, be captured by the perturbing star or pushed inwards and potentially be accreted by the central star. The extent to which this happens depends on the periastron distance, the mass ratio of the stars, the eccentricity and, moreover, the initial (pre-encounter) mass distribution in the disc.

Star-disc encounters with focus on the mass and angular momentum losses due to gravitational interactions in ONC-like cluster models have been reviewed in many investigations prior to this study (Pfalzner, 2004; Olczak *et al.*, 2006; Pfalzner & Olczak, 2007). In particular, Olczak *et al.* (2006) found that star-disc interactions influencing the circumstellar discs are more frequent in the inner core of the ONC than previously assumed (Scally & Clarke, 2001). Moreover, the massive stars act as gravitational focii which results in a rapid destruction of their discs due to multiple perturbations by lighter stars (Olczak *et al.*, 2006; Pfalzner *et al.*, 2006).

However, most previous numerical studies of star-disc encounters have used only a single density distribution, mainly focusing on the case of a theoretically motivated r^{-1} disc-mass distribution (Hall *et al.*, 1996; Hall, 1997; Pfalzner, 2004; Olczak *et al.*, 2006; Moeckel & Bally, 2006; Pfalzner & Olczak, 2007). Star-disc encounters with different initial disc-mass distributions have only been considered in a very limited way. Heller (1995) performed numerical simulations of two different mass distributions ($p = 0$ and $p = 1.5$) concentrating on parabolic encounters with equal mass stars, while Hall (1997) investigated initial surface distributions of $p = 0$ and $p = 1$ for close and penetrating encounters of unity mass ratio. A study of a wide parameter range focusing on multiple initial disc-mass distributions still needs to be performed.

Nevertheless, numerical studies of star-disc encounters only allow a sectional view of the processes since it is impossible to simulate each combination of encounter parameters. Earlier analytical studies by Ostriker (1994) did not suffer from this shortcoming. In

---

[*] Here, the term 'star-disc encounter' describes encounters in which only one of the stars is surrounded by a disc, in contrast to disc-disc encounters, in which both stars are surrounded by discs.

her study, a first order approximation of the angular momentum loss dependent on the initial disc-mass distribution is given. However, the validity of her results is limited to large periastron radii (for example $r_{\text{peri}}/r_{\text{disc}} > 3$ for $M_2/M_1 = 1$), where the angular momentum loss is usually well below 10 %. Close or even penetrating encounters cannot be interpreted by this linear perturbation theory (Ostriker, 1994; Pfalzner *et al.*, 2005b) making numerical studies indispensable in this regime.

Taking the huge variety of observed and theoretical motivated disc-mass distributions into account (Section 1.3), one has to consider different initial disc-mass distributions to evaluate their effect in star-disc encounters. In this work, the effects of star-disc encounters are investigated for a large parameter space considering most configurations that can be expected in a typical young cluster. The investigated mass distributions cover the entire range of the so far observed disc-mass distributions.

1.4.1 The Orion Nebula Cluster

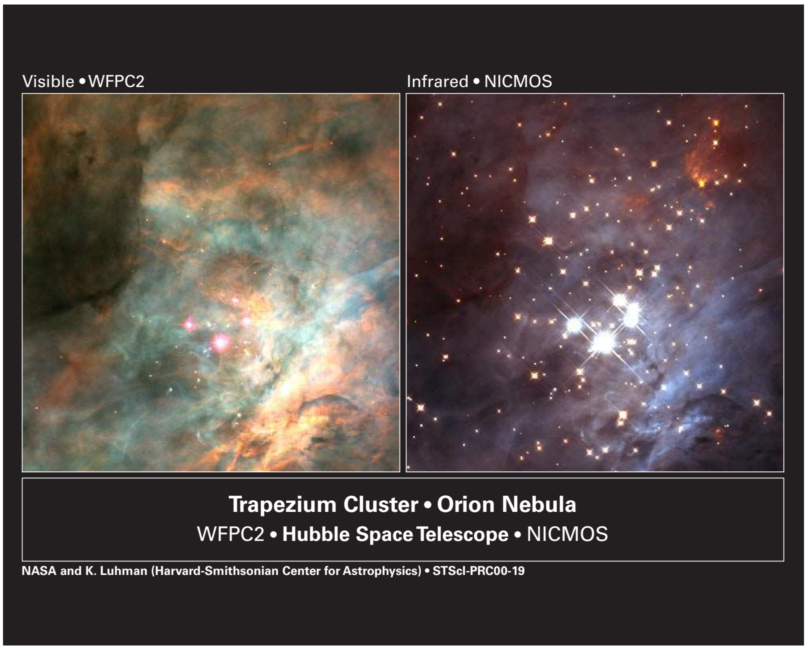

FIGURE 1.6: Two views of the Trapezium cluster in the Orion Nebula from the Hubble Space Telescope. The image on the left, an optical spectrum image taken with Hubble's WFPC2 camera, shows a few stars shrouded in glowing gas and dust. On the right, an image taken with Hubble's NICMOS infrared camera penetrates the haze to reveal a swarm of stars as well as brown dwarfs. The figure is taken from Luhman & O'Dell (2000).

The Orion Nebula Cluster (ONC) has been chosen as one model cluster for our simulations since it is the nearest massive young star cluster and one of the best observed young dense star forming regions. In Figure 1.6 it can be seen that large parts of the cluster are covered by the remnant gas, which prevents extensive observations in the visible regime. However, in the infrared band the star-forming region, which consists of about 4000 stars with masses above the hydrogen-burning limit of $0.08\,\mathrm{M}_\odot$ in a volume of 2.5 pc (Hillenbrand & Hartmann, 1998; Hillenbrand & Carpenter, 2000) and half-mass radius $r_{hm} \approx 1\,\mathrm{pc}$, can be resolved. It is located south of Orion's Belt, along our spiral arm of the Milky Way, at a distance of $414 \pm 7\,\mathrm{pc}$ to our Sun (Sandstrom *et al.*, 2007; Menten *et al.*, 2007) and is part of the Orion Molecular Cloud Complex. The mean age of the cluster has been estimated to be about $1-2$ Myr (Hillenbrand & Hartmann, 1998; Palla & Stahler, 1999). Most of the stars have already been formed and the residual gas has been ejected to the outer parts.

Besides most of its objects being T Tauri stars, there is also strong evidence for the occurrence of protostars embedded in a dusty envelope, which indicates that the star formation process is still ongoing. The inner region of the ONC emerges as a very bright and dense part of the cluster, called the Trapezium, which already expelled most of its gas. It is this cluster region where most of the massive stars are located. The most massive ($m_{\mathrm{system}} \approx 50\,\mathrm{M}_\odot$) and also brightest ($2.5 \cdot 10^5 \mathrm{L}_\odot$) stellar system in this region is the binary θ^1C Ori, which is one out of four leading high-mass objects that ionize the whole nebula by their intense ultraviolet radiation. The strong radiation of these stars also shapes the Orion proplyds, protoplanetary discs that are surrounded by tear-drop shaped ionization fronts (O'dell *et al.*, 1993). Finally, the high densities in these inner cluster region ($\rho_{0.053\,\mathrm{pc}} = 4.7 \cdot 10^4\,\mathrm{pc}^{-3}$, McCaughrean & Stauffer, 1994) suggest that stellar encounters might be relevant for the evolution of circumstellar discs within the Trapezium region.

1.4.2 Dynamical cluster evolution

The dynamical evolution of the stellar population is largely determined by gravitational interactions of the stellar members. Hereby, a fundamental quantity describing the global dynamical state of the cluster is the *virial ratio*

$$Q = \frac{T}{|W|} = \frac{r_{\mathrm{vir}}\sigma^2}{GM_{\mathrm{tot}}}, \tag{1.4}$$

where T is the total kinetic energy, W the total potential energy of the cluster, σ is the statistical dispersion of the velocities (so-called *velocity dispersion*), G is the gravitational constant, M_{tot} is the total cluster mass, and r_{vir} is the virial radius. For an equal-mass system r_{vir} is defined by the average distance between the particles:

$$\frac{1}{r_{\mathrm{vir}}} = \left\langle \frac{1}{|r_i - r_j|} \right\rangle_{i \neq j}. \tag{1.5}$$

In general, the magnitude of the virial ratio specifies whether a cluster is contracting ($Q < 0.5$), expanding ($Q > 0.5$) or in virial equilibrium ($Q = 0.5$). This classification can be inferred from the virial theorem, which yields for any stable spherical system consisting of N self-gravitating particles

$$2T + W = 0. \tag{1.6}$$

While individual deflections of the stellar trajectories are unpredictable in such chaotic N-body systems the overall dynamics of the stellar cluster can be specified by a set of time scales that are introduced in the following.

Crossing time

The *crossing time*, t_{cross}, is given by (Heggie & Hut, 2003; Binney & Tremaine, 2008)

$$t_{\text{cross}} = \frac{2r_{\text{vir}}}{\sigma} = 2\sqrt{2}\frac{r_{\text{vir}}^{1.5}}{\sqrt{GM_{\text{tot}}}} \tag{1.7}$$

where $\sigma \approx \sqrt{GM_{\text{tot}}/2r_{\text{vir}}}$ and the virial radius r_{vir} is given by the potential energy W as $r_{\text{vir}} = GM_{\text{tot}}/2|W|$. The crossing time estimates the typical time scale a star needs to cross the cluster and, thus, describes the amount of mixing of the stellar population. In general, a non-equilibrium dynamical system adjusts back to equilibrium within a few t_{cross}. For massive clusters consisting of 30 000 stars and a radius of $R = 6\,\text{pc}$ typical crossing times of $t_{\text{cross}} \approx 0.3$ Myr are obtained. If the cluster age is less than t_{cross} the population is close to its initial state.

Relaxation time

The path of a star is perturbed by several weak deflections of neighbouring stars. A time that quantifies after which time span these deflections become significant and the star forgets about its initial path is given by the *two-body relaxation time* (Spitzer, 1987)

$$t_{\text{relax}} = 0.1\frac{N}{\ln N}t_{\text{cross}}, \tag{1.8}$$

where N is the number of stars. It expresses the time after which the changes of the direction of motion of the stars become comparable to the initial velocity dispersion. Consequently, within t_{relax} the dynamical cluster state changes significantly and evolves to a globally relaxed system. Note that for the usual case of $N > 35$ we obtain $t_{\text{relax}} > t_{\text{cross}}$ so that the cluster might be mixed and close to dynamical equilibrium but is not relaxed. In other words, for high particle numbers the cluster dynamics are less influenced by encounters due to the deeper cluster potential.

The relaxation time within a cluster varies significantly between the innermost and outermost parts. Therefore, it is useful to define a *half-mass relaxation time* (Spitzer, 1987; Binney & Tremaine, 2008)

$$t_{\mathrm{rh}} = \frac{0.14N}{ln(\gamma N)}\sqrt{\frac{r_{\mathrm{hm}}^3}{GM_{\mathrm{tot}}}}, \tag{1.9}$$

where r_{hm} is the half-mass radius, containing the innermost half of the total cluster mass, and γN the argument of the Coulomb logarithm (Spitzer & Hart, 1971) with $\gamma = 0.11$ for equal-mass particles (Giersz & Heggie, 1994) and < 0.11 otherwise (Giersz & Heggie, 1996). While the dynamics of old globular clusters with typical ages of $t_{\mathrm{age}} \approx 10^{10}$ yr and relaxation time scales of $t_{\mathrm{relax}} \approx 10^8$ yr are significantly influenced by stellar interactions, young clusters like the ONC with relaxation time scales $t_{\mathrm{relax}} = 1.5 \cdot 10^7\mathrm{yr} > t_{\mathrm{age}} = 10^6\mathrm{Myr}$ (adapted from Hillenbrand & Hartmann, 1998) can be approximated as collisionless systems with their dynamics being determined by a smoothed gravitational potential.

However, although the global dynamics are rather unaffected by stellar interactions the circumstellar discs properties can be significantly altered by stellar fly-bys.

Ejection and evaporation time

Stars are able to escape from a bound stellar population if their total binding energy $E_{\mathrm{tot}} = W + T \geq 0$. This translates into the minimum stellar velocity needed to escape the cluster potential, so-called *escape velocity*, given by

$$v_{\mathrm{esc}}(r,t) = \sqrt{2|\phi(r,t)|}. \tag{1.10}$$

The potential $\phi(r,t)$ splits into a part given by the total enclosed mass within r, $M_{\mathrm{tot}}(r,t)$, and a potential contributed by the surrounding material

$$\phi(r,t) = -G\left(\frac{M_{\mathrm{tot}}(r,t)}{r} + 4\pi\int_r^{\infty}\rho(r',t)r'\mathrm{d}r'\right). \tag{1.11}$$

The second term is obtained by integrating over each radial mass shell at $r' > r$.

There are two different types of stellar collisions that force a star to leave the cluster: (i) *Ejections*, which require a strong, single encounter event increasing the velocity of one of the stars to an amount larger than the escape velocity and (ii) *Evaporation* caused by several weak interactions that gradually increase the kinetic energy of a star to finally become unbound from the cluster.

The ejection time scale of the cluster can be approximated by $t_{\mathrm{ejec}} = -N dt/dN \approx 10^4 t_{\mathrm{rh}}$ (Henon, 1969) while numerical simulations (Spitzer, 1987) suggest an evaporation time scale of the order of $t_{\mathrm{evap}} \approx 330 t_{\mathrm{rh}}$.

Collision time

The collision time, t_{coll}, defines the time scale for an actual physical contact between two stars, with collision radius $r_{\mathrm{coll}} = 2r_{\mathrm{star}}$. The collision rate, $1/t_{\mathrm{coll}}$, is obtained by a simple integration of the number of encounters per unit time over all stellar velocities, which results in (Binney & Tremaine, 2008)

$$\frac{1}{t_{\mathrm{coll}}} = \left[16\sqrt{\pi}n\sigma r_{\mathrm{coll}}^2 \left(1 + \frac{GM_1}{2\sigma^2 r_{\mathrm{coll}}}\right)\right]^{-1} \tag{1.12}$$

where n is the stellar density, M_1 the mass of the central star, and σ the velocity dispersion. Here, the second term represents the effect of gravitational focusing, which leads to a reduction of the collision time. For simplicity all stars are assumed to have the same single mass, which strongly underestimates the effect of gravitational focusing.

For typical quantities like a mean stellar mass of $< M_1 >= 0.5$, velocity dispersion of $\sigma = 1\mathrm{km/s}$, $r_{\mathrm{coll}} = 2\mathrm{R}_\odot$, and central densities of $n = 5 \times 10^3\,\mathrm{pc}^{-3}$ as found for the ONC we obtain an collision time scale of the order 10^{11} yr. Hence, stellar collisions are rather unlikely for stellar densities investigated in this study.

However, for a gravitational interaction between the circumstellar disc and the encountering star much larger radii $r_{\mathrm{coll}} \gg 2\mathrm{R}_\odot$ can be assumed. Gutermuth *et al.* (2005) estimated in their study the collision time scales in dependence of the cluster density. Assuming two collision radii, $r_{\mathrm{coll}} = 10^3\,\mathrm{AU}$ for protostellar envelopes (Motte & André, 2001) and $r_{\mathrm{coll}} = 10^2\,\mathrm{AU}$ for classical T Tauri discs (McCaughrean & O'dell, 1996), they find typical encounter time scales of the order 10^5 yr and 10^7 yr, respectively, for stellar densities of 10^4 stars per pc^{-3}.

1.4.3 Mass segregation

Observations showed that stellar clusters, sometimes only a few Myr old, are typically mass segregated, e.g. the most massive stars of the only 1 Myr old ONC are located within the inner $r_{\mathrm{core}} = 0.3\,\mathrm{pc}$ of the cluster (Hillenbrand & Hartmann, 1998). Not only dynamical evolved clusters like the starburst cluster Arches (Harfst *et al.*, 2010) are found to be mass segregated but also still embedded clusters show this trend like the ONC, NGC 6231 (Raboud & Mermilliod, 1998) or NGC 1893 (Sharma *et al.*, 2007). There is a strong debate if the observed mass segregation can be a product of dynamical two-body relaxation of the cluster or if only primordial mass segregation is capable to explain segregation processes on such short timescales. A better understanding of the dynamical mechanisms is needed to further constrain these concepts.

In case of primordial mass segregation massive stars form preferentially at the cluster center. This process is explained by an increased amount of accretion material as well as an accelerated accretion of the surrounding gas due to the location of the stars at the bottom of the potential well. Bonnell & Davies (1998) investigate the evolutionary effect of dynamical mass segregation and conclude that the position of massive stars in young clusters generally reflects the cluster's initial conditions due to the young cluster age relative to their relaxation time (see also Hillenbrand & Hartmann (1998)). Therefore, previous numerical studies assumed an initial mass segregation of the ONC locating the most massive star in the cluster center and the three next massive stars randomly within $r = 0.6 \cdot r_{hm}$ (Bonnell & Davies, 1998) so that it fits today's observations of the ONC.

Another explanation might be a *dynamical mass segregation*. The wide range of observed stellar masses (typical $0.08 - 150\,\mathrm{M}_\odot$ which will be further detailed in Sec. 2.3) implies that their initial kinetic energy depends not only on the stellar position in the cluster but also strongly on the individual stellar masses, with largest kinetic energies for the most massive stars. Stellar interactions lead to an equipartition of the kinetic energy by massive stars transferring kinetic energy to the low-mass stars. As a consequence the massive stars sink towards the cluster center.

Typically, the time scales for dynamical mass segregation are larger than the cluster relaxation time $t_{\mathrm{equ}} > t_{\mathrm{relax}}$. However, recent numerical investigations found that cool clusters dynamical mass segregate on timescales far shorter than expected (Allison *et al.*, 2009; Olczak *et al.*, 2011). Also dynamical friction from the molecular gas can effectively reduce the time scale of the dynamical mass segregation (Er *et al.*, 2009). Moeckel & Bonnell (2009) show, that for system ages less than a few crossing times star formation scenarios predicting general primordial mass segregation are even inconsistent with observed segregation levels for some young embedded clusters. Furthermore, Ascenso *et al.* (2009) argue that there is currently no observational evidence of mass segregation in young clusters since there is no robust way to differentiate between true mass segregation and sample-incompleteness effects.

1.5 Dominant cluster mode

Although the star formation process itself seems comparatively well understood (see Sec. 1.1) there is currently a serious discussion about the environment within which the majority of stars form. A main problem is the absence of a general definition of a stellar cluster. Moreover, the question arises whether most stars form in the few massive clusters, the large number of small-N clusters or in hierarchically structured environments with arbitrary local surface densities. In the latter case massive clusters would only represent an exception. The two main formation models will be briefly explained in the following.

Two sequences of clustered star formation

It is generally believed that most stars, if not all, do not form in isolation but as part of a group of stars consisting between just a few to up to ten-thousands of stars (e.g. Lada & Lada, 2003; Porras *et al.*, 2003; Fall *et al.*, 2005; Evans *et al.*, 2009). However, today only a low fraction of stars in the solar neighbourhood is found in clusters. A comparison of the number of young clusters (< 10 Myr) to the number of evolved clusters indicates that the majority of clusters dissolves quickly after their formation (e.g. Fall *et al.*, 2005; Pfalzner, 2009). Lada & Lada (2003) determine that 90% of the observed embedded clusters within 2 kpc of the Sun have to disperse within 10 Myr after their formation and about 96% after 100 Myr. They called this rapid cluster disruption and the accompanied lack of evolved open clusters *infant mortality*.

The dissolution of young stellar clusters is explained by the expulsion of their residual gas caused by stellar winds, UV radiation, and the first supernova explosions. Due to a significant reduction of the total cluster mass a high number of stars might become unbound. This process was studied by several authors (Hills, 1980; Lada *et al.*, 1984; Adams, 2000; Geyer & Burkert, 2001; Boily & Kroupa, 2003a,b; Goodwin & Bastian, 2006; Bastian & Goodwin, 2006; Baumgardt & Kroupa, 2007; Parmentier & Pfalzner, 2012; Pfalzner & Kaczmarek, 2013) and will be detailed in Section 1.5.2.

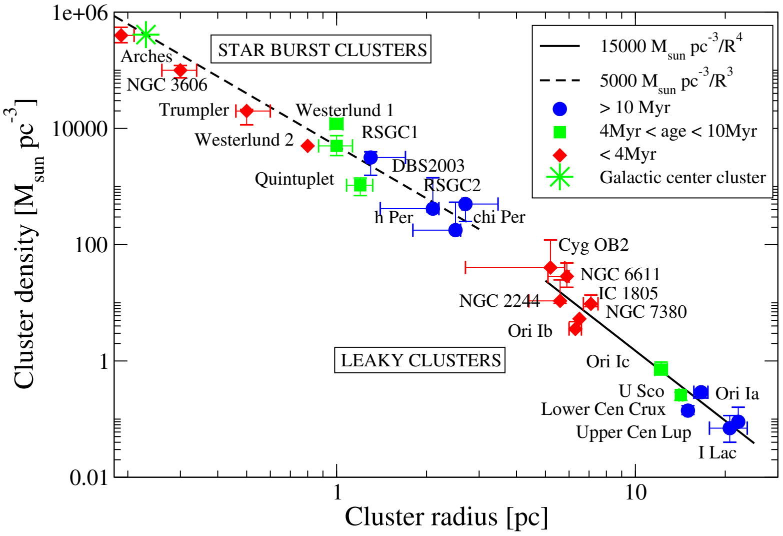

Figure 1.7: Cluster density as a function of the cluster size for clusters more massive than $10^3\,M_\odot$. The Figure is taken from Pfalzner (2009) while the observational data points are taken from Wolff *et al.* (2007), Figer (2008), Borissova *et al.* (2008), and references therein.

While Lada & Lada (2003) concentrated on the temporal evolution of embedded clusters, recent investigations by Pfalzner (2009) found evidence for a bimodal evolution process of stellar clusters more massive than $10^3\,\mathrm{M}_\odot$ in the radius-density plane. Figure 1.7 shows the sequential radius-density-age relation revealing two distinct groups of clusters. Clusters in the first sequence are termed ***starburst clusters*** and consist of several ten-thousand stars in a rather small volume of only a few 0.1 pc half-mass radius. Within 20 Myr of development their total masses of $\approx 20\,000\,\mathrm{M}_\odot$ remain fairly constant while their sizes increase significantly to about $1 - 3$ pc. Pfalzner & Kaczmarek (2013) determined star formation efficiencies of up to 70% as an explanation for the minor dissolution of the cluster and comparatively low velocity dispersions of the stellar members (Rochau *et al.*, 2010; Bastian, 2011; Hénault-Brunet *et al.*, 2012).

Stars within the dense environments of such starburst clusters are very prone to stellar encounters. Olczak *et al.* (2012) investigated stellar encounters in the Arches starburst cluster and determined that more than 30% of all stellar discs are completely destroyed by gravitational interactions within the first 2.5 Myr. However, well-observed starburst clusters in the Milky Way are very rare because they are mostly located in the dense spiral arms or close to the Galactic Center where observations are limited by the high background density. In the present study the focus is on massive clusters in the solar neighbourhood and starburst clusters will not be considered.

Massive nearby star forming regions, which are subject of the present study, evolve along the second sequence in the density-radius plane, the so-called ***leaky cluster*** sequence. These clusters have initial total masses similar to the starburst clusters but are distributed in a much larger area with a radius of about 6 pc. Within 20 Myrs the size of leaky clusters increases significantly up to ≈ 20 pc while they additionally lose large amounts of their total mass. Pfalzner & Kaczmarek (2013) found a star formation efficiency of $< 30\%$ of such clusters and concluded that the expulsion of the residual gas is a major process for cluster members to become unbound.

Hierarchical cluster formation

In contrast to the observed modes of a clustered formation the size and surface density of a star forming region in the theoretical context of a hierarchical cluster formation process are believed to be continuously distributed throughout the hosting galaxies (Elmegreen *et al.*, 2006; Bastian *et al.*, 2007). In this picture one might argue that the embedded clusters observed by Lada & Lada (2003) are simply a selection effect and an observational bias leads to a neglect of the stars residing in the lower local density regimes. Another approach is that already during the formation process bound stellar systems are naturally formed in the observed density peaks of the interstellar medium, while lower density clusters instantly dissolve. Hereby, a minor fraction of $\approx 30-35\%$ of all stars is estimated to be born in such bound entities (Kruijssen, 2012). By contrast Lada & Lada (2003) observed that 90% of stars are expelled from a cluster after the gas expulsion process and only about 10% might remain bound.

The probably most popular study about this subject was published by Bressert *et al.* (2010) who investigated local surface densities in the solar neighbourhood ($< 500\,\mathrm{pc}$ distance) and found a smoothed log-normally shape of the stellar distributions. They favour a continuous star formation process over clustered modes of star formation due to a lack of multiple peaks in the observed local surface density distribution of star forming regions. However, recent studies found that their results might be caused by a superposition effect of multiple modes of star formation (Pfalzner *et al.*, 2012; Gieles *et al.*, 2012) so that a smooth surface density distribution can not be used as a criterion for hierarchical star formation. Moreover, starburst clusters or the dense inner Trapezium region of the ONC have been excluded in Bressert *et al.* (2010) giving no further qualification of the Pfalzner (2009) cluster sequences.

The discussion if most stars form in clusters leads to the question: What is a cluster? While Lada & Lada (2003) estimated 90% of all stars to form in clusters due to their cluster definition of a local surface density threshold of 3 stars per pc^2 Bressert *et al.* (2010) came up with a density limit of 200 stars per pc^2 leading to only 26% of all stars forming in clusters. The Bressert *et al.* (2010) limit is based on the estimated density for encounters to become important in a clustered environment (Gutermuth *et al.*, 2005). However, such arguments are irrelevant for our study since we focus on the actual cluster densities and find high variations of the local surface densities between the maximum and the observed local surface density, which is basically used to define a stellar population as a cluster. A detailed description will be given in Section 4.3. Additionally, here, the low density regions observed by Bressert *et al.* (2010) are of minor importance since stellar interactions might be rare in their present density conditions.

1.5.1 Embedded cluster phase

For the first 10^5 to 10^6 yr of the star formation process the newly formed protostars are surrounded by their natal gas. Such evolutionary very young clusters are called *embedded clusters*. Due to gas extinction the formed young stars are mostly not visible in the optical regime. Only longer wavelength emissions like near infrared (NIR) radiation are able to pass obstacles in form of dust and gas providing first insights in T Tauri star characteristics. Still, little constrains can be made on stellar quantities due to the optical thick cloud structure.

So far it is unclear if the formation of stars in such embedded clusters starts in the dense

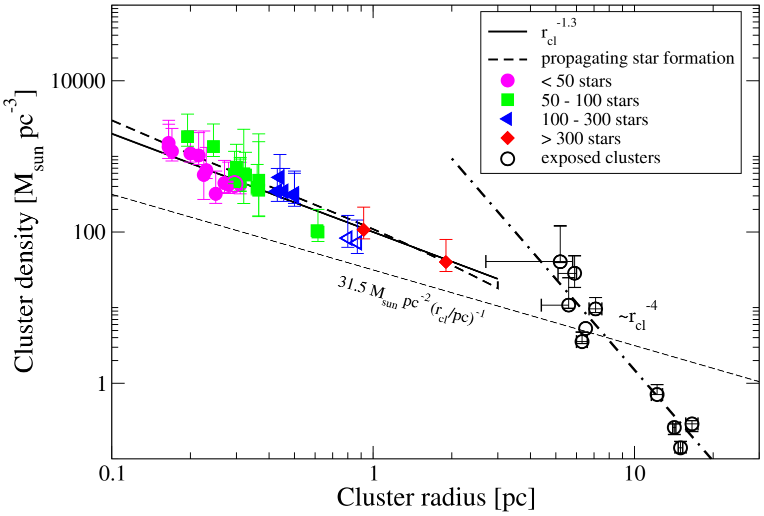

FIGURE 1.8: Cluster density as a function of cluster radius for embedded clusters with more than 200 observed members (coloured symbols) and the leaky cluster sequence found by Pfalzner (2009) for clusters more massive than $10^3\,\mathrm{M}_\odot$ (black open circles). The thin dashed line indicates the observational limit defined by Carpenter *et al.* (2000). The original figure is taken from Pfalzner (2011).

inner part of Giant Molecular Clouds or if stars form simultaneously throughout the cloud, hence, to a much lower degree in the outer regions. Figure 1.8 shows the cluster density versus the cluster size for the embedded clusters observed by Lada & Lada (2003). Pfalzner (2011) was the first to interpret their observed mass-radius relation as a sequence, which contains as well the precursors for the radius-density-age relation of exposed leaky clusters. If sufficient material is provided by the surrounding molecular cloud the embedded clusters potentially gain enough mass to form additional stars and thus develop towards the leaky cluster sequence. Moreover, Pfalzner (2011) shows that the development in the density-radius plane can be fitted by $\rho \approx 100 \cdot r^{-1.3}\,\mathrm{M}_\odot\,\mathrm{pc}^{-3}$. The density development in the embedded phase is flatter than the evolutionary track of the leaky clusters since no gas has been expelled and star formation is still ongoing. After reaching a maximum mass of several $10^4\,\mathrm{M}_\odot$ and cluster radii of about $1-3\,\mathrm{pc}$ the residual gas is ejected, the cluster rapidly expands, and most of its stellar members become unbound (see also Section 5).

While there are predictions that star formation starts simultaneously throughout the entire Molecular Cloud, the evolution shown in Figure 1.8 suggests that the process of star formation starts in the central cluster region and is delayed for larger distances from the center. Figure 1.8 indicates that the first few stars of a forming cluster are located in the very dense center of the cluster with $r_{\mathrm{cluster}} < 0.2\,\mathrm{pc}$. However, Parmentier & Pfalzner

(2012) claim that star formation occurs simultaneously within the whole cluster but at a slower rate in the outer parts. They show that due to an observational threshold, given by the population of background stars (Carpenter *et al.*, 2000), the distant sparse star forming regions of the molecular cloud might be neglected in observations (see also Pfalzner, 2011). Therefor, the results found by Pfalzner (2011) present a density limit for the embedded cluster evolution in the density-radius plane.

1.5.2 Gas expulsion phase

The rapid disruption of stellar populations within a few Myr after their formation, as assumed in the concept of *infant mortality*, is explained by an extremely fast gas expulsion process. Observations show that the majority of young clusters eject their residual gas in less than ≈ 5 Myr (Whitworth, 1979; Leisawitz *et al.*, 1989; Lada & Lada, 2003), however, the significance of the responsible mechanisms is unclear. Adams (2000) estimated the gravitational binding energy of a cluster to be

$$E \approx 4 \times 10^{46}\,\mathrm{erg} \left(\frac{M}{1\,000\,\mathrm{M}_\odot} \right)^2 \left(\frac{R}{1\,\mathrm{pc}} \right)^{-1}. \tag{1.13}$$

Convenient initial quantities, which fulfill the requirements to evolve along the leaky cluster sequence, would be $M_{\mathrm{total}} = M_{\mathrm{gas}} + M_{\mathrm{stars}} = 100\,000\,\mathrm{M}_\odot$ and $R = 6\,\mathrm{pc}$ (Pfalzner & Kaczmarek, 2013). According to Equation 1.13 an energy of 10^{49} to 10^{50} erg would be required to expel the entire amount of residual gas. A simple explanation would be an early supernova explosion of an O-type star. Such energetic explosions release energies of 10^{51} to 10^{53} erg (Kitayama & Yoshida, 2005; Kitaura *et al.*, 2006) within very short timescales. However, the time interval until a high-mass star collapses in a supernova explosion decreases exponentially with its mass (Schaller *et al.*, 1992), with typical lifetimes for massive O-stars ($120\,\mathrm{M}_\odot$) of 3 Myr while the first supernova explosion of θ^1C Ori in the Orion Nebula Cluster would be expected after about 5 Myr. However, as argued by Palla & Stahler (2000) rapid gas expulsion occurs even for low-mass clusters in less than 10 Myr, which are void of massive stars.

Other energy sources to explain an early ejection of the gas are given by the UV flux and stellar winds of the massive stars. Tenorio-Tagle *et al.* (1986) analysed the effect of photoionisation in young clusters and found that massive stars are able to remove significant amounts of gas before the first star explodes in a supernova. Depending on the gas profile Chiosi & Maeder (1986) estimated an O5-star releasing 4×10^{52} erg in form of radiation during its lifetime ($\approx 10 Myr$), while stellar winds account for additional 10^{49} erg until the star explodes (Kudritzki *et al.*, 1987). See also Goodwin (1997) and Lamers & Cassinelli (1999) for more details.

A characteristic timescale unit to evaluate the impact of the cluster gas dispersal is the *crossing time* that has been introduced in Section 1.4.2. Baumgardt & Kroupa (2007) showed that clusters return to dynamical equilibrium already a few tens of crossing times after the gas is expelled.

Alternative disruption processes

After a rapid gas expulsion process a high fraction of about 90% of all stellar clusters is dispersed. However, observations indicate a further decreasing cluster frequency over the first 100 Myr with approximately 90% of clusters being disrupted every decade in age (Fall *et al.*, 2005; Chandar *et al.*, 2006; Whitmore *et al.*, 2007). Such further disruptions are caused by mechanisms that become important on much longer time scales than the gas expulsion.

Relevant internal processes are given by two-body relaxation and stellar evolution, while tidal fields are potential external effects. For our prototype cluster we obtain a typical half-mass relaxation time (the time scale a star 'forgets' about its initial path) of about 100 Myr (Spitzer, 1987), which indicates that due to the high number of stars two-body relaxation is of minor importance in the early stage of cluster development.

Stellar evolution of individual high-mass stars might reduce the total mass of young clusters. Depending on its mass the stars evolve on different timescales, where stars more massive than $8\,\mathrm{M}_\odot$ generally resolve quickly in a supernova explosion. However, the first supernovae explosions of the most massive stars are expected after a few Myr, which is beyond the scope of interest of this investigation, e.g. it takes > 30 Myr for a $10\,\mathrm{M}_\odot$ star to explode in a supernova (see Eq. 1.1). Goodwin (1997) determined a total cluster mass loss of 10% within the first 50 Myrs due to stellar evolution. Within 10 Gyr the cluster mass is reduced by approximately 30% (Baumgardt & Makino, 2003). Hereby, the mass reduction can be assumed as nearly adiabatically, which minimises the fraction of stars becoming unbound by a reduction of the potential cluster energy. The effect of stellar evolution on the time scales considered in this work plays only a minor role and can be neglected.

Moreover, interactions with an external Galactic tidal field become essential when investigating massive starburst clusters like Arches, which is located at a projected distance of only 25 pc from the center of the Milky Way (Olczak *et al.*, 2012). However, here, the effect of a tidal field has been neglected since the focus is on the early evolution of massive embedded clusters in the solar neighbourhood, thus, a sufficient distance to the Galactic center can be assumed. In such regions the clusters are only marginally affected by weak tidal fields of the surrounding clouds (see also Sec. 1.5.2).

Star formation efficiency

The star formation efficiency ϵ turns out to be an important criterion for the survivability of a stellar cluster after the residual gas is expelled. It is defined as $\epsilon = M_{\mathrm{stars}}/M_0$, where M_{stars} is the mass of the stellar content while $M_0 = M_{\mathrm{stars}} + M_{\mathrm{gas}}$ represents the total mass of the stars and the surrounding gas cloud. According to its definition ϵ is assumed constant for a certain Molecular Cloud. In the following the star formation efficiency will be introduced in detail.

Analytical investigations found that in case of a rapid gas-mass loss of the primordial embedded cluster star formation efficiencies of $> 50\%$ are required to obtain a subsequently bound system (Hills, 1980; Mathieu, 1983; Elmegreen, 1983). Therefore, they analysed the evolution of the total cluster energy during the gas expulsion phase. These analytical models solely consider the total kinetic and the total potential energy of the cluster to determine the survivability of a bound stellar system. Adams (2000) and Boily & Kroupa (2003a) reviewed the analytical approach by Hills (1980) and showed that the fraction of bound stars is not only a function of the star formation efficiency but also of the initial stellar distribution function. They found lower star formation efficiencies of around 30% to retain a significant fraction of bound mass. A short introduction of the analytical approach is given in Appendix A.

Lada *et al.* (1984) performed the first Nbody simulations of embedded star clusters and their dissolution after gas expulsion. Their model clusters contained only a minor fraction of 50 (in a few cases 100) stars per cluster that were distributed in a Plummer shaped sphere. In their simulations the gas cloud was initially included by a background potential and removed over varying expulsion timescales of up to 1 Myr. They found that a small fraction of stars can remain bound as a cluster even for $\epsilon < 50\%$, which is in contrast to the conclusions of Hills (1980). They also determined that the bound fraction depends strongly on the gas expulsion timescale, with significantly more stars remaining bound for an increasing expulsion timescale. In general, the expulsion occurs on time scales less than the clusters dynamical crossing time (Hills, 1980) with a maximum time for the expulsion of four crossing times (Lada *et al.*, 1984). Several further numerical investigations confirmed the approach by Lada *et al.* (1984), whereat some of them are summarized in Figure 1.9. It is shown that a star formation efficiency of about 30% is the threshold for the survival of a bound cluster core after rapid gas expulsion (Goodwin, 1997; Lada, 1999; Goodwin & Bastian, 2006; Baumgardt & Kroupa, 2007). Even lower star formation efficiencies of less than 10% are possible if assuming adiabatic gas expulsion (Baumgardt & Kroupa, 2007).

Furthermore, Lada *et al.* (1984) investigated initially sub-viral clusters and found that the low velocities of the stars can be a potential mechanism to obtain bound clusters in case of star formation efficiencies being lower than 20%. Geyer & Burkert (2001) continued

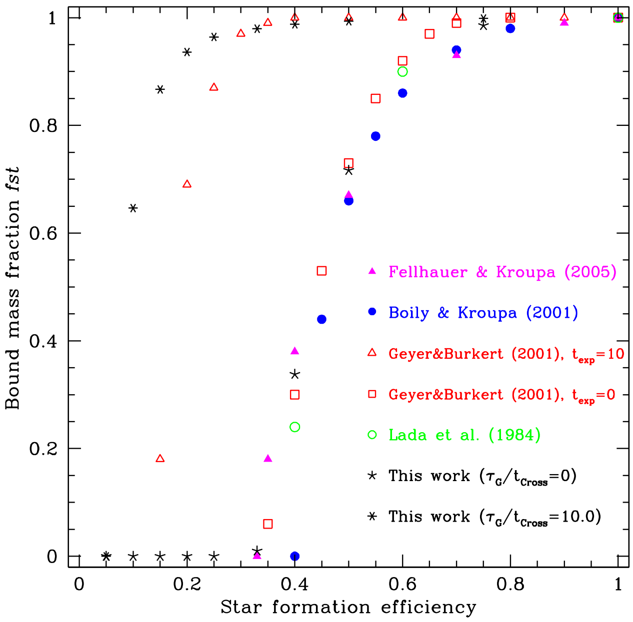

FIGURE 1.9: The fraction of stars which remain bound as a cluster after gas removal as a function of the star formation efficiency for results from the literature. While the right line of symbols represents the case of an instantaneous gas expulsion, open triangles and stars on the left show results for slow gas removal. The Figure is taken from Baumgardt & Kroupa (2007).

this thoughts by investigating different initial velocity dispersions of a stellar distribution. They argue that star formation efficiencies have to be high in order to to maintain a bound core but can be as low as 10% if the initial velocity dispersion is very small.

Geyer & Burkert (2001) used an embedded stellar King distribution of 1000 stars for their investigations. In particular, they used two different approaches for simulating the initial gas distribution. Despite using Nbody simulations for the stars and a background potential modelling the gas, they performed sophisticated SPH (Smoothed Particle Hydrodynamics) simulations of the gas component. However, similar results were obtained with both models, favouring the gaseous background potential for most embedded cluster simulations due to its simplicity.

In most cases numerical investigations focus on standard models of an equal cluster and gas cloud profile using the star formation efficiency ϵ, the cluster size r_{cluster}, and the gas expulsion timescale t_{exp} as parameters to describe the bound fraction. However, Adams (2000) published the first investigation assuming a locally varying star formation efficiency $\epsilon(r)$ by simulating the development of a stellar King profile and a nearly isothermal distribution of the gas component. As expected for the collapse of a GMC (see Appendix in Adams, 2000), the stellar density is higher than the gas density in the cluster center ($\epsilon(r) > 50\%$) whereas the density in the outer regions is dominated by gas ($\epsilon(r) \ll 50\%$).

Adams (2000) found that after the gas is expelled an exceeding fraction of stars remains bound as a cluster, which can be approximated by $N_{\mathrm{bound}}/N_{\mathrm{total}} = 2\epsilon - \epsilon^2$.

Moreover, he assumed an anisotropic velocity distribution model and found that the fraction of stars remaining bound as a cluster is higher than for the isotropic distribution model. In general, the number of bound stars depends strongly on the velocity distribution function as suggested by Boily & Kroupa (2003a). Chen & Ko (2009) reviewed the numerical investigations by Adams (2000) and claimed that the initial kinetic energy of the cluster and the initial cluster-cloud mass ratio at a certain Lagrange radius are much more sensible criteria for the fraction of bound stars.

Despite the star formation efficiency, stellar distribution function and the gas expulsion timescale the fraction of bound stars depends on the cluster radius. Baumgardt & Kroupa (2007) studied the influence of the galactic tidal field by assuming the cluster size to be much smaller than its distance to the Galactic center. They found that the tidal field slightly reduces the fraction of bound stars in limited cases of $r_{\mathrm{hm}}/r_{\mathrm{tide}} > 0.05$, where r_{hm} defines the half-mass radius of the cluster and r_{tide} is the radius beyond which the tidal forces of the hosting galaxy are able to remove stars from the cluster.

Another idea to obtain bound stellar clusters after blowing out the natal gas is the merging of sub-clusters. Fellhauer & Kroupa (2005) showed that star formation efficiencies can be as low as 20% and still leave a gravitationally bound stellar population in star cluster complexes that subsequently merge to a bound population.

Estimates of star formation efficiencies by observations of young stellar clusters are very challenging. A major difficulty is finding the actual number of young stellar objects, which are surrounded by dusty discs and deeply embedded in their natal gas. However, observations of Giant Molecular Clouds, the birthplaces of young protostars (see Sec. 1.1), indicate that star formation appears to be a rather inefficient process. In general, only a minor fraction of $\leq 30\%$ of the total mass is typically transformed into stars (Lada & Lada, 2003).

Myers *et al.* (1986) studied 54 Giant Molecular Clouds in the inner galactic region and found star formation efficiencies ranging from $\epsilon = 0.06\%$ to 50%. They interpreted the low median value of $\epsilon = 2\%$ as a reason for a low fraction of remnant bound clusters after the expulsion of the residual gas. Additionally, they already concluded that the considerably varying star formation efficiencies of the clouds depend on the initial cloud mass. Recent observations by Weidner *et al.* (2007) confirmed a strong decrease of the global star formation efficiency from low-mass star clusters to massive clusters containing high-mass stars.

However, Lada *et al.* (2010) suggest that the highly non-uniform distribution of stars is not a function of the initial cloud mass as assumed by Myers *et al.* (1986) and Weidner

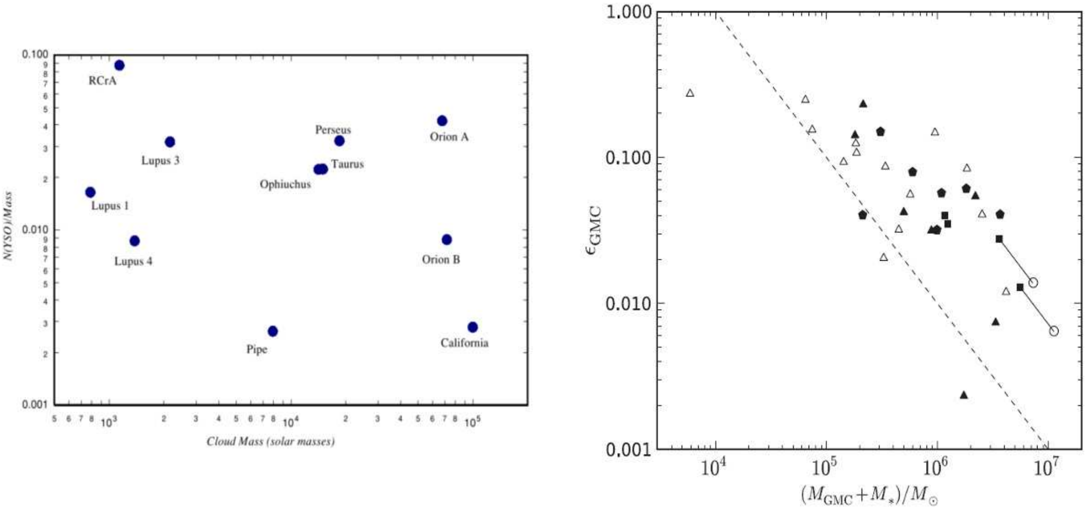

FIGURE 1.10: (a) Ratio of the number of Young Stellar Objects, N(YSO), to the total cloud mass as a function of the total cloud mass. This is roughly equivalent to a measure of twice of the star formation efficiency as a function of the cloud mass. The figure is taken from Lada *et al.* (2010). (b) Star formation efficiency as function of the total cluster mass. The dashed line indicates the luminosity limit. The figure is taken from Murray (2011) with the plotted data taken from Solomon *et al.* (1987) (filled triangles), Heyer *et al.* (2009) (open triangles), Grabelsky *et al.* (1988) (filled squares), and Bronfman *et al.* (1989) (filled pentagons).

et al. (2007) but varies by more than one order of magnitude (see Fig. 1.10a). Therefore, they analysed cloud complexes within 450 pc from the Sun and determined star formation efficiencies of $\epsilon < 5\%$ ($N(\mathrm{YSO})/Mass < 0.1$, Fig. 1.10a). Murray (2011) found star formation efficiencies of $\epsilon = 8^{+12}_{-8}\%$ in a similar sample of young stellar clusters in the Milky Way and plotted the efficiency as a function of the total cloud mass (Fig. 1.10b). They found that the observed trend can potentially be explained by an observational selection effect, namely a luminosity limit indicated by the dashed line.

Evans *et al.* (2009) found similar star formation efficiencies of $\epsilon = 3\%$ to 6% for star forming regions within 300 pc from the Sun. Considering an average overall cloud lifetime of about 20 Myr (Matzner, 2002; McKee & Ostriker, 2007; Murray, 2011), they argue that in case of a continuing constant star formation for 10 Myr a cluster is able to reach final efficiencies of 15% to 30%. Although most studies focus on clusters in the solar neighbourhood, such little star formation rates have also been determined for extragalactic regions, where efficiencies of $\epsilon = 14^{+18}_{-8}\%$ are determined for galaxy cluster cores (McDonald *et al.*, 2011).

Many studies have investigated the effect of the gas expulsion on the evolution of stellar clusters. However, here, for the first time the relevance of star-disc encounters during the entire cluster evolution process will be investigated. The focus will be on the most massive clusters in the Solar neighbourhood, which - as discussed above - evolve along the leaky cluster sequence after an early expulsion of their natal gas. The numerics and setup for the models used in the present investigation will be detailed in the following.

2 Methods

2.1 Numerics

The densities of young star clusters span a wide range from sparse clusters like Taurus with densities of 1 to 10 stars per pc^3 (Luhman *et al.*, 2009) to very massive and compact clusters like the Arches cluster with a core density of several 10^5 stars per pc^3 (Figer *et al.*, 1999). Such dense stellar environments lead to strong gravitational interactions between the cluster members and effect as well the protoplanetary discs. To investigate the temporal evolution of circumstellar discs in such large stellar number environments numerical simulations are required. Two different types of simulations were used in this context, a parameter study of individual stellar encounters and dynamical cluster simulations of all (but disc-less) stars. These numerical investigations can be treated separately and are combined in a final diagnostic step.

In my diploma thesis I performed a first parameter study to investigate the effect of an encounter between a disc-surrounded and a disc-less star, so-called star-disc encounter events. Hereby, the stars are represented by two particles and the disc by N pseudo-particles, which reproduce the dynamical behaviour of the real mass distribution of a circumstellar disc. The disc particles initially move on Keplerian orbits around the star. The temporal development of the disc-mass distribution during an encounter is modelled using a fifth-order Runge-Kutta Cash-Karp integrator with an adaptive time-step size control for the numerical calculations. Long-range interactions of the gravitational forces between the disc particles and the perturbing stars are calculated using a hierarchical tree method (Barnes & Hut, 1986). The numerical methods are outlined in Appendix B.

Here, the interactions between stars in different model clusters have been simulated for several Myr of cluster evolution. The code is based on the code NBODY6 originally developed by Sverre Aarseth in the late 60s (Aarseth, 1963, 1974, 2003). Apart from a general presentation of the temporal cluster development, these simulations provide valuable information about typical encounter parameters like encounter frequencies, minimum stellar separations, stellar mass ratios and orbital eccentricities.

In the following, the code NBODY6 will be introduced. Moreover, code modifications and the combination with the single encounter investigations will be detailed.

2.1.1 Cluster dynamics

In the past, simulations of star clusters containing several thousand particles have been computationally too expensive but new developments in computer techniques and numerical algorithms in the last years have lead to a reduction of the computation time and increasing accuracy, so that computationally intense simulations of massive stellar clusters can be solved in appropriate time periods today.

Massive stellar clusters contain up to ten thousands of stars that are gravitationally interacting. The dynamics of the system are described by $6N$ ordinary differential equations, $3N$ for the particle positions and $3N$ for the velocities that have to be solved numerically. The particles interact only via gravitational forces, which are described by a set of N Newtonian equations of the form:

$$\ddot{\vec{r}}_i = \vec{a}_i = \frac{\vec{F}_i}{m_i} = -G \sum_{\substack{j=1 \\ j \neq i}}^{N} \frac{m_j(\vec{r}_i - \vec{r}_j)}{|\vec{r}_i - \vec{r}_j|^3}, \tag{2.1}$$

where m_i and m_j are the particle masses, $\vec{r}_i$ and $\vec{r}_j$ the particle positions, and G is the gravitational constant. This is known as the gravitational N-body problem, which cannot be solved analytically for $N \geq 3$. For the realisation of appropriate cluster models a highly accurate N-body code is needed. Here, the code NBODY6 developed by Sverre Aarseth is used, which operates with a high-order integrator for the integration of the gravitational forces at a high precision.

To improve the computational effort sophisticated numerical schemes like a parallelised force summation, an improved neighbour treatment and a regularisation for close encounters are implemented. All methods are described in the following (for further details see Aarseth, 2003).

Hermite integration scheme

The generic problem of solving ordinary differential equations of N-th order can be reduced to the study of a set of N coupled first-order differential equations for the functions $\vec{a}_i$ (with $i = 1, 2, ..., N$) which have the general form

$$\dot{\vec{a}}_i(t) = f_i(t, \vec{a}_1, ..., \vec{a}_N), \;\; i = 1, ..., N. \tag{2.2}$$

The advantage of this scheme is that there are no derivatives on the right hand side of any of those equations, and there are only first derivatives on the left hand side. In the following, the numerical treatment of one of the N differential equations will be shown exemplary.

One possibility to approximate a solution within an interval $\Delta t = t_1 - t_0$ is given by the Euler method

$$\vec{a}_{i,1} = \vec{a}_{i,0} + \Delta t \cdot f_i(t_0, \vec{a}_{i,0}), \tag{2.3}$$

where $a_{i,1}$ is the approximation of the reference point $a(t_1)$ and the approximation of $a(t_0)$ is given by $a_{i,0}$. For the Euler method the derivative information are only expanded to the beginning of the next interval, t_1, and therefore the obtained errors are only one power of Δt smaller. So this linear approximation will lead to large errors and consequently unstable trajectories.

A more accurate time-integrator to track the trajectories of a high number of stars for several Myr is the fourth order Hermite integrator scheme which was introduced and implemented in NBODY6 by Makino (1991) (see also Makino & Aarseth, 1992)). It works with a predictor-corrector method, which means it involves a prediction step for a rough estimation of the particles path and a corrector step to adjust the initial approximation.

The first step is to further differentiate Equation 2.1 and obtain

$$\dot{\vec{a}}_{i,0} = G \sum_{\substack{j=1 \\ j \neq i}}^{N} m_j \left(\frac{\vec{v}_{ji,0}}{|\vec{r}_{ji,0}|^3} - 3 \frac{(\vec{r}_{ji,0} \cdot \vec{v}_{ji,0}) \vec{r}_{ji,0}}{|\vec{r}_{ji,0}|^5} \right), \tag{2.4}$$

where $\vec{r}_{ji,0} = \vec{r}_{j,0} - \vec{r}_{i,0}$ is the current relative position and $\vec{v}_{ji,0} = \vec{v}_{j,0} - \vec{v}_{i,0}$ the current relative velocity between the particles i and j. A first prediction of the new position $r_{i,1}$ and velocity $v_{i,1}$ is simply given by their Taylor series:

$$\vec{r}_{i,1} = \vec{r}_{i,0} + \vec{v}_{i,0}(t_1 - t_0) + \frac{\vec{a}_{i,0}}{2}(t_1 - t_0)^2 + \frac{\dot{\vec{a}}_{i,0}}{6}(t_1 - t_0)^3 \tag{2.5}$$

$$\vec{v}_{i,1} = \vec{v}_{i,0} + \vec{a}_{i,0}(t_1 - t_0) + \frac{\dot{\vec{a}}_{i,0}}{2}(t_1 - t_0)^2, \tag{2.6}$$

where now $\vec{a}_{i,0} = \dot{\vec{v}}_{i,0}$ denotes the current acceleration of particle i.

A Hermite interpolation can be used to further improve the predicted values. Therefor, the Taylor expansion for $\vec{a}_{i,1}$ and $\dot{\vec{a}}_{i,1}$ are generated to third and second order, respectively:

$$\vec{a}_{i,1} = \vec{a}_{i,0} + \dot{\vec{a}}_{i,0}(t_1 - t_0) + \frac{\ddot{\vec{a}}_{i,0}}{2}(t_1 - t_0)^2 + \frac{\dddot{\vec{a}}_{i,0}}{6}(t_1 - t_0)^3 \tag{2.7}$$

$$\dot{\vec{a}}_{i,1} = \dot{\vec{a}}_{i,0} + \ddot{\vec{a}}_{i,0}(t_1 - t_0) + \frac{\dddot{\vec{a}}_{i,0}}{2}(t_1 - t_0)^2 \tag{2.8}$$

where $\vec{a}_{i,0}$ and $\dot{\vec{a}}_{i,0}$ are known from Eq. 2.1 and Eq. 2.4, respectively. While $\vec{a}_{i,0}$ and $\dot{\vec{a}}_{i,0}$ can simply be obtained by the initial position and velocity, a direct calculation of $\ddot{\vec{a}}_{i,0}$ and $\dddot{\vec{a}}_{i,0}$ is not possible. However, Eq. 2.7 and Eq. 2.8 can now be combined to obtain the third order derivative:

$$\dddot{\vec{a}}_{i,0} = 6\left(2\frac{\vec{a}_{i,0} - \vec{a}_{i,1}}{(t_1 - t_0)^3} + \frac{\dot{\vec{a}}_{i,0} - \dot{\vec{a}}_{i,1}}{(t_1 - t_0)^2}\right). \tag{2.9}$$

Substituting Eq. 2.9 into Eq. 2.7 gives the second order derivative of the acceleration:

$$\ddot{\vec{a}}_{i,0} = -6\frac{\vec{a}_{i,0} - \vec{a}_{i,1}}{(t_1 - t_0)^2} - 2\frac{2\dot{\vec{a}}_{i,0} - \dot{\vec{a}}_{i,1}}{t_1 - t_0}. \tag{2.10}$$

These solutions can now be used to estimate the corrections of Eq. 2.5 and Eq. 2.6 by an expansion to two higher orders:

$$\vec{r}_i = \vec{r}_{i,1} + \ddot{\vec{a}}_{i,0}\frac{(t_1 - t_0)^4}{24} + \dddot{\vec{a}}_{i,0}\frac{(t_1 - t_0)^5}{120} \tag{2.11}$$

$$\vec{v}_i = \vec{v}_{i,1} + \ddot{\vec{a}}_{i,0}\frac{(t_1 - t_0)^3}{6} + \dddot{\vec{a}}_{i,0}\frac{(t_1 - t_0)^4}{24} \tag{2.12}$$

where $\vec{r}_i$ and $\vec{v}_i$ denote the corrected position and velocity, respectively.

The advantage of the Hermite predictor-corrector scheme is - beside its comparatively simple structure - an eminent energy and angular momentum conservation, which is required for a long timescale cluster development. This provides the opportunity to determine the cluster dynamics at high accuracy*.

Individual time steps

The stellar densities in the cluster center can be several magnitudes higher than in the cluster outskirts. Many close interactions in these inner parts require a high spatial and temporal resolution. In principle this would result in decreasing time steps for all cluster regions, which would significantly increase the computation time. One vital method to reduce the computational effort for such systems is to adapt the integration accuracy to the physical problem. In the temporal domain this is realised by individual time steps Δt_i for the particles, so that in case of large dynamical timescales the integration steps are not as frequent as required for close particle interactions. Shorter individual time scales in the dense cluster regions assure a sufficient accuracy while the computational effort can be reduced by prolonged time steps in the sparse cluster parts.

The individual time step method is organised as following. First, the particle i of minimum time step width Δt_i is determined. Afterwards the positions of the remaining particles for this particular time step are predicted (as introduced in the Hermite scheme, Eq. 2.5) to obtain the gravitational force acting on i. After adopting the position, velocity and time

---

[*] Here, simulations with deviations in the total energy of $> 0.001\%$ have been excluded from the diagnostic step.

for particle i the process starts again. In NBODY6 the individual time step is defined by (Aarseth, 1985)

$$\Delta t_i = \left(\eta \frac{|\vec{a}_i||\ddot{\vec{a}}_i| + |\dot{\vec{a}}_i|^2}{|\dot{\vec{a}}_i||\dddot{\vec{a}}_i| + |\ddot{\vec{a}}_i|^2} \right)^{1/2} , \tag{2.13}$$

where η is a dimensionless accuracy parameter which is typically chosen to be 0.02 (Aarseth, 2003).

A so-called *block time-step* scheme is used in NBODY6 to obtain shared integration time steps for the particles. Hereby, the individual time steps are quantised by powers of 2,

$$\Delta t_i = 2^{-k} \qquad k = 0, 1, 2 \ldots n, \tag{2.14}$$

where n provides the quantisation exponent for the smallest time step $\Delta t_{\mathrm{i,min}} > 2^{-n}$. Each individual time step, given by Eq. 2.13, is truncated to the closest block time step given by Eq. 2.14.

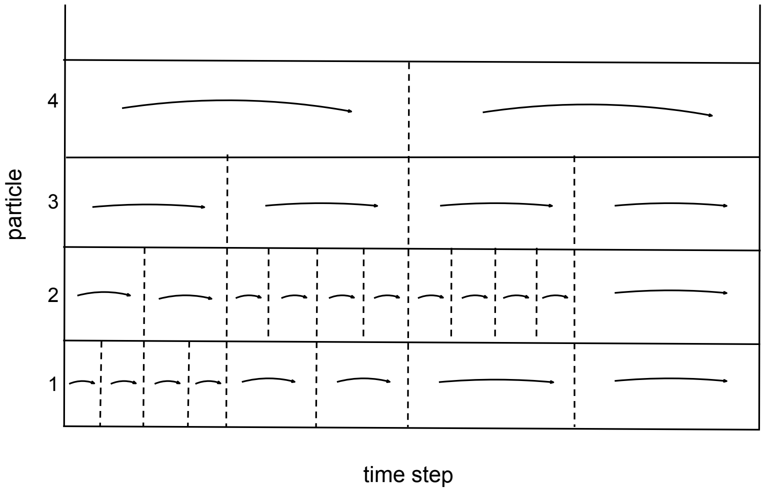

FIGURE 2.1: Sketch of a block time step scheme.

Figure 2.1 shows a sketch of the block time step scheme. As outlined above, particle 1 starts with the shortest time step after which its new accurate position and velocity will be determined. Particle 4 defines the largest step after which the phase space coordinates of all particles will be quantified and updated. For the last time step bin the particles 1, 2, and 3 have equal time step sizes. Here, the minimum time step is four times larger than the initial minimum time step.

Neighbour treatment

Gravitational N-body simulations are conceptually simple in principle, because they merely involve integrating the $6N$ ordinary differential equations defining the particle motions in Newtonian gravity. However, in practice, the number of particles N involved can be very large (as in the present application) and the number of gravitational particle-particle interactions, which have to be evaluated, rises as

$$\sum_{i=1}^{N}\sum_{j=1}^{i-1} 1 = \frac{N(N-1)}{2} = \mathcal{O}(N^2) \ . \tag{2.15}$$

Similarly to the usage of adaptive time steps for the temporal domain, the accuracy in the spatial domain can be adopted to the physical problem, reducing the required N^2 calculations. A possible solution is to construct an algorithm which restricts the direct force summation to particles close to each other, while the contribution from more distant objects is considered on a less accurate level.

To significantly reduce the number of calculation steps the so-called Ahmad-Cohen neighbour scheme, introduced in detail by Makino & Aarseth (1992), is implemented in the NBODY6 code. Here, the general idea is to divide the total acceleration on a star a_i in two parts, a distant ($a_{i,\mathrm{d}}$) and a nearest neighbour force contribution ($a_{i,\mathrm{n}}$):

$$a_i = a_{i,\mathrm{d}} + a_{i,\mathrm{n}}. \tag{2.16}$$

The distant part, $a_{i,\mathrm{d}}$, denominates the slowly varying force of very distant particles while the nearest neighbour part, $a_{i,\mathrm{n}}$, describes the high fluctuating potential of particles in the immediate vicinity of particle i. While the regular forces are typically weak the irregular forces strongly influence the particle.

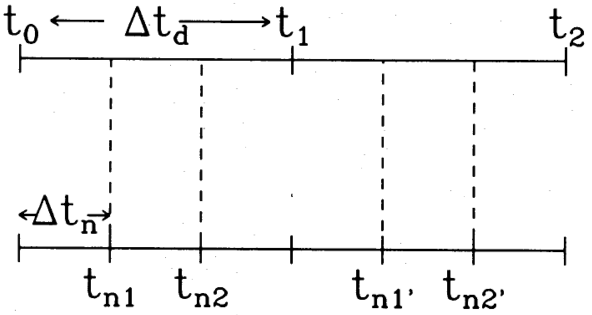

FIGURE 2.2: Sketch of a time sequence of the Ahmad-Cohen neighbour scheme for one particle taken from Makino & Aarseth (1992).

These two forces are now updated after different time intervals Δt_n and Δt_d with $\Delta t_n < \Delta t_d$. As indicated in Figure 2.2 at certain irregular time steps, $t_{n1}, t_{n2}, t_{n1'}, t_{n2'}, \dots$, only the nearest neighbour forces are calculated to higher orders while distant particle forces are predicted by Eq. 2.5 and Eq. 2.6. At regular time steps $t_0, t_1, t_2, \ldots$ all forces are determined to high orders.

The specification if a particle is a distant or a near neighbour particle is given due to its distance to the investigated particle r_n, which is determined at each regular time step. Aarseth (1985) defined the adjusted radius r_n^{new} as

$$r_n^{\mathrm{new}} = r_n^{\mathrm{old}} \left(\frac{n_p}{n} \right)^{1/3} \tag{2.17}$$

which is defined by n the number of nearest neighbours and n_p the predicted number of nearest neighbours, which is given by $n_p = n_{\max}(0.04C)^{1/2}$. Here, C is the density contrast $C \propto n/r_n^3$ and $n_{\max}$ the maximum number of nearest neighbours for which $2N^{1/2}$ has proven to be a good estimate in case of large N (Aarseth, 2003).

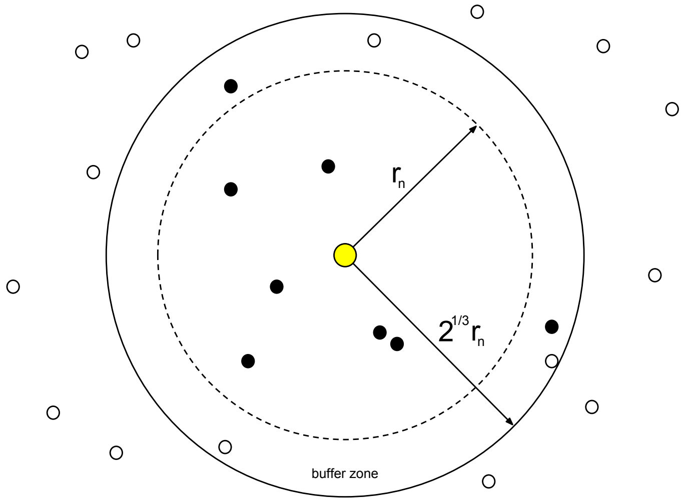

FIGURE 2.3: Sketch of the neighbour scheme for one particle. Particles with an irregular force contribution are shown as filled circles while open circles indicate regular force contributors. The yellow particle in the center represents particle i.

Moreover, particles within a buffer zone between r_n and the radius $2^{1/3}r_n$, which fulfill the requirement $\vec{r}_{ij}\vec{v}_{ij} < 0.1r_n^2/\Delta t_d$, are included in the list of nearest neighbours to assure a consideration of fast approaching particles. The classifications of the nearest neighbours in the radial sphere are illustrated in Figure 2.3.

Two-body regularization

Although above described methods reduce the computation time significantly, the investigations for close interactions like short period binary systems or very eccentric stellar orbits can considerably increase the computational effort. The small particle separations also result in strongly increasing gravitational forces, which lead to numerical difficulties.

One way to overcome this obstacle is a regularisation of the close interacting particles. In NBODY6 this is achieved by the so-called *KS-regularisation* introduced by Kustaanheimo & Stiefel (1965) and explained in detail in Aarseth (2003).

The binary is treated separately from the neighbour-force summation scheme. External perturbations are implemented in the binary's equation of motion by an external tidal field acceleration $\ddot{\vec{r}}_{\rm ext}$:

$$\ddot{\vec{R}} = -\frac{M\vec{R}}{R^3} + \ddot{\vec{r}}_{\rm ext}, \tag{2.18}$$

where $M = m_i + m_j$ is the total mass of the binary system and $\vec{R} = \vec{r}_i - \vec{r}_j$ is their relative coordinate. To avoid the singularity of type r^{-2}, a substitution of Eq. 2.18 by a differential time transformation of the form

$$dt = R^n d\tau \tag{2.19}$$

is generated, resulting in:

$$\vec{R}'' = \frac{nR''\vec{R}''}{R} - \frac{M\vec{R}}{R^{3-2n}} + R^{2n}\ddot{\vec{r}}_{\rm ext}, \tag{2.20}$$

where here $n = 1$ is chosen according to Sundman (1912) (for more details see Aarseth, 2003). In the following the external perturbation will be neglected and the one dimensional regularisation case will be exemplary discussed. These constraints lead to a reduction of Eq. 2.20:

$$x'' = x'^2/x - M. \tag{2.21}$$

The binding energy h of the orbiting stars per unit reduced stellar mass in one dimension is given by

$$h = \frac{\dot{x}^2}{2} - \frac{M}{x}. \tag{2.22}$$

A substitution of Eq. 2.22 with $\dot{x} = x'/x$ according to Eq. 2.19 yields

$$x'' = 2hx + M, \tag{2.23}$$

which is a regular differential equation of motion of a displaced harmonic oscillator, where the singularity is removed. By a coordinate transformation of $u^2 = x$ together with Eq. 2.22 this can be simplified to

$$u'' = \frac{1}{2}hu. \tag{2.24}$$

For two-dimensional coordinate systems these transformations exploit a mapping in the complex plane by a 2×2 matrix, a so-called *Levi-Civita matrix.* However, a generalisation in three-dimensions has been achieved by Kustaanheimo & Stiefel (1965), who used a 4×4 matrix and included a fourth fictitious coordinate and corresponding velocity. The advantage of the regularised equations of motion is that a significantly reduced number of integration time steps is required while the numerical stability of even circular orbits is improved (Aarseth, 2003).

Hardware acceleration

A significant acceleration of numerical simulations can be achieved by a parallelised force calculation. This can be achieved by either a connection of several *Central Processing Units* (CPUs) via network or by using special purpose hardware acceleration. One approach of the latter are the so-called *Gravity Pipe* (GRAPE) boards, which contained chips that were particularly designed for a fast parallelised calculation of gravitational forces. Nowadays, the chips provided in standard consumer graphic cards *Graphical Processing Units* (GPUs) become more convenient since they are less expensive. These were originally build to rapidly render three-dimensional graphics but became accessible for other operations with vendor supported programming interfaces like *Compute Unified Device Architecture* (CUDA), which is used in our case of Nvidia GPUs for the calculation of the regular forces. Because of the similarity to the GRAPE boards (from the users point of view) programs optimised for GRAPE can easily be adapted to GPUs.

One requirement for an efficient performance enhancement is a sufficient number of particles ($> 10^3$), since otherwise the communication of the processors becomes to time consuming compared to the computational benefit.

2.2 Modification of nbody6

2.2.1 Identification of encounter events

The NBODY6 code as such does not automatically provide information about the stellar interaction dynamics. In our work group the code NBODY6 has been extended by a definition to identify an encounter scenario. Moreover, a concept to determine the encounter properties like periastron, masses, eccentricity and the time the encounter periastron passage happened have been implemented.

The neighbour scheme of the NBODY6 code is used to identify the indices (and therefore mass ratio) of each encounter event by searching for the strongest perturbing star amongst the stellar neighbours. An exception are the KS-regularised pairs which are directly treated as strongest perturbers to each other. Since the individual star-disc encounter simulations are restricted to two-body perturbations, multiple encounter events are not considered, which might lead to an underestimation of the encounter influences on the disc properties.

An encounter is identified by the trajectory of the encounter being a nearly Keplerian orbit of concave shape and second, at least 10% of the orbit have to be fulfilled. If these requirements are achieved, the periastron distance is calculated. Since the simulation time is discretised the obtained closest separation is not necessarily the periastron distance (see Fig. 2.4). Especially in case of strong encounter events with small periods this becomes an issue. In polar coordinates the separation r can be interpolated as a Keplerian orbit by

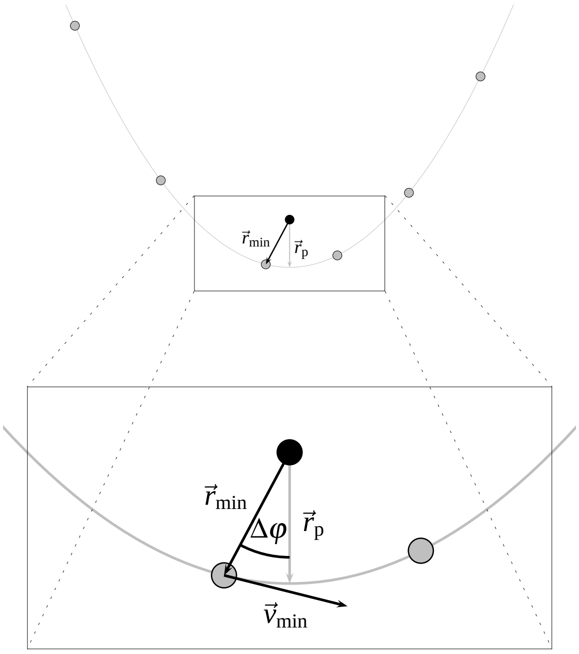

FIGURE 2.4: Sketch of an encounter taken from Olczak *et al.* (2012). The black circle indicates the position of the central star while the grey circles mark the position of the perturber at sequential time steps.

$$r = \frac{(1+\epsilon)r_{\rm peri}}{1+\epsilon\cos(\phi)} \tag{2.25}$$

with eccentricity ϵ and periastron distance $r_{\rm peri}$ (see Fig. 2.4). Note, that ϵ has not to be strictly equal in two different time steps due to numerical limitations. Accordingly, slight differences in the eccentricities are accounted for while for differences of more than 10% the encounter is rejected.

The periastron distance r_{peri} and eccentricity ϵ are obtained from the *Laplace-Runge-Lenz vector*

$$\vec{A} = \vec{v} \times \vec{l} - \frac{GM}{r}\vec{r}, \tag{2.26}$$

where $M = m_1 + m_2$ is the total mass of the encountering stars and $\vec{l} = \vec{r} \times \vec{v}$ defines the specific angular momentum. Both, $\vec{A}$ and $\vec{l}$, are conserved for an inverse-square central force. From $\vec{r}_{\text{min}}$ and $\vec{v}_{\text{min}}$, which are illustrated in Figure 2.4, we obtain

$$r_{\text{peri}} = \frac{|\vec{l}|^2}{GM\mu} \tag{2.27}$$

and

$$\epsilon = \frac{|\vec{A}|}{GM} \tag{2.28}$$

where $\mu = m_1 m_2 / M$ is the reduced mass.

To determine the time of the periastron passage, $t_{\text{peri}} = t_{\text{min}} + \Delta t$, one eliminates r_{peri} in Eq. 2.25 and uses the conservation of the specific angular momentum $l = r^2\dot{\phi}$ once again to obtain

$$\Delta t = \frac{r_{\text{peri}}^2(1+\epsilon)^2}{l} \int_0^{\Delta\phi} \frac{1}{(1+\epsilon\cos\phi)^2} d\phi. \tag{2.29}$$

In the following, a case differentiation for $\epsilon = 1$, $\epsilon < 1$, and $\epsilon > 1$ has to be performed.

Forming binaries, given by $\epsilon < 1$, are found to be transient systems that in most cases remain bound over a small number of orbits. However, around 1/4 of all stars undergo repeated fly-bys by a companion star. Here, simply the most disruptive encounter, which means the smallest periastron distance and eccentricity, is recorded, since the focus is on the relevance of stellar encounters. This might underestimate the disc losses but the effect will be discussed for the respective cases.

Finally, the result of the tracking procedure is a list of encounter parameters for each particle that contains information about the time, periastron distance, mass ratio and eccentricity of the encounter.

2.2.2 Instantaneous gas expulsion

As already outlined in Section 1.5, embedded clusters expel their remnant gas quickly and the the star formation process ceases. In Chapter 5 cluster models with focus on the subsequent dynamical cluster evolution will be investigated. In this case the cluster is set up under the condition of a recent expulsion of the remnant gas. A simple way to mimic such an instantaneous expulsion process is to adapt the virial ratio $Q = T/|W|$, where T is the kinetic energy, and W the potential energy, to the modified total energy of the cluster, which has been intensively discussed in Goodwin (1997).

Such simplifications avoid the actual modulation of the natal gas since simply the stellar velocity distribution has to be adjusted according to the virial state. The correction term for the velocities is simply obtained by a comparison of the total cluster energies. Here, the cluster energy before gas expulsion is given by

$$E = T + W = \frac{1}{2} M_{\mathrm{tot}} \sigma^2 - \frac{G M_{\mathrm{tot}}^2}{2R_0} = Q_0 M_{\mathrm{tot}} \sigma_{\mathrm{eq}}^2 - \frac{G M_{\mathrm{tot}}^2}{2R_0} = \frac{G M_{\mathrm{tot}}^2}{2R_0} \left(Q_0 - 1\right), \tag{2.30}$$

where M_{tot} is the total initial cloud mass, R_0 is the average radius of the cluster, $\sigma^2 = 2Q_0\sigma_{\mathrm{eq}}^2$ is the velocity dispersion of the stellar cluster members, and $\sigma_{\mathrm{eq}}^2 = |W|/M_{\mathrm{tot}} = GM_{\mathrm{tot}}/2R_0$ is the velocity dispersion if the cluster is in virial equilibrium ($Q = 0.5$) with the initial virial ratio Q_0. It can be seen that the cluster is initially unbound ($E > 0$) if the virial ratio is $Q_0 > 1$.

However, if the gas is expelled the total cluster mass decreases which results in a lower total energy after the gas loss, given by

$$E = \frac{1}{2} \epsilon M_{\mathrm{tot}} v^2 - \frac{G \epsilon^2 M_{\mathrm{tot}}^2}{2R_0} = Q_0 \epsilon M_{\mathrm{tot}} \sigma_{\mathrm{eq}}^2 - \frac{G \epsilon^2 M_{\mathrm{tot}}^2}{2R_0} = \frac{G \epsilon M_{\mathrm{tot}}^2}{2R_0} \left(Q_0 - \epsilon\right), \tag{2.31}$$

with star formation efficiency $\epsilon = M_{\mathrm{stars}}/M_{\mathrm{tot}}$. The appendant virial ratio given by

$$Q = \frac{Q_0}{\epsilon} \tag{2.32}$$

specifies the modified situation of the cluster.

Equation 2.32 has been implemented in the NBODY6 code as a correction term for the initial virial ratio. Thus, the cluster can be modelled as initially out of virial equilibrium by simply supplying the global star formation efficiency.

In contrast to the instantaneous gas expulsion model, which on the evolution of massive clusters after the expulsion of the gas, two different approaches will be shortly discussed in Appendix D.

2.3 Cluster setup

The particles representing the cluster stars in the simulation have to be assigned initial masses, positions, and velocities. The general setup of the particles will be introduced in the following.

Initial mass function

Here, we tried to model a realistic distribution of stellar masses in the cluster instead of the often used single-mass distribution. Despite the higher computational effort the cluster evolution is largely determined by the initial mass function (IMF). Hereby, the IMF, $\xi(m)$, describes the number of stars per unit mass with $\xi(m)\,dm$ giving the number of single stars in the mass interval m to $m + dm$. Thus, the total number of stars with masses between m_1 and m_2 is obtained by

$$N(m_1, m_2) = \int_{m_1}^{m_2} \xi(m) dm. \tag{2.33}$$

In contrast to the present-day mass function (PDMF), the IMF describes the distribution of stellar masses before they start losing mass by outflows or are even completely destroyed in a supernovae explosion. Therefore, all used IMF's have been found empirically from observed distributions of stellar masses in young clusters. Salpeter (1955) found a first estimate of the initial mass function for the mass range $0.4 < m/\,\mathrm{M}_\odot < 10$, of the form

$$\xi(m) \propto m^{-2.35} \tag{2.34}$$

indicating that massive stars in stellar clusters are rare in number. While Salpeter's approach could be confirmed for high-mass stars by later observations (e.g. Massey & Hunter, 1998) it had to be modified for the low-mass regime, where a flattening of the distribution slope is observed. Currently used IMFs covering the low-mass regime are that by Chabrier (2003b), who assumes a log-normal distribution for stellar masses $m \leq 1\,\mathrm{M}_\odot$, given by

$$\xi(\log m)_{m\leq 1} = 0.158 \times \exp\left(-\frac{(\log m - \log 0.079)^2}{2\cdot 0.69^2}\right) (\log\,\mathrm{M}_\odot)^{-1}\,\mathrm{pc}^{-3} \tag{2.35}$$

(see also Chabrier, 2003a), and that by Kroupa (2001), given by a broken power law distribution function

$$\xi(m) \propto \begin{cases} m^{-0.3} & 0.01 \leq m/\,\mathrm{M}_\odot < 0.08 \\ m^{-1.3} & 0.08 \leq m/\,\mathrm{M}_\odot < 0.5 \\ m^{-2.3} & 0.5 \leq m/\,\mathrm{M}_\odot. \end{cases} \tag{2.36}$$

However, due to their low luminosities low-mass stars are difficult to find, which might lead to an underestimation in this regime.

Throughout this study, the latter approach will be used. Furthermore, here the lower limit for the stellar mass has been set to the hydrogen burning limit of $m_{\mathrm{min}} = 0.08\,\mathrm{M}_\odot$ making the plain Kroupa (2001) IMF a sufficient distribution function for this study. Stellar masses of $m_{\mathrm{star}} < 0.08\,\mathrm{M}_\odot$ are neglected since they contribute only little to the stellar dynamics and the distribution function is apparently continuous but flattens across the hydrogen burning limit (see Eq. 2.36 and e.g. Allen *et al.*, 2005). The maximum stellar mass is set to the accepted upper mass limit $m_{\max} = 150\,\mathrm{M}_\odot$ (Figer, 2005; Oey & Clarke, 2005; Weidner & Kroupa, 2006). Even though higher stellar masses of $165 - 320\,\mathrm{M}_\odot$ have been recently suggested for massive starburst clusters like R136 (Crowther *et al.*, 2010), many of such massive stars turned out to be unresolved binaries (Damineli *et al.*, 2000) (see also Zinnecker & Yorke, 2007, for a review).

Stellar number density distribution

A characteristic quantity, largely determining star-disc encounters in a cluster, is the stellar number density distribution. In this study, different evolutionary time steps of massive stellar population are investigated, which require a sophisticated setup of individual density profiles dependent on its prior formation history.

For the setup of the embedded cluster models (Section 4) the stars have been spatially distributed according to a density that is representative for an initial ONC density distribution. Observations of today's ONC density distribution show that it can be approximated by an isothermal profile ($\propto r^{-2}$) in the outer parts (McCaughrean & Stauffer, 1994; Hillenbrand & Hartmann, 1998) and a flat stellar density profile of the form $\rho_{\mathrm{core}} \propto r^{-0.5}$ in the cluster core (Scally *et al.*, 2005).

Since the initial distribution of gas in molecular clouds, which are the birthplaces of the forming stars (Section 1.1), can be assumed to be isothermal (Larson, 2003), it seems reasonable to start out with a r^{-2} dependence for the initial stellar distribution of very young, embedded star clusters (Scally *et al.*, 2005; Olczak *et al.*, 2006, 2010). Here, an isothermal density model with an initially slightly increased density in the cluster core region is used, given by

$$\rho_{\mathrm{initial}}(r) = \begin{cases} \rho_0 \cdot r^{-2.3} & r \leq R_{\mathrm{core}} \\ \rho_0 \cdot r^{-2.0} & R_{\mathrm{core}} < r \leq R_{\mathrm{cluster}} \\ 0 & R_{\mathrm{cluster}} < r \end{cases} \tag{2.37}$$

where $\rho_0 = 3.1 \times 10^2\,\mathrm{pc}^{-3}$, $R_{\mathrm{core}} = 0.2\,\mathrm{pc}$, and $R_{\mathrm{cluster}} = 2.5\,\mathrm{pc}$. It is a reliable initial distribution since it turns out, that after 1 Myr of dynamical evolution, the estimated age of the ONC, the model matches observations of today's ONC density distribution (Olczak *et al.*, 2006) reasonably well.

While starting out with an isothermal stellar distribution seems to be a good approach to set up very young embedded star clusters (Scally *et al.*, 2005; Olczak *et al.*, 2006, 2010), the stellar density distribution in the core of more dynamically evolved clusters is found to be much flatter (nearly constant) than given by an isothermal sphere.

Thus, for the setup of evolved clusters prior to the expansion phase (Section 5), the stellar content is distributed according to a King profile of $W_0 = 9$. In contrast to the Plummer model, which is one of the most commonly used stellar profiles for numerical investigations due to its analytical simplicity (e.g. Aarseth *et al.*, 1974; Kroupa *et al.*, 2001; Goodwin & Bastian, 2006; Bastian & Goodwin, 2006; Baumgardt & Kroupa, 2007; Allison *et al.*, 2009; Brasser *et al.*, 2012), the family of King models provides not only good fits to many observed old clusters, like globular clusters, but are also applicable for young embedded clusters like the present ONC ($W_0 = 9$, Hillenbrand & Hartmann, 1998) or even young starburst clusters like Arches (Initially: $W_0 = 3^\dagger$, Present-day: $W_0 = 7$, Harfst *et al.*, 2010) and NGC 3603 ($W_0 = 8^\ddagger$, Nürnberger & Petr-Gotzens, 2002; Sung & Bessell, 2004), although their global relation to young massive clusters remains unclear (Portegies Zwart *et al.*, 2010). In general, King models with $W_0 \geq 7$ can be denominated as characteristically for young clusters, due to their concentrated but flattened core.

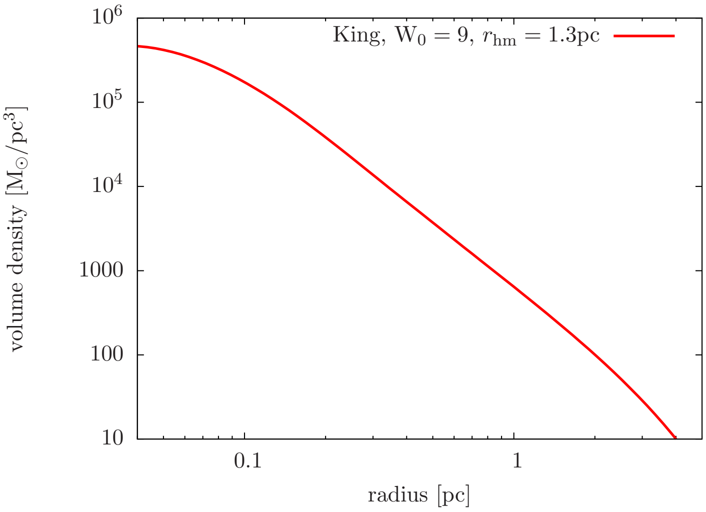

FIGURE 2.5: Shown is the cluster (mass) volume density as a function of the distance to the cluster center. A King-shaped initial distribution profile with $W_0 = 9$, half-mass radius $r_{\rm hm} = 1.3$ pc (King radius $r_0 = 0.13$ pc), and containing 30 000 stars is shown in solid red

The King profile of $W_0 = 9$ is shown in Figure 2.5, where the cluster volume density is

---

[†] Private communication with S. Harfst and C. Olczak revealed that an initial King Parameter of $W_0 = 3$ for the Arches Cluster only leads to slightly improved profiles than initial parameters of $3 < W_0 \leq 7$. Higher King parameters of $W_0 > 7$ were not even tested but seem in a first effort also very likely, especially when considering primordial mass segregation.

[‡] Nürnberger & Petr-Gotzens (2002) find a concentration of $c = 1.75$ which can be converted to $W_0 \approx 8$ according to Figure C.1. Sung & Bessell (2004) also mention that the King profile fitting is very sensitive to the central density, which easily leads to a potential underestimation of W_0.

plotted as a function of the distance to the cluster center. The red line indicates the King-shaped distribution given for 30 000 stellar members and half-mass radius $r_{\rm hm} = 1.3\,{\rm pc}$ (King radius $r_0 = 0.13\,{\rm pc}$, Eq. C.6) as it will be used in Section 5. While the density distribution continuously decreases towards the cluster outskirts, it flattens for the inner 0.1 pc (see Sec. 4.2 for dynamical evolution of a stellar cluster).

Apart from providing suitable density profiles for evolved clusters, it turns out that King models also fit the nearly isothermal profile used to set up embedded clusters (Eq. 2.37) reasonably well assuming a King Parameter of $W_0 = 12$. Figure 2.6 shows the isothermal volume density profiles according to Equation 2.37 (black lines) and the King $W_0 = 12$ profile (red lines). It can be seen that the initial profiles (solid lines) as well as the evolved profiles after 1 Myr (dashed lines) are consistent with each other. Only minor deviations are given due to the sharp edge of the isothermal distribution in the outer cluster parts ($r = 2.5\,{\rm pc}$).

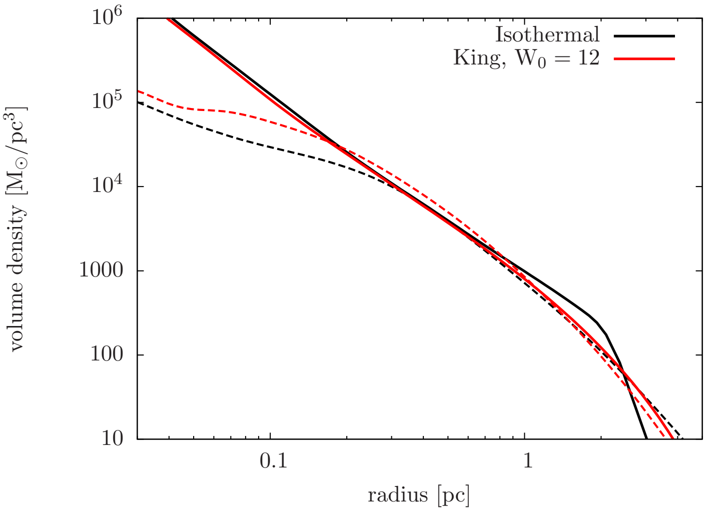

FIGURE 2.6: Shown is the cluster (mass) volume density as a function of the distance to the cluster center. A King-shaped initial distribution profile with $W_0 = 12$, $r_{\rm hm} = 1.3\,{\rm pc}$, and containing 30 000 stars is shown in red and a nearly isothermal distribution (Eq. 2.37) in black. The solid lines present the initial and the dashed lines the profiles after 1 Myr.

Having modelled a stellar density profile, all stars are distributed as being initially single, no primordial binaries are included. This approach will presumably underestimate the number of ejections from the cluster, since apart from an increased destruction rate of the stellar discs in tight binaries, the cluster dynamics are usually influenced by strong few-body interactions (Hills, 1975; Heggie, 1975). Actually, the binary fraction in the ONC today is found to be around 50% (Duquennoy & Mayor, 1991; Köhler *et al.*, 2006). The primordial binary frequency could be even higher (≈ 74% Kaczmarek *et al.*, 2011) as dynamical interactions can destroy wide binaries very quickly. Hence, excluding primordial binaries presumably has a non-negligible effect, so that further studies are needed to quantify the influence on the disc destruction rates. However, binaries are not only destructed but also form during the cluster evolution, especially if there exist no primordial binaries (Pfalzner & Olczak, 2008). Here, such evolutionary binary formations are implemented in the encounter statistics by considering the most disrupting fly-by (Section 2.2.1). Primordial binaries have been neglected due to the high computational effort but might be an improvement for future investigation.

Velocity distribution

After distributing the stars within the cluster and assigning masses to them, the last parameter to be attached to the stars is their velocity. The motion of a large number of stars in a cluster can be approximated by that of molecules in a gas. Hereby, the bodies are considered as point masses interacting via point center forces. However, these forces differ considerably. While the forces between gas molecules are rather violent, being significant on short distances and timescales, the motion of stars in a cluster is influenced by the mean potential generated by the overall cluster density structure (for more details see Binney & Tremaine, 2008). Assuming a cluster consisting of 10^4 stellar members and a crossing time in the order of 10^5 yr, physical collisions between two interacting stars become significant on time scales of the order 10^7 yr (Eq. 1.8). Consequently, for the short-term evolution the stellar clusters can be approximated as collision-less systems, which here means only elastic interactions are considered like in case of an ideal gas.

The velocity distribution of molecules in a thermalised ideal gas is well-described by a Maxwellian velocity distribution given by

$$f(\vec{v}) = N \exp\left(-\frac{\vec{v}^2}{2\sigma^2}\right), \tag{2.38}$$

where $f(\vec{v})dv_x dv_y dv_z$ is the probability of a particle with velocity between $\vec{v}$ and $\vec{v}+d\vec{v}$, N the number of particles, and σ the velocity dispersion. For an isothermal sphere σ is constant throughout the sphere. Moreover, from Equation 2.38 follows that

$$f(\vec{v}) \propto f(v_x)f(v_y)f(v_z). \tag{2.39}$$

Here, the Maxwell distribution is obtained by a random number sampling of the Gaussian deviates for each velocity component. A convenient method for the setup is described in Box & Muller (1958). First, two random numbers, x_1 and x_2, that are uniformly distributed in the interval $[0,1]$ are generated and then used for a transformation of the form

$$y_1 = \sqrt{-2\ln x_1}\cos(2\pi x_2) \tag{2.40}$$

$$y_2 = \sqrt{-2 \ln x_1} \sin(2\pi x_2) \tag{2.41}$$

which have a Gaussian distribution with a standard deviation of one. A numerically faster and more robust calculation is given if polar coordinates ($y_1 = r \cos \phi$, $y_2 = r \sin \phi$) are assumed, which results in $r = \sqrt{y_1^2 + y_2^2} = \sqrt{(-2 \ln x_1)}$ and $\phi = 2\pi x_2$.

Statistical robustness

It is indispensable to perform multiple simulations (N_{sim}) for each individual cluster model to obtain statistically robust results. Therefore, a set of random initial stellar positions, velocities and masses has been achieved for each run, which are analysed and averaged in a subsequent step. It turned out that tracking about 500 000 stellar trajectories leads to an error of $< 3\%$ for the present results. This means for an initial number of stars $N_{\mathrm{star}} = 1\,000$ around 500 simulations were preformed while around 15 simulations were performed in case of $N_{\mathrm{star}} = 30\,000$. However, due to an inhomogeneous distribution of stars as well as single stellar masses within the cluster certain parameter sub-samples like the high-mass regime might lead to slightly increased statistical variations, which will be discussed in the respective cases.

2.4 Diagnostic aspects

The final step of the data analysation is a combination of the results from the star-disc encounter parameter study and the dynamical cluster simulations. This will be done in the diagnostic step. Two approaches have been implemented to merge the parameter study results with the dynamical encounter parameters recorded from the cluster simulations, like the minimum stellar separations, the stellar mass ratios and the eccentricities: (i) An approximation of the disc losses by a fit formula (as provided in Section 3.2.4 - see Eq. 3.4 and Eq. 3.4) or (ii) a first-order interpolation of the tabulated individual disc loss results.

The fitting formula is strictly valid just in a limited mass ratio regime $m_2/m_1 < 20$ as will be discussed in detail in Section 3.2.4. However, an interpolation method has been preferred in this study since it significantly improves the loss estimates for the large parameter domain, in particular for high mass ratios. Therefore, a two-dimensional interpolation of first order for the discrete mass ratio and periastron quantities, respectively, has been implemented that generalise the losses from the tabulated parameter study results.

Another important parameter which yet has to be included is the eccentricity ϵ. Here, a fit formula for the dependence on the eccentricity has been adapted from Olczak *et al.* (2010):

$$\frac{\Delta x}{x} = \frac{\Delta x_0}{x_0} \cdot \exp\left(-0.12(\epsilon - 1)\right) \cdot \left(0.83 - 0.015(\epsilon - 1) + 0.17 \exp\left(0.1(\epsilon - 1)\right)\right) \qquad (2.42)$$

where $\Delta x_0/x_0$ is the disc mass (or angular momentum) loss obtained by either Eq. 3.4, Eq. 3.4 or interpolating the single encounter results. $\Delta x/x$ gives the final disc loss in dependence on the eccentricity. Equation 2.42 has been proven valid for varying initial disc-mass distribution results. It has been tested for the mass losses by averaging over several simulations with different seeds for the initial particle distribution. The errors lie typically in the range of $4 - 5\,\%$.

Since parabolic encounters lead to maximum losses, accounting for the eccentricity will in general reduce the overall disc losses.

3 Disc-mass distribution in star-disc encounters

In this part of the thesis the focus is on the effect of the initial disc-mass distribution in single star-disc encounters between two interacting stars, where one star is initially surrounded by a circumstellar disc. A parameter study has been carried out in the framework of my diploma thesis and has been extended here to an increased parameter range to cover below investigated stellar cluster properties. First, a brief introduction into the numerical methods and parameter range used in this study will be given. Afterwards the results of the simulations will be presented including a fit formula for the mass and angular momentum loss depending on the initial disc-mass distribution index p, followed by a summary and discussion.

3.1 Setup and method

The encounter between a disc-surrounded star with a secondary star is modelled using a tree algorithm (see Appendix B and also Pfalzner, 2003). In the here used simulations, only one star is initially surrounded by a disc. However, previous investigations have shown that star-disc encounters can be generalised to disc-disc encounters as long as there is no significant mass exchange between the discs (Pfalzner *et al.*, 2005a). In the case of a mass exchange, the discs can be to some extent replenished, such that for very close encounters the mass loss determined in this study would be slightly overestimated.

The disc is represented by 10 000 pseudo-particles, distributed according to a given particle distribution $\propto r^{-b}$. Choosing this relatively small number of simulation particles is motivated by the aim to cover a large encounter parameter space. However, performing test simulations with 50 000 particles shows that the lower resolution is sufficient for measuring the properties investigated here.

Initially, the simulation particles move on Keplerian orbits around the central star. The disc extends from an inner gap of 10 AU to 100 AU. The inner cut-off avoids additional complex calculations of direct star-disc interactions and saves computation time. Any pseudo-particle that reaches a sphere of 1 AU around the central star is removed from the simulation and stated in a commonly used simplified approach as having been accreted onto

variable	values
Outer disc radius, $r_{\rm disc}$	100 AU
Inner disc radius, $r_{\rm i,disc}$	10 AU
Number of particles, $n_{\rm part}$	10 000 (50 000)
Disc mass, $m_{\rm disc}$	$10^{-4}\,{\rm M}_\odot$ ($10^{-3}\,{\rm M}_\odot$)
Particle distribution index, b	0, ($\frac{7}{4}$)
Mass distribution index, p	0, $\frac{1}{2}$, 1, $\frac{7}{4}$
Rel. perturber mass, M_2/M_1	$0.1 - 1875$
Rel. periastron distance, $r_{\rm peri}/r_{\rm disc}$	$0.1 - 50$
Eccentricity, ϵ	1
Simulation time, $t_{\rm end}$	$\sim 3\,000$ yrs

TABLE 3.1: Initial conditions for all simulations

the star (Bate *et al.*, 2002; Vorobyov & Basu, 2005; Pfalzner *et al.*, 2008). The vertical density distribution in the disc follows

$$\rho(r,z) = \rho_0 \exp\left(-\frac{z^2}{2H^2(r)}\right), \tag{3.1}$$

where ρ_0 is the unperturbed mid-plane particle density on the equatorial plane with $\rho_0 \propto r^{-(b+1)}$, where b is the particle distribution index. $H(r)$ is the vertical half-thickness of the disc (see Pringle, 1981), which is represented by $H(r) = 0.05\,r$ according to a temperature profile of $T = T_0 \cdot r^{-1}$ with $T = 20$K at the inner edge of the disc. A summary of the disc properties can be found in Table 3.1.

The total simulation time of $t_{\rm end} \approx 3\,000$ yrs for each encounter corresponds to three orbital periods of the outermost particles in the investigated standard disc with size $r_{\rm disc} = 100$ AU around a $1\,{\rm M}_\odot$ star. This time span was found to be adequate for the calculation of all relevant quantities.

The discs obtained at the end of the simulations continue to develop in the sense that taking into account viscous forces, the eccentric orbits of perturbed disc pseudo-particles would re-circularise on timescales probably in excess of 10^5yr. However, bound and unbound material can be clearly distinguished shortly after the encounter.

In this present study, we are interested in protoplanetary discs, which are usually of low mass compared to protostellar discs (Bate, 2011). Here low-mass discs mean $m_{\rm disc} \ll 0.1M_1$, where M_1 is the mass of the disc surrounded star. The actual adopted disc-mass value is $10^{-4}M_1$. However, another case of $m_{\rm disc} = 10^{-3}M_1$ was tested and no differences in the result when including self-gravity in the simulations have been found. In addition, test simulations including pressure and viscous forces have been performed using a SPH code (for a description of the code see Pfalzner (2003)), but only found negligible differences ($< 3\%$) in the results. Therefore, in most of the here used simulations self-gravitation and viscous forces were neglected in favour of higher computational performance.

The actual values of mass and angular momentum loss induced by the encounters were obtained by averaging over several simulations with different seeds for the initial particle distribution. The errors in the mass and angular momentum losses were determined as the maximum differences between the simulation results. They typically lie in the range of $2 - 3\,\%$.

In addition to these obvious performance benefits, the possibility to neglect the self-gravitation, pressure, and viscous forces has allowed us to optimise the computation time by treating the disc particles as pseudo-particles without a fixed mass during the simulation.

The standard method for generating the initial disc-mass distribution in the simulations is to assign the same mass to each pseudo-particle (e.g. Boffin *et al.*, 1998; Pfalzner, 2004; Olczak *et al.*, 2006). This approach involves the performance of a whole suite of simulations for each variation in the initial disc-mass distribution. In contrast, here, the different disc-mass distributions are realised by using a fixed pseudo-particle distribution and assigning their masses *after* the simulation process according to the desired density distribution in the disc. The implementation of this flexible numerical scheme allows us to use one suite of simulations for any initial disc-mass distribution. Note, that the post-processing of the particle mass is only possible because of the restriction to low-mass discs, where self-gravitation and viscous forces can be neglected.

The particle masses are assigned to each pseudo-particle in the diagnostic step to calculate the encounter-induced losses and final mass distributions, which both depend on the initial distribution. For the example of a power-law disc-mass distribution with index p, the mass of a particle m_i depends on its initial radial position in the disc r_i, the total disc mass m_disc, the number of pseudo-particles n_part, their radial positions r_j, and the underlying power-law particle distribution of index b. Since the number of pseudo-particles is limited, the discrete particle masses m_i are described by

$$m_\mathrm{i} = \left(\sum_{j=1}^{n_{part}} r_j^{-p+b} \right)^{-1} \cdot m_\mathrm{disc} \cdot r_\mathrm{i}^{-p+b}. \tag{3.2}$$

The resulting independence of the mass and the particle distributions allows to improve the resolution of the simulations by initially placing most of the pseudo-particles where the interaction between the stars and disc is strongest.

In the present simulations, a constant particle distribution ($b = 0$) has been adopted.

This is done because the effects on mass and angular momentum are largest at the outskirts of the disc. Using a constant pseudo-particle density ($b = 0$) throughout the disc ensures a higher resolution in the outer parts, even for steep mass density profiles, than for the standard approach. In contrast, if one were interested in processes that mainly concern the inner parts of the disc, such as accretion, it would be more accurate to use not a constant particle distribution but one that guarantees a high resolution close to the star ($b \geq 1$).

The method of a posteriori mapping of the particle masses has been tested against representative test calculations for different initial pseudo-particle distributions and against the standard method of fixed pseudo-particle masses. The differences in the results were negligible, thus justifying the generalisation of the results for a constant particle distribution ($b = 0$).

Apart from the density distribution, the outcome of an encounter depends on the relative periastron distance $r_{\mathrm{peri}}/r_{\mathrm{disc}}$ and the mass ratio of the involved stars M_2/M_1, where M_2 is the mass of the perturbing star. The parameter space that has been investigated - for a summary see Table 3.1 - is chosen in such a way that it spans the entire range of encounters likely to occur in a typical young cluster. The lower limit of the perturber mass ratio is chosen to be $M_2/M_1 = 0.1$ as for smaller mass ratios the influence of the perturber becomes insignificant. The upper limit, $M_2/M_1 = 1875$, is determined by the maximum possible mass ratio expected to occur in a massive star cluster. It corresponds to the ratio between the hydrogen burning limit, which defines the lowest stellar mass of $0.08\,\mathrm{M}_\odot$, and $150\,\mathrm{M}_\odot$, the accepted upper stellar mass limit (Figer, 2005; Oey & Clarke, 2005; Weidner & Kroupa, 2006). The inner edge of the disc marks the lower value of $r_{\mathrm{peri}}/r_{\mathrm{disc}} = 0.1$. The upper value of $r_{\mathrm{peri}}/r_{\mathrm{disc}}$ corresponds to the distance where perturbations become negligible and therefore depends on the perturber mass.

3.2 Results

Although in principle any mass distribution of circumstellar discs can be studied, four exemplary disc-mass distributions are investigated here in more detail. To cover the entire range of numerically and observationally determined disc-mass distributions, a constant mass distribution ($p = 0$) is considered, representing the lower boundary of expected distributions, and a $p = 7/4$ distribution, providing an upper limit. Additionally, a $p = 1$ distribution is investigated for comparison to previous star-disc encounter results and a $p = 1/2$ distribution, which is in the range of analytical results for low-mass discs (Shakura & Sunyaev, 1973; Pringle, 1981) and similar to results found in recent investigations of magnetised material (see Sec. 1.1).

The present investigation focuses on coplanar, prograde encounters on parabolic orbits

($\epsilon = 1$) (see example in Fig. 3.1*a*) . Previous studies have shown that even for clusters as dense as the inner ONC region, most encounters in star clusters are expected to be close to parabolic (Larson, 1990; Ostriker, 1994; Olczak *et al.*, 2010). These parabolic encounters provide the strongest impact of the perturber on the disc, since for higher eccentricities the perturber only interacts briefly with the star-disc system and is, therefore, unable to influence the disc significantly. The limitation to a certain orientation is more restricting, as inclined and retrograde encounters can lead to lower losses in mass (Heller, 1993; Hall *et al.*, 1996; Clarke & Pringle, 1993). However, Pfalzner *et al.* (2005b) showed that up to an inclination of 45° the mass loss of the disc is only slightly smaller than for a coplanar orbit. This means that the results have to be regarded as an upper limit for encounters at different inclinations.

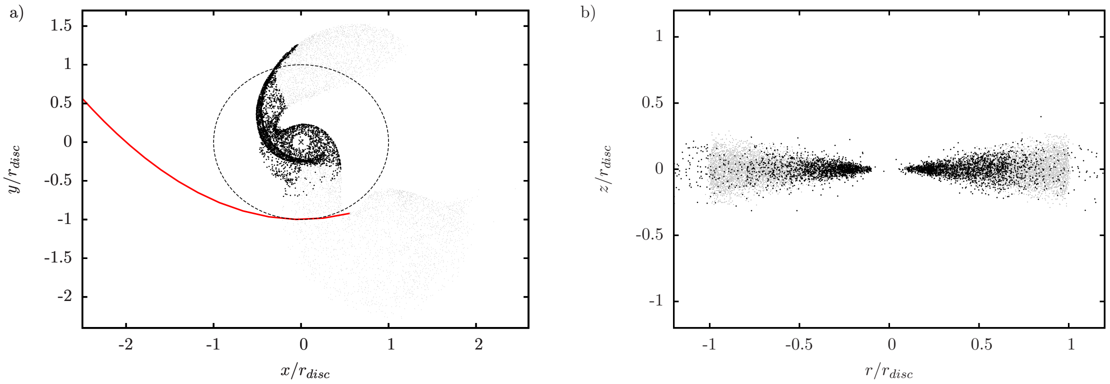

FIGURE 3.1: The dashed line in a) shows the boundaries of the initial disc while the solid red line indicates the trajectory of a grazing perturber ($r_{\text{peri}}/r_{\text{disc}} = 1$) of equal mass ($M_2/M_1 = 1$). Material that resides within the disc after the perturbation is marked as black squares, while material that is in the end either bound to the perturbing star, unbound, or accreted is shown as grey dots. Note, that the simulations were performed in three dimensions as can be seen in b).

3.2.1 Surface density distribution

To achieve a clearer understanding of the re-distribution of the disc material during a star-disc encounter that depends on the initial disc-mass distribution, first, the focus is on the evolution of the surface density profiles. In Fig. 3.2 is presented how the evolution of the surface density in star-disc encounters depends on the periastron distance for both a constant initial disc-mass distribution ($p = 0$) and one with a steep initial distribution ($p = 7/4$). It shows the mass distributions $\Sigma(r)$ before (solid black line) and after a penetrating ($r_{\text{peri}}/r_{\text{disc}} \leq 1$, dashed blue line), grazing ($r_{\text{peri}}/r_{\text{disc}} = 1$, dashed red line), and distant encounter ($r_{\text{peri}}/r_{\text{disc}} = 3$, dashed green line). Here, the relative perturber mass was chosen to be $M_2/M_1 = 1$.

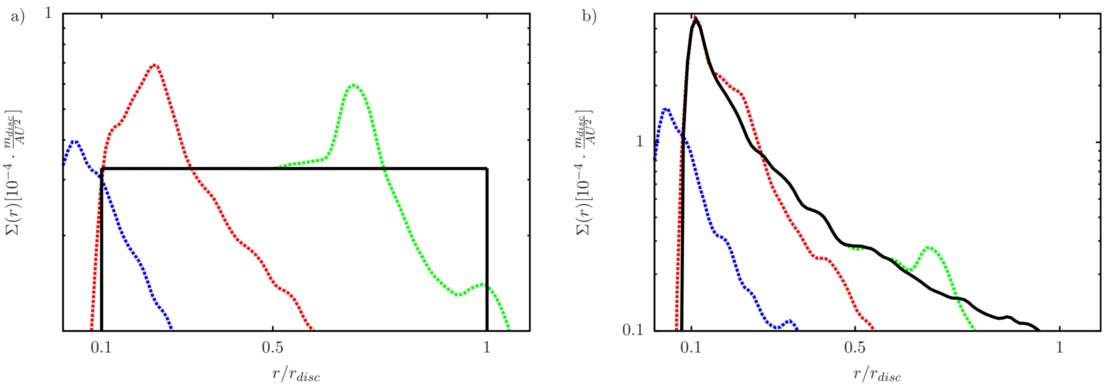

FIGURE 3.2: Initial (solid black line) and final surface densities in case of a) initially constant distributed disc material of $p = 0$ and b) a steep distribution of $p = 7/4$. In both plots non-penetrating ($r_{\rm peri}/r_{\rm disc} = 3$, dashed green line), grazing ($r_{\rm peri}/r_{\rm disc} = 1$, dashed red line), and penetrating encounters ($r_{\rm peri}/r_{\rm disc} = 0.1$, dashed blue line) are plotted for a perturbing star of equal mass ($M_2/M_1 = 1$).

As known from previous investigations (Hall, 1997; Larwood, 1997), an encounter reduces the density in the outer parts of the disc by transporting some part of the outer disc material inwards while another fraction of material migrates outwards. The latter might become both captured by the perturber and unbound if the encounter is strong enough. These effects become more pronounced for small $r_{\rm peri}/r_{\rm disc}$ and/or large M_2/M_1. However, the actual amounts depend on the initial disc-mass distribution. In an equal-mass distant encounter ($r_{\rm peri}/r_{\rm disc} = 3$), most of the perturbed disc material is pushed inside the disc towards smaller disc radii. In this case, 12.5 % of the total disc mass migrates inwards for an initial constant disc-mass distribution ($p = 0$), whereas it is only 6 % for an initial $p = 7/4$.

The effects of different initial disc-mass distributions become even more obvious for closer encounters such as grazing (dashed red lines in Fig. 3.2) or penetrating fly-bys (dashed blue lines in Fig. 3.2). Here, the migration process and also the differences between the initial distributions are dominated by material moving outwards. In the case of a grazing encounter and an initially constant disc-mass distribution, about 60 % of the disc mass becomes unbound. However, in addition about 10 % of the total disc mass can be found outside the initial disc radius of 100 AU that is still bound to the central star. In contrast, for the steep $p = 7/4$-mass distributions only ~ 30 % of the disc mass becomes unbound but again ~ 10 % is bound but situated outside 100 AU. It can be concluded that the outer disc material is generally separated from the disc for grazing encounters, while material initially located inside the disc ($r/r_{disc} \leq 0.7$) is re-distributed but remains bound to the central star. Hence, prominent differences in encounter-induced disc losses for the investigated disc-mass distributions are expected for strong perturbations of the outer disc parts. In penetrating encounters, part of the disc material is pushed further inside the disc resulting in a higher surface density in the inner disc regions. In extreme cases, the disc loss can increase to $> 90\,\%$ so that the final disc structure can no longer be regarded as a disc.

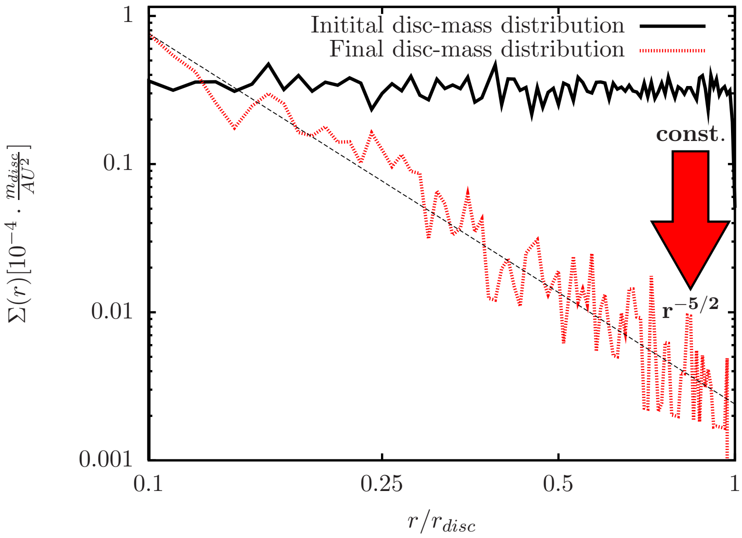

FIGURE 3.3: Initial ($p = 0$, solid black line) and final surface density after an encounter of $M_2/M_1 = 5.0$ and $r_{\rm peri}/r_{\rm disc} = 0.7$ (dotted red line). The dashed straight line represents a slope of $p = 5/2$.

In nearly all cases, a steepening of the density profile is the general effect of an encounter. The degree of steepening depends on the mass ratio, periastron distance, and the initial disc-mass distribution. Fig. 3.3 shows that even initially flat distributed disc-material ($p = 0$) can be redistributed into a surface density profile steeper than $p \approx 2$.

How is the vertical structure of the disc influenced by an encounter? As only coplanar encounters are investigated here, the answer is: surprisingly little. Fig. 3.1*b* shows the vertical particle profile of a strongly perturbed disc after a penetrating encounter of $M_2/M_1 = 1$. The main effect of the encounter is a decrease in the number of particles in the outer disc regions. In these parts of the disc, the resolution is relatively low, but owing to the here used constant particle distribution ($b = 0$) it is significantly higher than in previous investigations using r^{-1} particle distributions in their simulations.

In a few special cases where material is pushed moderately inwards, even partially negative distribution indices as low as $p = -1$ can be the end product of an encounter (Fig. 3.4). The effect is most prominent in the inner part of perturbed discs with initially constant distributed disc material. Nonetheless, the outer parts of the disc always have a distribution with positive index, $p > 0$.

This could perhaps explain the negative indices observed for some discs. Observations remain limited to measuring only part of the radial extension of the entire disc. If this were to be the range where negative indices prevail, one would wrongly extrapolate negative indices for the whole disc, while the overall index of the disc would remain positive.

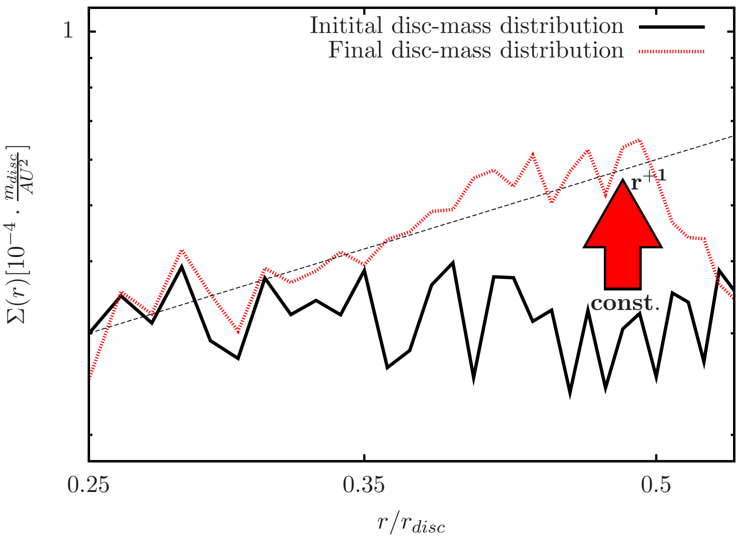

FIGURE 3.4: Initial ($p = 0$, solid black line) and final surface density after an encounter of $M_2/M_1 = 1.0$ and $r_{\text{peri}}/r_{\text{disc}} = 2.0$ (dotted red line). The dashed straight line represents a slope of $p = -1$.

3.2.2 Relative mass loss

In addition to changing the shape of the disc-mass distributions, star-disc encounters can remove material from the disc. Fig. 3.5 shows the relative disc-mass loss $\Delta m_{\text{rel}} = (m_{t=0} - m_{t_{\text{end}}})/m_{t=0}$ for the four initial disc-mass distribution indices $p = 0$, $p = 1/2$, $p = 1$, and $p = 7/4$. Two representative cases of orbital parameters are singled out: Fig. 3.5*a* shows the dependence on the periastron distance for an equal-mass encounter, whereas Fig. 3.5*b* depicts the dependence on the mass ratio for grazing encounters ($r_{\text{peri}}/r_{\text{disc}} = 1$).

Qualitatively, the dependence of the relative disc-mass loss on the periastron distance agrees with previous results (Pfalzner *et al.*, 2005b; Olczak *et al.*, 2006). However, the absolute values change considerably for the different initial disc-mass distributions. The effect is largest for nearly grazing encounters where mainly the outer disc regions are affected. As expected from the respective fraction of material in the outer regions, maximal mass losses occur for initially constant disc-mass distributions, while minimal losses occur for the $r^{-7/4}$-distribution. The largest difference in mass loss between the investigated disc-mass distributions in Fig. 3.5*a* occurs for $r_{\text{peri}}/r_{\text{disc}} = 0.9$, whereas the $r^{-7/4}$-distribution only has a mass loss of 33 %, and the constant mass distribution has a mass loss of 64 %.

The situation is somewhat different for very close penetrating encounters ($r_{\text{peri}}/r_{\text{disc}} \leq 0.3$), where the discs are so strongly perturbed that the resulting structure can hardly be described as a disc. In this case the disc-mass loss seems relatively independent of the initial mass distribution (see Fig. 3.5*a*). At the other end of the parameter space - i.e. at large relative periastron distances - the mass loss becomes too small ($\Delta m_{\rm rel} \leq 10\%$) to infer any dependence on the initial distribution.

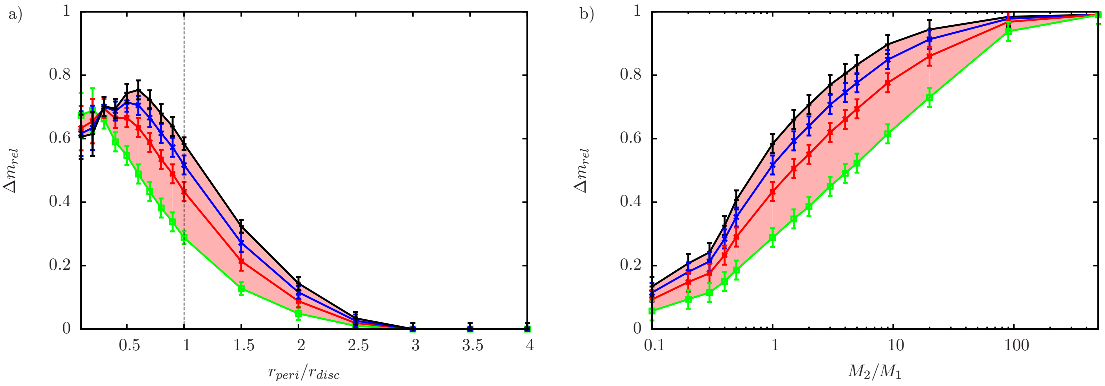

FIGURE 3.5: The relative disc-mass loss of a $p = 0$ (black line), $p = 1/2$ (blue line), $p = 1$ (red line), and $p = 7/4$ (green line) disc-mass distribution including all particles bound more tightly to the central star than to the perturber and excluding unbound and accreted particles. The data is plotted for *a*) different periastron distances and an equal-mass perturber, and *b*) different perturber mass ratios and $r_{\rm peri}/r_{\rm disc} = 1$. The vertical dashed line indicates the initial outer disc radius.

Similarly, the dependence on the initial mass distribution is less pronounced for $M_2/M_1 < 0.3$ and $M_2/M_1 > 90$ (see Fig. 3.5*b* for a grazing encounter). Hence, generally weak perturbations - whether distant or of low mass ratio M_2/M_1 - are incapable of significantly influencing the discs, while in the case of strong perturbations nearly the entire disc material is removed independently of the investigated disc-mass distributions. In both cases, the mass loss does not depend strongly on the disc-mass distribution. In contrast, encounters of intermediate strength are most sensitive to the disc-mass distribution. For the case shown in Fig. 3.5*b*, a maximum differences of up to 35 % for $M_2/M_1 = 3$ is determined.

For high-mass ratios $M_2/M_1 > 20$ and certain non-penetrating periastron distances, which restrict the gravitational star-disc interactions to the outer disc parts, differences in mass loss as high as 40 % can be inferred for the different initial disc-mass distributions.

Having determined the relative disc-mass loss in individual star-disc encounters, Figure 3.6 shows the losses of an initially constant disc-mass distribution divided by the losses of a $p = 7/4$ distribution, as a function of the periastron distance. Three representative mass ratios are presented, $M_1/M_2 = 0.1$, 20, and 500. It can be seen, that the larger the periastron distances the higher are the relative differences between the disc-mass losses for the different initial disc-mass distributions. For perturbations of the outermost disc regions the losses of initially flat disc-mass distributions are around three times higher than the losses for initially steep disc-mass distribution profiles.

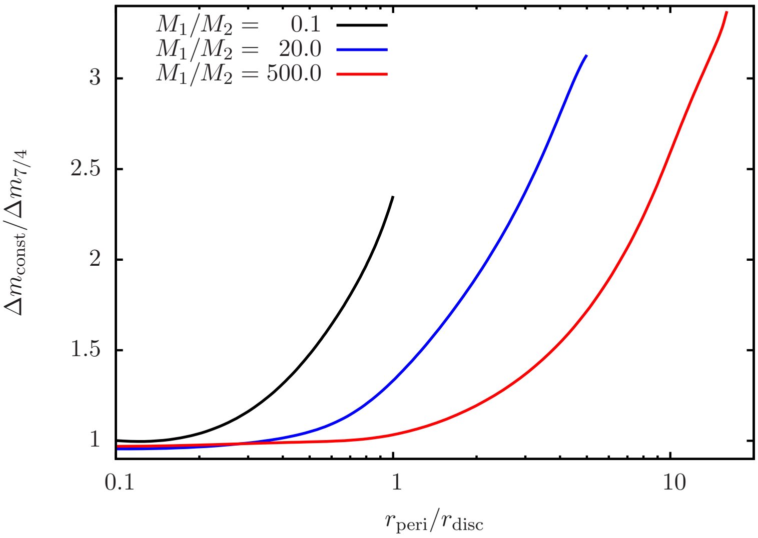

FIGURE 3.6: Shown is the relative disc-mass loss of a constant disc-mass distribution ($\Delta m_{\mathrm{const}}$), in units of the loss of a $r^{-7/4}$ distribution ($\Delta m_{7/4}$), as a function of the periastron distance. The data is plotted for perturber mass ratios of $M_1/M_2 = 0.1$ (black line), 20 (blue line), and 500 (red line). Here, the cases of individual mass losses $\Delta m_{7/4} < 3\%$ have been excluded.

3.2.3 Relative angular momentum loss

The different initial disc-mass distributions do not only influence the disc-mass loss but also the angular momentum loss. Fig. 3.7*a* shows the relative angular momentum loss $\Delta J_{\mathrm{rel}} = (J_{t=0} - J_{t_{end}})/J_{t=0}$ as a function of the encounter distance for equal-mass encounters and the four different disc-mass distributions used in this work. As expected from previous results (e.g. Pfalzner & Olczak, 2007), the general trends in relative angular momentum loss are quite similar to that of the mass loss (compare Figs. 3.5 and 3.7) with angular momentum losses being slightly higher than the disc-mass losses.

While the mass losses for encounters of intermediate strength with $r_{\mathrm{peri}}/r_{\mathrm{disc}} = 0.9$ and $M_2/M_1 = 1$ are 64 % for the constant mass distribution compared to 33 % for the 7/4-mass distribution as shown before, the corresponding angular momentum losses are 75 % and 50 % , respectively. Material migrating inwards or becoming unbound owing to an encounter leads to an angular momentum loss, while the fraction of the disc mass that is pushed beyond the initial disc-radius but remains bound to the central star increases the total angular momentum of the disc. In total, the dependence on the initial disc-mass distributions is less pronounced for the relative angular momentum loss than for the disc-mass loss.

A similar result is found for the relative differences between the angular momentum loss of initially constant ($\Delta J_{\mathrm{const}}$) and $p = 7/4$-density distributed discs ($\Delta J_{7/4}$) shown in

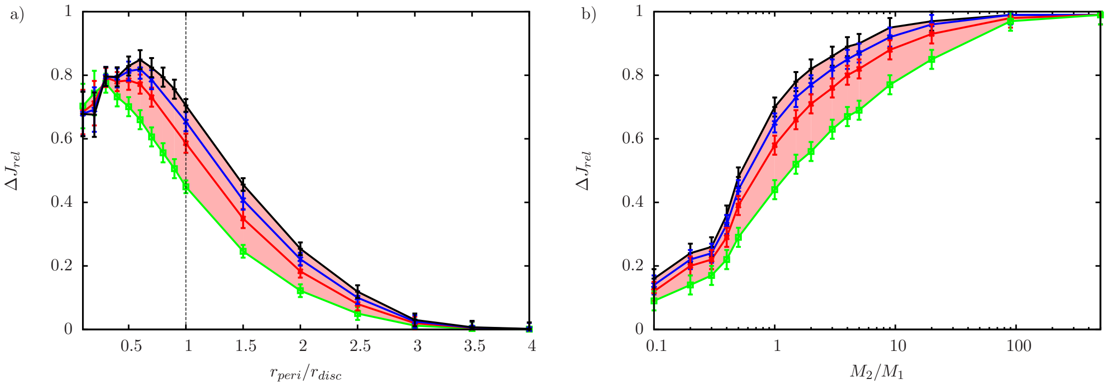

FIGURE 3.7: The relative angular momentum loss of a $p = 0$ (black line), $p = 1/2$ (blue line), $p = 1$ (red line), and $p = 7/4$ (green line) disc-mass distribution including all particles bound more tightly to the central star than to the perturber and excluding unbound and accreted particles. The data is plotted for *a*) different periastron distances and an equal-mass perturber, and *b*) different perturber mass ratios and $r_{\rm peri}/r_{\rm disc} = 1$. The vertical dashed line indicates the initial outer disc radius.

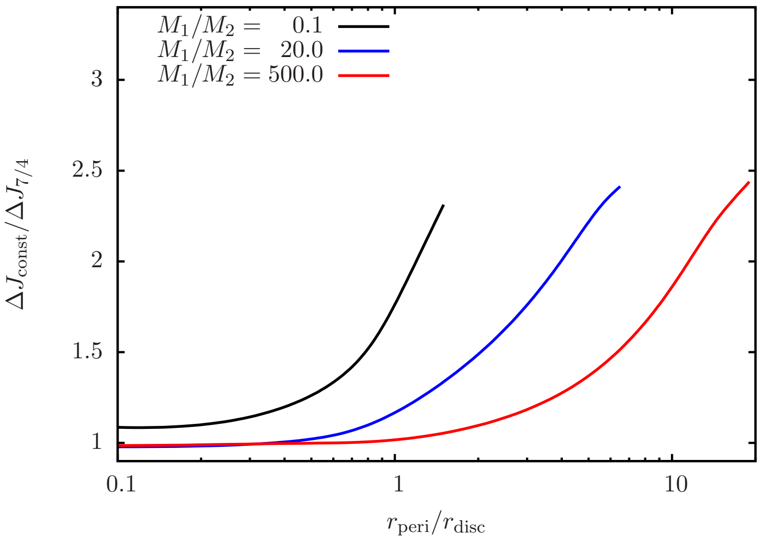

FIGURE 3.8: Shown is the relative angular momentum loss of a constant disc-mass distribution ($\Delta J_{\rm const}$), in units of the loss of a $r^{-7/4}$ distribution ($\Delta J_{7/4}$), as a function of the periastron distance. The data is plotted for perturber mass ratios of $M_1/M_2 = 0.1$ (black line), 20 (blue line), and 500 (red line). Here, the cases of individual angular momentum losses $\Delta J_{7/4} < 3\%$ have been excluded.

Figure 3.8. Here, perturbations of only the outermost disc regions yield to an up to 2.5 times higher angular momentum loss for the initially $p = 0$ distribution than obtained for the case of $p = 7/4$.

However, although the differences are lower in maximum the influence of different initial disc-mass distributions on the angular momentum loss covers a significantly large parameter range.

Since mass and angular momentum losses are generally influenced by perturbations of the outer disc parts, an initially flat particle distribution that has a high resolution in the outer disc regions can help us to achieve a higher accuracy in determining disc losses. Nevertheless, disc losses obtained with initially steep particle distributions ($p = 1$) found in previous studies (Olczak *et al.*, 2006; Pfalzner & Olczak, 2007) are accurately reproduced within the error range in the present study.

3.2.4 Adapting a fit formula dependent on the initial disc-mass distribution

The numerical results for the mass and angular momentum loss in this study cover a wide parameter range but, however, present only a discrete classification of the relative losses for the different initial disc-mass distributions. Analytical approaches are a possible option to avoid this disadvantage but are only valid for a very limited parameter space of distant encounters (Ostriker, 1994; D'Onghia *et al.*, 2010). To obtain a general estimate of the effect of arbitrary initial disc-mass distributions on the encounter-induced mass and angular momentum loss of protoplanetary discs, a fit formula is presented that is valid for *any initial disc-mass distribution*, given that it can be expressed by a power law of the form $\Sigma(r) \propto r^{-p}$. For this purpose, the fit function for the relative mass loss of Olczak *et al.* (2006) (see Eq.4 therein) and for the relative angular momentum loss of Pfalzner & Olczak (2007) (see Eq.1 therein), which are valid for a r^{-1}-distribution, is extended towards arbitrary surface density distribution indices $0 \leq p \leq 7/4$

$$\begin{aligned} \Delta m_{\mathrm{rel}} &= \left(\frac{M_2}{M_2 + 0.5 M_1}\right)^{1.2} \ln\left[(3 - \frac{p}{4}) \cdot (r_p)^{0.1}\right] \qquad (3.3) \\ &\times \exp\left\{-\sqrt{\frac{M_1}{M_2 + 0.5 M_1}}\left[(r_p)^{2-p/2} - 0.5\right]\left(p + |\frac{1-p}{2}|\right)\right\}, \end{aligned}$$

$$\begin{aligned} \Delta J_{\mathrm{rel}} &= 1.02\left[\frac{M_2}{M_1 + M_2} + \left(\frac{1-p}{5} - \frac{\exp(p)}{100}\right)\right]^{0.5 \cdot r_p} \\ &\times \exp\left(-\sqrt{\frac{M_1 (r_p - 0.7\, r_p^{0.5})^3}{M_2}}\right), \qquad (3.4) \end{aligned}$$

where $r_p = r_{peri}/r_{disc}$ is the relative periastron distance.

For most of the parameter space, the adopted functions fit the data well within the margin of error and extend Ostriker's analytical function for the angular momentum loss considerably. Larger deviations of the fit functions from the simulated losses occur only for high encounter mass ratios of $M_2/M_1 > 20$, which was also the case for the established fit functions of Pfalzner & Olczak (2007) and Olczak *et al.* (2006). In the case of disc-penetrating orbits and low-mass ratios, the disc losses can be affected by Lindblad and Corotation resonances that are located in the inner disc regions and cause moderate deviations of the fit function from the expected disc losses.

The extended fit functions provide a significant improvement to previous analytical and numerical results. They cover an extensive parameter space of the most reasonable initial disc-mass distributions and the most relevant orbital parameter ranges expected for interactions in star clusters of any age.

3.2.5 Definition of disc-perturbing encounter

In the following chapter, the previously described results for single star-disc encounters will be combined with simulations of the dynamical evolution of stellar populations. The aim will be an extensive investigation of the influence of the initial disc-mass distribution on star-disc encounters in the different developmental stages of a dynamical cluster environment. In this context, a definition for a disc-perturbing encounter is needed.

The analytical identification of a stellar encounter event has already been introduced in Section 2.2.1. However, not all of such encounters have necessarily a fundamental influence on the circumstellar discs. To investigate the importance of star-disc encounters in cluster environments a criterion is required, which classifies a disc-perturbing encounter.

Due to a limited resolution of current telescopes, observations are generally constrained to the extreme cases of the complete destruction of a disc. A typical observed quantity in this context is the cluster disc fraction that has been discussed extensively in Section 1.3. Throughout this study, a star is termed as *disc-less* and a disc as *destroyed* if $\leq 10\%$ of its initial disc mass remains bound to the central star.

However, already non-destructive encounters significantly influence the structure of circumstellar discs. Encounter-induced density fluctuations might even accelerate the planet formation process via gravitational instabilities within the discs. The relevant physical quantity here to determine the effect of a stellar fly-by on the disc structure is the angular momentum loss. In Figure 3.9 three perturbed discs are shown for differing encounter parameters but similar angular momentum losses of $\Delta J_{\text{rel}} \approx 5\%$. In all these cases the complete disc mass remains bound to the central star. It can be seen that a similar disc structure is obtained for several encounter mass ratios and periastron distances. A signifi-

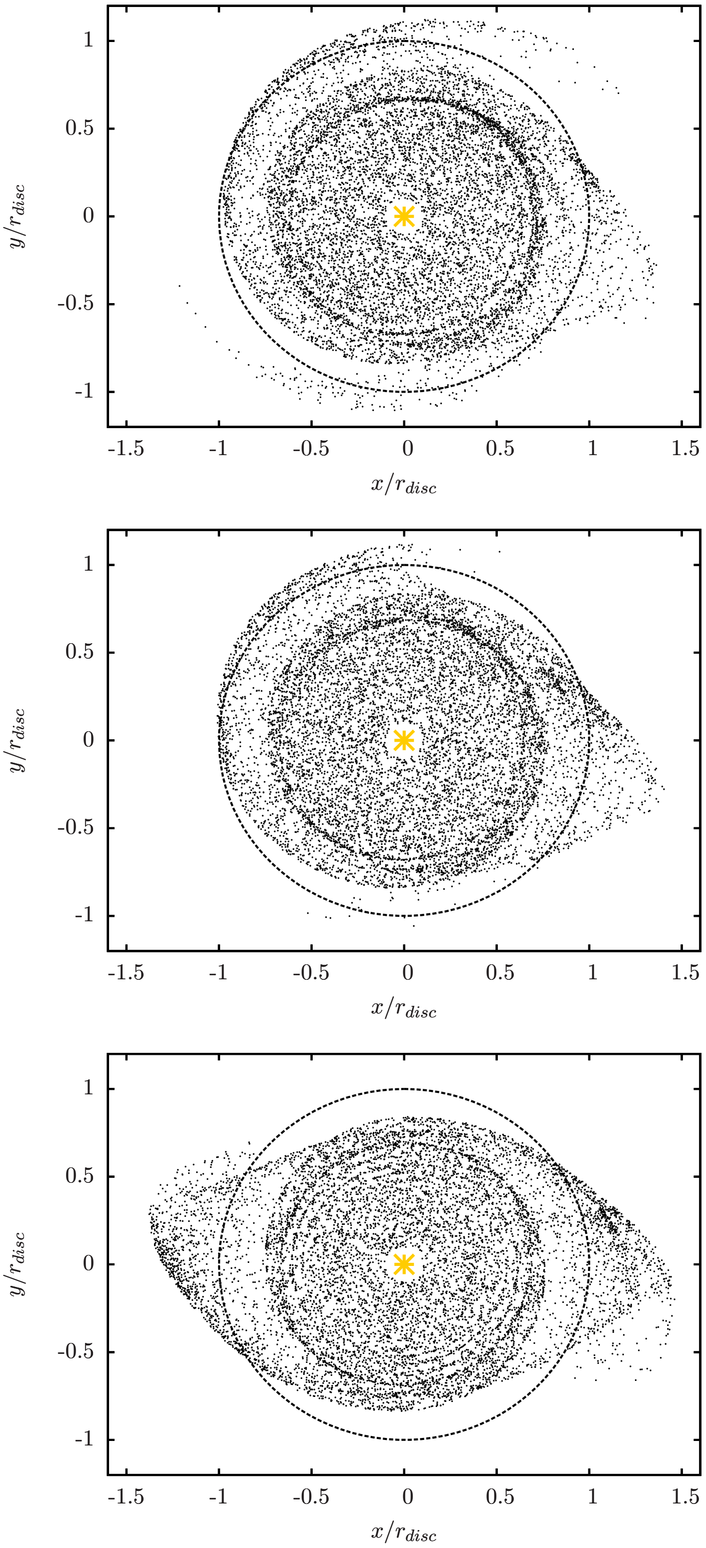

Figure 3.9: Here, three examples of a perturbed star-disc system with an angular momentum loss of ≈ 5% are shown for a) an encounter of mass ratio $M_2/M_1 = 0.5$ and periastron $r_{\mathrm{peri}}/r_{\mathrm{disc}} = 2.5$, b) $M_2/M_1 = 1$ and $r_{\mathrm{peri}}/r_{\mathrm{disc}} = 3.0$, and c) $M_2/M_1 = 90.0$ and $r_{\mathrm{peri}}/r_{\mathrm{disc}} = 11.5$. The dashed line shows the boundaries of the initial disc and the yellow asterisk illustrates the position of the central star.

cant perturbation of the disc outskirts can be determined, accompanied by the formation of two tidal tails, which are a result of the gravitational attraction of the perturbing star and the relative movement between the central star and the center of mass of the disc (Pfalzner, 2003). Only a few observations of such spiral structures exist (e.g. Lin *et al.*, 2006; Muto *et al.*, 2012), not only because of the limited observational resolution, but also due to re-circularisation processes, which might lead to a smoothing of the density fluctuations within a few 10^4 Myr.

To investigate the overall effect of stellar encounters on circumstellar discs in a stellar environment, in the following the disc around a star is defined as *perturbed* if $\Delta J_{\mathrm{rel}} \geq 5\%$. In general, the number of stars with *perturbed* discs is higher than the number of stars with disc-mass loss $\Delta m_{\mathrm{rel}} \geq 3\%$. An encounter leading to a perturbed disc is called a disc-perturbing encounter.

3.3 Conclusion

The circumstellar disc profiles largely determine the shape of the forming planetary systems. Recently, Chiang & Laughlin (2012) analysed the distribution of extrasolar planets found by the Kepler mission and suggested a Minimum Mass Extrasolar Nebula with a power-law index $p = 1.6$, which is even slightly steeper than the one for the Minimum Mass Solar Nebula of $p = 1.5$ (Weidenschilling, 1977). The probably most realistic model for the formation of the Solar System is the *Nice* model (Gomes *et al.*, 2005; Tsiganis *et al.*, 2005; Morbidelli *et al.*, 2005), which describes a dynamical evolution scenario for the formation of the Solar System. Desch (2007) deduced that according to the *Nice* model the initial surface density profile of the solar nebula protoplanetary disc must have been even steeper with a $\Sigma(r) \propto r^{-2.2}$ form to develop into the present Solar System. As a possible way of forming such steep disc-mass density profile, he considered photoevaporation by an external massive star (see also Mitchell & Stewart, 2010). Kuchner (2004) found that similar surface density profiles are required for the formation of known extrasolar planetary systems. In general, these results suggest rather steep disc-mass distribution profiles for the potential formation of planetary systems.

Here, it has been demonstrated that the consequence of an encounter is a steepening in the surface density of the disc on short timescales with close encounters invoking density profiles steeper than $\Sigma(r) \propto r^{-2}$ for any given initial disc-mass distribution. Since these density profiles are probably the prerequisite for forming a planetary system similar to the Solar System, encounters in the early history of the Solar System might have provided these conditions (Adams, 2010).

Moreover, the results emphasise that these steep density profiles do not have to exist ab initio or be formed by photoevaporation processes but that even discs that initially have evenly distributed material can fulfil the requirements for the formation of a Solar System type planetary system in the inner disc regions after a close encounter. Additional evidence of such an encounter in the case of the early Solar System was given by distant Solar System objects on highly eccentric orbits, such as the transneptunian object Sedna, and also the sharp outer edge of the Solar System at $\sim 50\,\mathrm{AU}$ from the Sun (Ida *et al.*, 1999; Allen *et al.*, 2001; Morbidelli & Levison, 2004; Kenyon & Bromley, 2004). Pfalzner (2012) showed that the Solar System most likely formed in a leaky cluster environment with an encounter probability of $\approx 30\%$ in the first 2 Myrs.

On the other extreme, in rare cases encounters can not only lead to profile steepening but also to profile flattening, which might explain even the surface density distribution profiles of $p < 0$ observed by Isella *et al.* (2009).

Consequently, if all young stars were to start out with the same disc-density structure, the influence of the cluster environment by means of encounters in the very early and dense phases of cluster evolution could account for the observed multitude of today's disc-mass density profiles.

3.4 Summary

As most stars probably form in clustered environments encounters are likely to have a significant impact on the disc structure. The scope of this part of the study was to determine the role of the initial mass distribution in this context. The parameter study of star-disc encounters performed in my diploma thesis was extended for disc-mass distributions of the form $\Sigma(r) \propto r^{-p}$ with $p \in [0, 1/2, 1, 7/4]$. The results can be summarised as follows:

1. The relative disc-mass loss differs by up to 40 % among the different initial density distributions for the same type of encounter. The largest differences are associated with perturbations of the outer disc edge, where the mass loss can be up to three times higher for flat disc-mass distributions ($p = 0$) compared to steep distributions ($p = 7/4$).

2. The dependence on the initial disc-mass distribution is less pronounced for the relative angular momentum loss in such encounters. Here, differences of 15% between the investigated distributions are typical.

3. The general effect of an encounter is a steepening of the surface density slope for any initial disc-mass distribution, which can result in distribution indices of $p > 2$ even in the case of initially flat distributions.

4. The disc-mass and angular momentum losses caused by a parabolic encounter can be fitted by a function of the perturber mass ratio, the relative periastron distance, and the index of the initial disc-mass distribution.

In short, the intuitive result that the flatter the mass distribution the stronger the change in the disc mass and angular momentum caused by encounters has been quantified. This infers that the importance of encounters in young stellar clusters and their potential to trigger encounter-induced losses might be reconsidered depending on the dominant initial disc-mass distribution.

4 Embedded clusters in virial equilibrium

The vast majority of stars seems to be born in massive stellar clusters (Lada & Lada, 2003; Porras *et al.*, 2003; Evans *et al.*, 2009). In the first few Myr of their lifetime the stars are surrounded by their natal gas, however, the time scale of this embedded period is observationally not well-constrained, but is expected to be lower than 5 Myr in case of the most massive clusters (see Section 1.5).

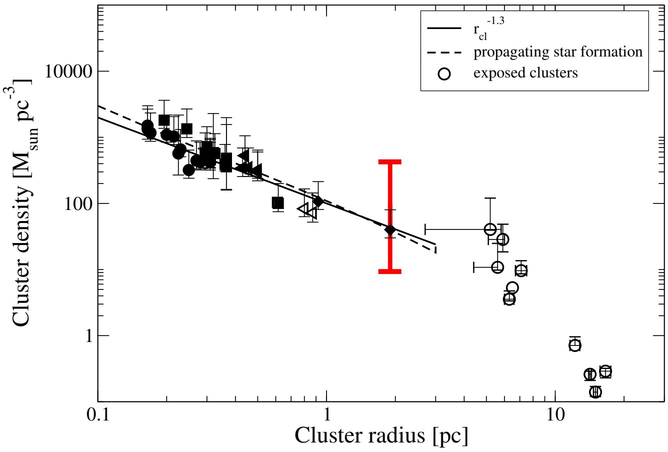

FIGURE 4.1: Same as Fig. 1.8 but here the simulated density space is indicated by a red bar.

The scope of this section is to investigate this early embedded phase of stellar cluster development and the general influence on the disc frequencies. One example of such an embedded cluster, where the gas expulsion process near the massive OB-stars recently started, is the Orion Nebula Cluster (ONC), which has been extensively described in Section 1.4. Here, it is used as a model cluster since it is one of the best observed young massive star forming regions that is, at least partly, still embedded in its natal gas. As detailed in Section 1.4, previous numerical investigations found high probabilities for encounters between the stellar members during the temporal development of such dense stellar cluster environments. Olczak *et al.* (2010) found that the encounter rate is rather unaffected by the cluster size but depends strongly on the stellar density. They found that the ONC itself marks

	variable	value
number of star	N_{stars}	4 000
mean stellar mass	m_{mean}	0.5
core radius	r_{core}	0.3 pc
cluster size	r_{cluster}	2.5 pc
half-mass radius	r_{hm}	≈ 1 pc
cluster core density	ρ_{core}	$2 \cdot 10^4\,\text{pc}^{-3}$
mean age	t_{age}	1 Myr
crossing time	$t_{\text{cross,hm}}$	0.5 Myr

TABLE 4.1: Properties of the Orion Nebula Cluster (Hillenbrand & Hartmann, 1998, and references therein).

a threshold; in less dense clusters the high-mass stars dominate the interaction dynamics, whereas in denser clusters the interactions between the low-mass stars themselves play the major role for the disc-mass loss.

Here, six representative cases of 0.25, 0.5, 1, 2, 4, and 8 times the density of the ONC have been investigated. The entire range of initial cluster densities covered in this chapter is indicated in Figure 4.1 by a red bar. In addition the observed densities of young embedded clusters are shown as a function of the cluster size (for more details about the evolution of the clusters along the sequence shown in black see Section 1.5). The here covered density range is representative for *massive* clusters in the late embedded stage. Clusters of lower densities than considered here might exist as well, but are less prone to gravitational interactions (Olczak *et al.*, 2010) and, moreover, observationally not well constrained (Carpenter *et al.*, 2000).

4.1 Setup

The general setup of the stellar masses, radial positions, and velocities has been extensively described in Section 2.3. However, in this chapter we concentrate on ONC-like cluster models, which involves some assumptions about the setup that are discussed in the following. The general properties of the ONC are summarized in Table 4.1.

As mentioned in Section 1.4.3, no evident primordial mass segregation scenario could be confirmed as correct so far. However, Olczak *et al.* (2011) determined from data of today's ONC (Hillenbrand, 1997) a segregation of the five most massive stars towards the cluster center, while the remaining stars show no signs of mass segregation. Following the approach by Bonnell & Davies (1998), here, initially the four most massive stars have been distributed in the inner cluster region with $r_{\text{seg}} = 0.6 \cdot r_{\text{hm}}$.

The stars have been distributed according to Equation 2.37, which describes a nearly isothermal density profile with a slightly enhanced number density in the core region. To model the stellar velocities, a Maxwellian velocity distribution (as described in Section 2.3) with radius-independent velocity dispersion σ has been used. This choice is supported by observations, as Jones & Walker (1988) found a nearly constant velocity dispersion of $\sigma_{\mathrm{1dim}} \approx 2$km/s independent of the cluster radius by studying stellar proper motions in the ONC. This corresponds to a three-dimensional velocity dispersion of $\sigma = \sqrt{3} \cdot \sigma_{\mathrm{1dim}} \geq$ 3.46km/s. Recent observations, investigating radial velocities in the ONC found even higher values of $\sigma_{\mathrm{1dim}} \approx 3$km/s (Fűrész *et al.*, 2008).

As the mean stellar mass $m_{\mathrm{mean}} \approx 0.5$ (Tab. 4.1), this results in a total cluster mass $M_{\mathrm{ONC}} = N \cdot m_{\mathrm{mean}} = 4\,000 \cdot 0.5\ \mathrm{M}_{\odot} = 2\,000\ \mathrm{M}_{\odot}$. Assuming above velocity dispersions, the virial ratio Q is then given by

$$Q = \frac{r_{\mathrm{hm}}\sigma^2}{2GM_{\mathrm{ONC}}} \geq 0.7, \tag{4.1}$$

with the half-mass radius of the ONC given by $r_{\mathrm{hm}} \approx 1\,\mathrm{pc}$. From Eq. 4.1 it follows that the ONC is expected to be in a super-virial state, probably due to recent gas expulsion processes in the core region. However, observational uncertainties in the parameter determination (Scally *et al.*, 2005) - and the neglect of low-mass objects (like brown dwarfs) and the gas component - presumably lead to a considerably underestimation of the total mass M_{ONC}, which might lead to an overvalued virial ratios. Since in this chapter we are in particular interested in the effect of stellar encounters rather than the cluster evolution the focus here will be on initially virialised systems of $Q = 0.5$. Super-virial clusters will be investigated in Section 5.

For simulations presented in this chapter, no background potential describing the gas component is included since the focus is on dynamical snapshots of the stellar cluster before the gas is expelled. In this case the clusters remain in a roughly virial state. Moreover, after 1 Myr the stellar density profiles match observed embedded clusters (Section 2.3), which justifies the usage of the present approach for investigations of the relevance of stellar encounters in young clusters.

The stellar velocities are chosen in such a way as to match an isothermal stellar density profile in virial equilibrium. The higher mass concentration in the core region (Eq. 2.37) implies, that in our model the velocities are slightly underestimated which has only a marginal effect here since the clusters rapidly expand due to the rather short crossing times.

Model	N_{stars}	N_{sim}	$\rho_{\text{core}}[10^3\,\text{pc}^{-3}]$	$\rho_{\text{cluster}}[\,\text{pc}^{-3}]$
A	1 000	500	1.3	15.3
B	2 000	250	2.7	30.6
C	4 000	125	5.3	61.1
D	8 000	70	10.5	122.2
E	16 000	32	21.1	244.5
F	32 000	16	42.0	489.2

Table 4.2: The number of initial stars N_{stars}, number of performed simulations N_{sim}, number density of the cluster core region ρ_{core} and total cluster density ρ_{cluster} for the six investigated models are shown. The radius of the core region is $r_{\text{core}} = 0.3\,\text{pc}$ while the cluster size is $r_{\text{cluster}} = 2.5\,\text{pc}$. The core density is given by $\rho_{\text{core}} = 3N_{\text{core}}/4\pi r^3_{\text{core}}$ and the cluster density by $\rho_{\text{core}} = 3N_{\text{stars}}/4\pi r^3_{\text{cluster}}$.

4.1.1 Density scaling

The relative importance of encounters is likely a strong function of the cluster density. Apart from the ONC-model, density-scaled versions of this model will be investigated to show the dependence of the results on the cluster density (see also Olczak *et al.*, 2010). As mentioned before, a suitable range of cluster densities has been modeled that covers the densities of typical embedded massive clusters (Fig. 4.1).

The density scaling of the star clusters was achieved by keeping the size of the cluster constant ($r_{\text{cluster}} = 2.5\,\text{pc}$) and varying the initial number of stars N_{stars}. Assuming a stellar number density of roughly $\rho(r) = \rho_0 r^{-2}$ we obtain

$$N_{\text{stars}} = \int_0^{r_{\text{cluster}}} \rho(r) r^2 \mathrm{d}r \mathrm{d}\Omega \propto \rho_0 r_{\text{cluster}} \tag{4.2}$$

which shows that in the present case the cluster density scales with the number of stellar members. As mentioned in Section 2.3 a slightly steeper profile of $\rho_{\text{core}}(r) \propto r^{-2.3}$ has been used for the cluster core, however, it has only a minor effect due to the low stellar number in that region. Here, models with 1 000, 2 000, 4 000, 8 000, 16 000 and 32 000 stars were investigated, corresponding to cluster densities of 0.25, 0.5, 1, 2, 4 to 8 times the initial stellar density of the ONC-like models at any radius $r < r_{\text{cluster}}$.

Although the cluster is initially in virial equilibrium, the population is expected to expand with time due to individual stellar escapers, most likely from the outer cluster regions. The fraction of escapers is expected to be similar for the density-scaled models, given that the number of escapers, ΔN_{esc}, from each shell of width Δr at radius r from the cluster center scales with the total number of stars in that shell ΔN_{stars}. From Eq. 4.3 one obtains

$$\Delta N_{\text{esc}}(r) \propto \Delta N_{\text{stars}}(r) \propto \rho_0 \Delta r \propto N_{\text{stars}} \Delta r, \tag{4.3}$$

so that the fraction of escapers remains constant $\Delta N_{\mathrm{esc}}(r)/N_{\mathrm{stars}}$ for the density-scaled models. Thus, it is expected, that the temporal evolution of the density profiles will be roughly the same.

An overview of the parameters of the simulated models, like initial number of stars N_{stars} and corresponding number of simulations N_{sim}, is shown in Table 4.2, as well as the resulting densities in the cluster core region ρ_{core} (with $r_{\mathrm{core}} = 0.3\,\mathrm{pc}$, the total radius of the Trapezium cluster) and the mean cluster density ρ_{cluster} within the cluster radius $r_{\mathrm{cluster}} = 2.5\,\mathrm{pc}$.

4.2 General cluster dynamics

The parameters that largely determine the dynamical evolution of a stellar cluster are the virial ratio and the cluster density distribution. In this part of the study, the clusters have been set up in virial equilibrium, $Q = 0.5$, which means they are initially neither expanding nor contracting.

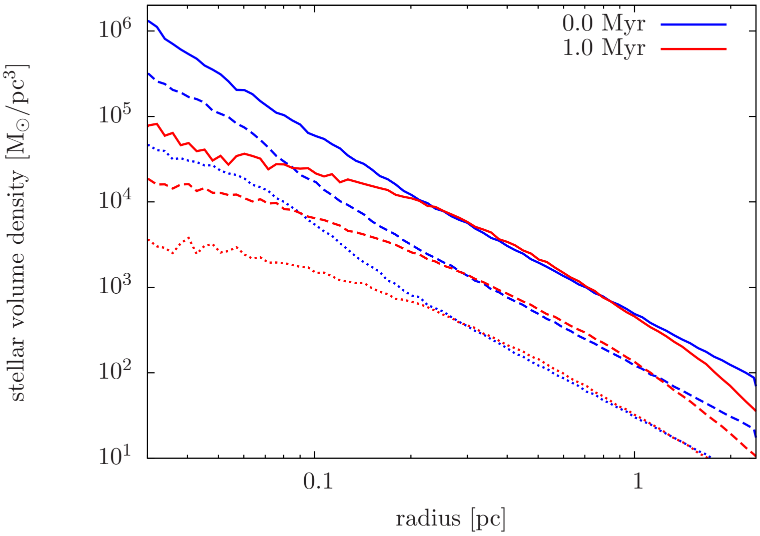

FIGURE 4.2: Shown is the stellar mass volume density as a function of the distance to the cluster center for the initial distribution (blue) and after 1 Myr (red). The results are plotted for model *A* (dotted line), model *C* (dashed line), and model *E* (solid line).

In Figure 4.2 the evolution of the stellar mass volume density distribution is shown as a function of the distance to the cluster center. Three representative models are show, model *A* (dotted line), model *C* (dashed line), and model *E* (solid line). It can be seen that the initial distributions, shown in blue, are equidistant distributed in accordance with differences in the initial densities of a factor of four. As expected the density is uniformly increased for a higher number of stars independent of the radial distance to the center. Due to the primordial mass-segregated setup of the clusters, which involves a subsequent positioning of the four most massive stars in the cluster center, the densities are here slightly increased. This effect is most prominent for the sparse clusters where only a minor fraction of stars is located in the inner regions. However, the evolution of the profiles is not influenced by this difference as can be deduced from the similarly shaped distributions after 1 Myr, shown in red. As expected from the analytical predictions in Section 4.1.1, for all shown cluster models a drop of the inner density can be deduced due to an expansion of the cluster induced by the stellar escapers.

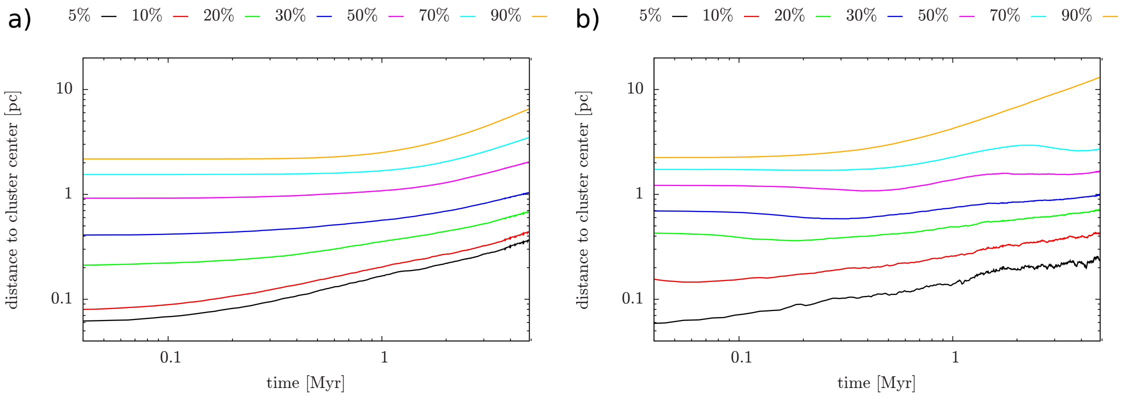

FIGURE 4.3: Shown are the Lagrangian radii as a function of the simulation time for (a) model A and (b) model E. The Lagrangian radii are presented for enclosed mass fractions of 5%, 10%, 20%, 30%, 50%, 70%, and 90%.

The evolution of the stellar volume density over time is demonstrated in Figure 4.3 for sparse (model A shown in Fig. 4.3a) and dense (model E shown in Fig. 4.3b) clusters. Here, the Lagrangian radii, representing volumes that include a constant fraction of stellar mass, are plotted as a function of the simulation time. For model A after 0.1 Myr an expansion of the core can be seen by an increase of the 5% Lagrangian radius. The relatively short time scales for the expansion of the innermost cluster regions are in accordance with a decrease of the crossing time with radius (Eq. 1.7). With time the density wave propagates outwards and the cluster expands until a new virial equilibrium state is reached.

For model E, shown in Figure 4.3b, which contains a much higher number of stars within the same volume, the crossing time of the system is significantly reduced which leads to a much faster expansion of the core region. Moreover, after 3 Myr a deceleration of the process indicated by a flattening of the 70% Lagrangian radius can be seen. This indicates a dynamical *cooling* of the inner system, while the outermost mass fraction, indicated by the orange line, are probably escapers.

4.3 Encounter dynamics

In the following the cluster dynamics are investigated with focus on stellar encounters. In this chapter, the exclusive case of initially constant disc-mass distributions will be studied, since the qualitative results for the dynamical evolution are unaffected by the initial disc-mass distribution.

Figure 4.4 shows the number of stars as a function of their radial position after 1 Myr and a green reference line indicating the initial distribution. The maximum standard deviation is 2% and all data bins with on average less than one star have not been considered in Figure 4.4. The evolved stellar positions are divided in two groups, stars which retain part of their discs (red circles) and disc-less stars (blue squares), which lost more than 90% of their discs mass due to gravitational interactions (see Sec. 3.2.5). In general, after 1 Myr the number of stars in the core region, $r_{\text{core}} = 0.3\,\text{pc}$, is significantly reduced as a substantial number of stars is ejected to large distances. Stars that maintain their discs are mostly located in the outer cluster regions, but within 10 pc[*]. Even though these stars might have been part of an encounter, this event was apparently not strong enough to remove their discs.

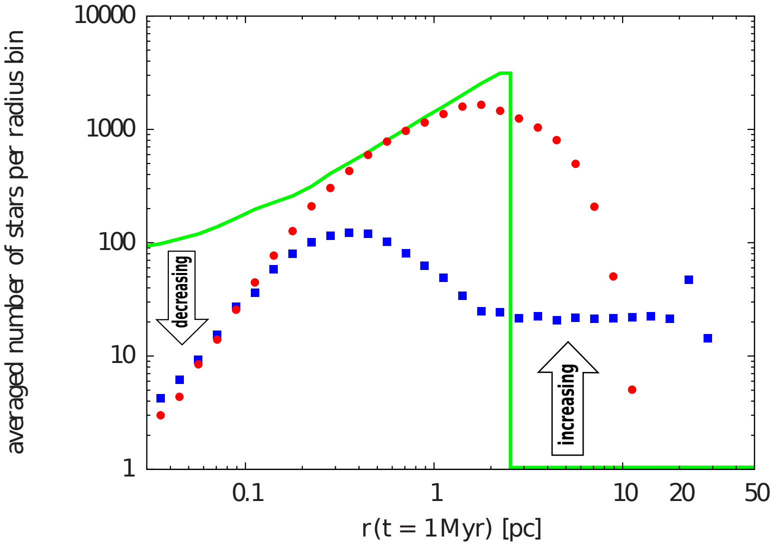

FIGURE 4.4: Shown is the averaged number of stars per radius bin versus the distance to the cluster center after 1 Myr for model *E*. Red circles indicate stars which maintain > 10% of their initial disc-mass, while blue squares represent stars that lost their disc due to gravitational interactions. The initial stellar distribution is indicated by a green solid line. The standard deviation is ≤ 2%.

---

[*] On average less than one star per radial bin, initially located in the inner 0.3 pc of the cluster, is ejected to more than 10 pc without loosing its disc. These stars belong to the minor fraction of escaping stars that are located in the high-velocity tail of the Maxwellian distribution.

By contrast, the disc-less stars are prominent in the innermost and the outermost parts of the population. Inside 0.2 pc even higher numbers of disc-less stars are found than stars surrounded by discs. Moreover, basically all stars located outside of 10 pc lost their discs in encounters. In the outermost parts at around 20 pc a pronounced peak indicates a significant amount of ejected stars with velocities $> 20\,\mathrm{pc/Myr}$. This traces a strong encounter event within the first few 10^5 years, which destroyed the discs of these stars and accelerated them strongly towards the cluster outskirts.

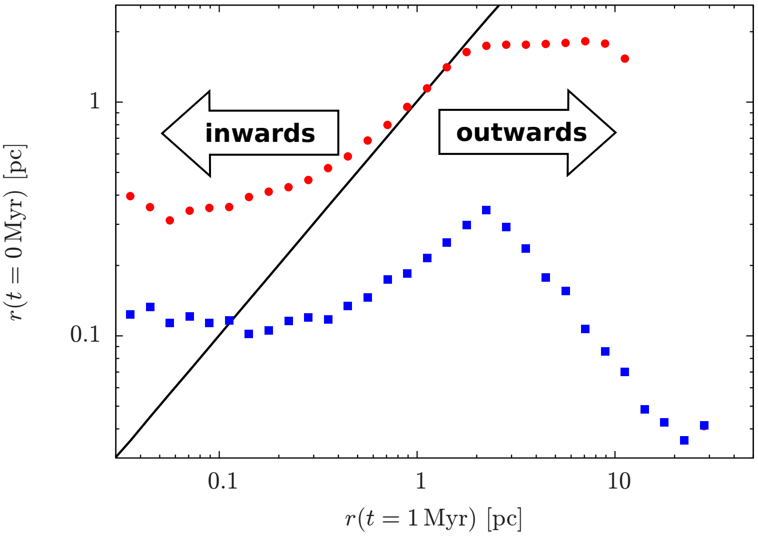

FIGURE 4.5: Shown is the averaged initial radius versus the actual distance to the cluster center for model *E*. Red circles indicate stars which maintain $> 10\%$ of their initial disc-mass after 1 Myr evolution, while blue squares represent stars that lost their disc due to gravitational interactions. The initial stellar distribution is indicated by a black solid reference line. Radial bins with an average of less than one star have not been considered.

Figure 4.5 shows the initial distance of the stars to the cluster center as a function of the distance to the cluster center after 1 Myr. Again blue squares represents the stars that lose their disc and the red circles stars that remain surrounded by a disc. The solid black reference line divides an inward from an outward movement. It can be seen that, as expected, after 1 Myr most of the stars have moved far from their initial positions accompanied by an increase in the cluster size.

The majority of stars that remain surrounded by a disc are initially located outside of the inner 0.3 pc. By contrast, the stars which already lost their discs due to gravitational interactions are initially located within the inner 0.3 pc, indicating that strong perturbations of the discs preferentially occur in the core region of the cluster.

Stars that are initially located within the 0.1 pc from the cluster center most likely lose their discs early on and are rapidly ejected. These disc-less fraction of the innermost stars gains sufficient kinetic energy to be expelled to distances far beyond 10 pc within 1 Myr. The peak of the distribution of the disc-less stars around 2.5 pc marks the temporal threshold where the ejection process decreases and the remnant cluster population starts to equilibriate.

4.4 Effect of the initial disc-mass distribution

Investigating the effect of the initial disc-mass distribution in star-disc encounters, we follow the approach by Olczak *et al.* (2010), which only investigated initial distributions $\propto r^{-1}$. They found a strong influence of gravitational interactions on the circumstellar discs in the central regions for clusters of intermediate stellar density and even sparse clusters due to gravitational focusing around the massive stars. For dense clusters encounters are even more important. However, here encounters between low-mass stars are the major disc destruction process.

In this section, the focus will be on the upper limits for the disc losses, which is achieved by assuming all encounters being coplanar and parabolic. Moreover, the focus here will be on the cluster core regions ($r_{\mathrm{core}} = 0.3\,\mathrm{pc}$), representing the densest part of the stellar population. Initially all stars are surrounded by a disc which are assumed to be equally distributed with $r_{\mathrm{disc}} = 150\,\mathrm{AU}$, representing an average value of observed disc sizes. If not mentioned otherwise, in the following above characteristics are used to obtain general upper limits for the disc losses. Afterwards, the limits will be extensively discussed.

4.4.1 Dependence on stellar density

Figure 4.6 shows the fraction of destroyed discs, $F_{\mathrm{destroyed}}$, after 2 Myr of cluster evolution as a function of the central cluster densities in the regime 1.3×10^3 and $4.2 \times 10^4\,\mathrm{pc}^{-3}$ (represented by Model A - F). It can be seen that for initial disc-mass distributions of r^{-1} (filled blue circles) central cluster densities of $10^3\,\mathrm{pc}^{-3}$ lead to around 15% of all circumstellar discs being destroyed. For volume densities above $10^4\,\mathrm{pc}^{-3}$ the fraction of destroyed discs increases considerably to around 50% [†]. Here, the fraction of destroyed discs has been fitted by a second order polynomial function, given by

$$F_{\mathrm{destroyed}}(\rho) = 71\rho^2 + 5.9\rho + 0.135, \tag{4.4}$$

[†] The fraction of destroyed discs is slightly lower than in Olczak *et al.* (2010). The reason is that they used a fit formula for the disc-mass losses that slightly overestimates the losses in case of mass ratios $M_2/M_1 > 20$. Here, an interpolation algorithm based on an extended parameter study is used as described in Section 2.2.

where the number density ρ has been scaled with $\rho = \rho_{\text{core}} \cdot 10^{-6}\,\text{pc}^3$. $F_{\text{destroyed}}(\rho)$ is indicated by the solid blue line in Figure 4.6. Note, that the fit function is restricted to core densities in a range of 10^3 to $4 \times 10^4\,\text{pc}^{-3}$, which, however, covers the complete range expected for the massive stellar clusters in the solar neighbourhood.

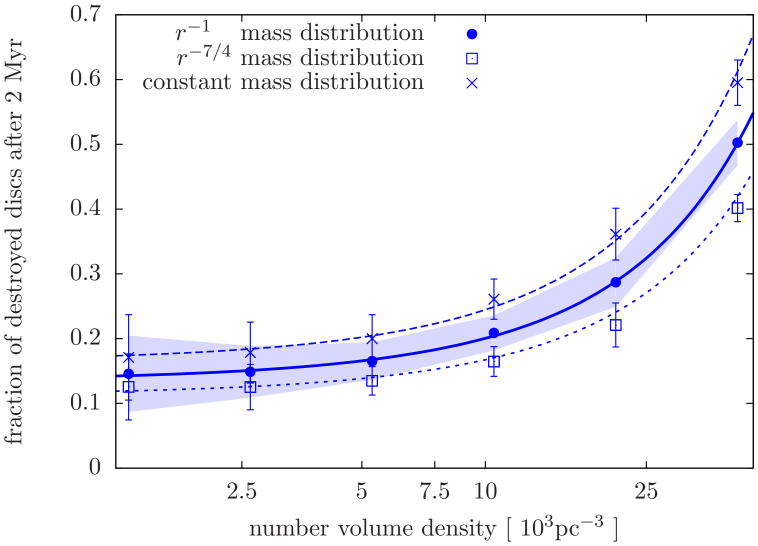

FIGURE 4.6: The fraction of destroyed discs after 2 Myr of evolution is plotted against the stellar number volume density in the core region ($r_{\text{core}} = 0.3\,\text{pc}$). Circles represent the results of an initial r^{-1} disc-mass distribution, while crosses show the constant and open squares the $r^{-7/4}$ distributions. The filled curve indicates the standard deviation for $p = 1$. The fits according to Eq. 4.5 are indicated by the blue solid ($p = 1$), dashed ($p = 0$), and dotted ($p = 7/4$) line.

Using an initial disc-mass distribution that differs from the r^{-1} case, one observes a density-dependent deviation of the cluster disc fraction. For low central densities, $\rho_{\text{core}} \leq 5 \times 10^3\,\text{pc}^{-3}$, the disc fraction for the different initial distributions are found to differ only slightly from the r^{-1} distribution. Here, again $\approx 15\%$ of the discs are destroyed in less than 2 Myr. For dense clusters larger differences in the fraction of destroyed discs are found. In the case of $4 \times 10^4\,\text{pc}^{-3}$ (Model F), for an initially constant disc-mass distribution the majority of circumstellar discs (60%) are destroyed by encounters, whereas for the $r^{-7/4}$ distribution the fraction is only about 40%. In other words, 50% more discs are destroyed for an initially constant disc-mass distribution compared to $r^{-7/4}$. As to be expected, here, an initially constant disc-mass distribution provides a maximum for the encounter-induced disc mass losses.

The higher the cluster density the larger is the difference in the cluster disc fraction for the different mass distributions. From relation 4.4 it follows that this difference is as well a function of the disc fraction, given by

$$\frac{F_{\text{destroyed}}(\rho, p)}{F_{\text{destroyed}}(\rho)} = 1.22 - 0.22p, \tag{4.5}$$

where p is the initial disc-mass distribution index and $F_{\text{destroyed}}(\rho)$ the fraction of disc-less stars in case of an initially r^{-1} distribution (Eq. 4.4), e.g. for densities of $10^4\,\text{pc}^{-3}$ a fraction of $F_{\text{destroyed}}(\rho = 10^4) = 21\%$ of all stars lose their discs, while the fraction is increased to 25% for initially constant disc-mass distributions and decreases to 17.5% for the steepest distributions. In Figure 4.6 the dashed blue line shows the fit function for $p = 0$ while the fit for $p = 7/4$ is indicated by the dotted blue line. The results have also been tested for $p = 1/2$, so that Equation 4.5 can be used in the entire interval of $p \in [0, 7/4]$.

Apart from investigations of the disc destruction rates, which basically focus on strong perturbations of the discs, even weak stellar encounters might influence the disc properties, such as disc mass and the mass distribution within the disc. This processes are of major importance but observationally difficult to constrain. To evaluate the general influence of stellar encounters on the disc properties the focus in the following will be on small variations of the disc's angular momentum, which has been defined as being characteristic for a perturbed disc in Section 3.2.5.

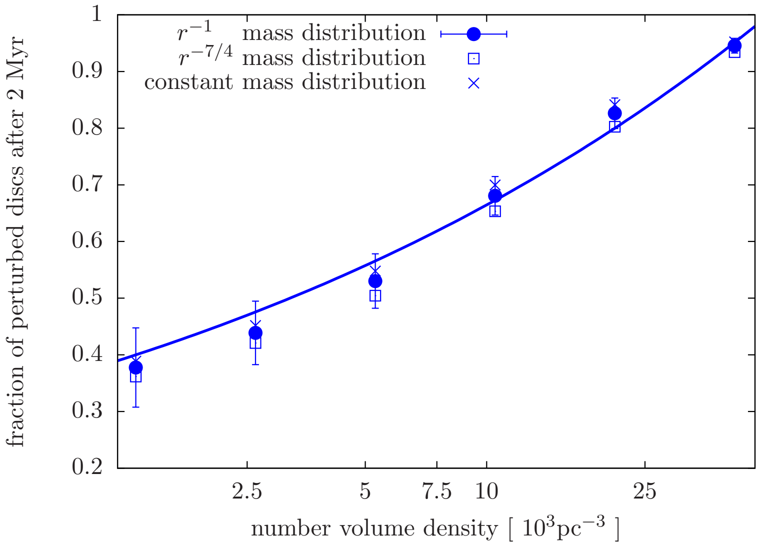

FIGURE 4.7: The fraction of stars with perturbed discs after 2 Myr of evolution is plotted against the stellar cluster density in the core region ($r_{\text{core}} = 0.3\,\text{pc}$). Circles represent the results for an initial r^{-1} disc-mass distribution, while crosses show the constant and open squares the $r^{-7/4}$ distributions. The standard deviation is shown for the r^{-1} distribution and is of the same order for the other distributions.

Figure 4.7 shows the fraction of stars with perturbed discs after 2 Myr as a function of the cluster core density. We find that the fraction increases nearly linearly in logarithmic space from 40% stars with perturbed discs for $\rho_{\text{core}} = 1.3 \times 10^3$ to 95% for central densities of $4.2 \times 10^4\,\mathrm{pc}^{-3}$. In dense clusters almost every star experiences an encounter event within the first 2 Myr in the dense inner cluster regions. The fraction of stars with perturbed discs, $F_{\mathrm{perturbed}}(\rho)$, can be fitted by

$$F_{\mathrm{perturbed}}(\rho) = 0.4 \left(\frac{\rho}{1.3 \cdot 10^3\,\mathrm{pc}^{-3}} \right)^{0.25}, \tag{4.6}$$

where ρ is the density within the core region of 0.3 pc. The fit function is shown in Figure 4.7 as a solid blue line.[‡]

Figure 4.7 shows as well the results for a constant initial disc-mass distribution and a $r^{-7/4}$ distribution. It can be seen that the fraction of stars with perturbed discs is basically not influenced by the initial disc-mass distribution. The reason is that for the vast majority of perturbed discs angular momentum losses $\gg 5\%$ are obtained. Only a minor fraction of discs are only slightly perturbed in the range $< 5\%$. This means that our results are applicable to arbitrary initial disc-mass profiles in the range $[0; 7/4]$. Thus, even steep distributions, which are believed to be the prerequisite profiles for planet formation (Desch, 2007; Meru & Bate, 2011), are significantly influenced by encounters.

Keeping in mind, that for the very dense clusters at least 40% of all circumstellar discs in the core region are destroyed by gravitational interactions leaves $\approx 55\%$ of stars with a significantly altered disc structure in the cluster core region. This fraction of stars possibly forms planets under conditions that differ significantly from the isolated case. In general, the fraction of altered (but undestroyed) discs can be obtained by the difference of Equation 4.6 and Equation 4.5.

Having investigated the extreme cases of a complete destruction of the circumstellar disc ($> 90\%$ disc mass loss) as well as all significant disc perturbations ($> 5\%$ angular momentum loss), the dependence on the loss thresholds is investigated in the following. Figure 4.8 shows the cumulative fraction of stars as a function of the angular momentum loss. For dense clusters (Fig. 4.8a) it can be deduced that the higher the angular momentum losses the larger is the dependence on the initial disc-mass distribution. However, for sparse clusters (Fig. 4.8b) the dependence is less pronounced. The reason is that large differences between the investigated initial disc-mass distributions are apparent for strong perturbations of the outer parts of the circumstellar discs. Such strong perturbations are given by either individual high-mass encounters or multiple low-mass perturbations (see Sec. 3.2.2 and Sec. 3.2.3). This will be quantified in the following.

[‡] Note, that the standard deviation for sparse clusters is found to be up to 10%, while the deviations for dense clusters are only $< 2\%$. The reason is that in sparse clusters disc losses are specified by the few high-mass stars and depend strongly on their position within the cluster. In dense clusters an increasing number of low-mass stars is involved in encounter events reducing the prominent effect of the high-mass stars.

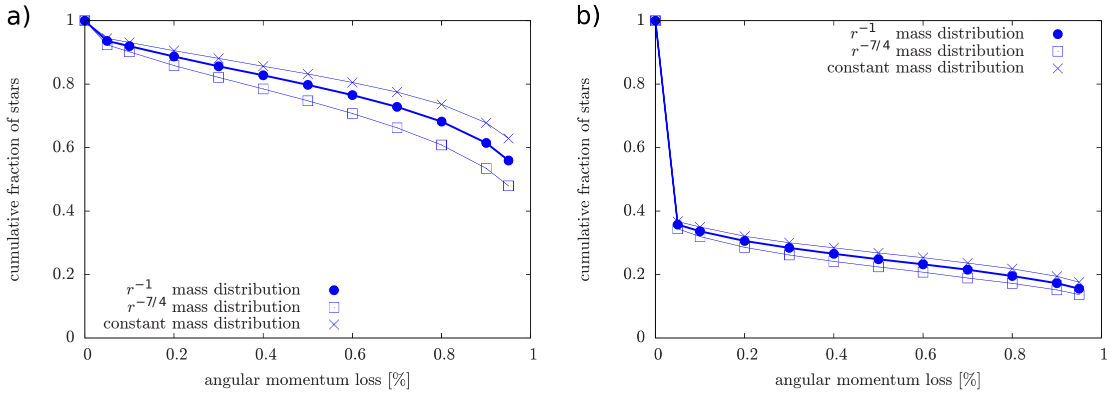

FIGURE 4.8: Shown is the cumulative fraction of stars as a function of the angular momentum loss after 2 Myr. The results are shown for (a) Model F and (b) Model A. Circles represent the results of an initial r^{-1} disc-mass distribution, while crosses show the constant and open squares the $r^{-7/4}$ distributions.

4.4.2 Dependence on stellar mass

Figure 4.9 shows the fraction of disc-less stars as a function of the stellar mass for (a) Model A and (b) Model F. For low stellar density environments a prominent loss of disc material surrounding the massive stars is found (Fig. 4.9a). Here, the high-mass stars in the center act as gravitational focii, causing multiple encounters with the surrounding stars. Due to the high number of encounters the entire discs of stars more massive than $50\,\mathrm{M}_\odot$ are quickly removed while stars with masses $M_1 < 10\,\mathrm{M}_\odot$ mostly retain some portion of their discs. For such low- and intermediate-mass stars only a minor fraction is involved in encounters, which leads to a disc destruction rate of less than 20% in this regime.

For higher cluster densities the favored encounter scenario changes (Fig. 4.9b). Interactions between low-mass stars become increasingly important leading to large disc-mass losses for stellar masses of $M_1 < 10\,\mathrm{M}_\odot$. Disc-mass losses of the high-mass stars ($M_1 > 30\,\mathrm{M}_\odot$) are less prominent, however, still $\approx 50\%$ of the massive stars loose their disc.

How do these results relate to the effect of the initial disc-mass distribution? Figure 4.10 shows the difference between the fraction of destroyed discs for initially constant and $r^{-7/4}$ disc-mass distributions as a function of the stellar mass. For dense clusters the relevance of the initial disc-mass distribution significantly depends on the mass of the central star. For high stellar masses the encounter mass ratios are usually well below $M_2/M_1 < 0.5$, leading to only minor differences in the disc losses for different disc-mass distributions as has been shown in Section 3.2.2. Consequently, here the differences in the fraction of disc-less stars are found to be relatively low ($< 10\%$).

However, for $M_2/M_1 > 0.5$ much larger differences between the investigated disc-mass distributions have been found, e.g. $> 25\%$ in a single encounter event with $M_2/M_1 = 1.0$

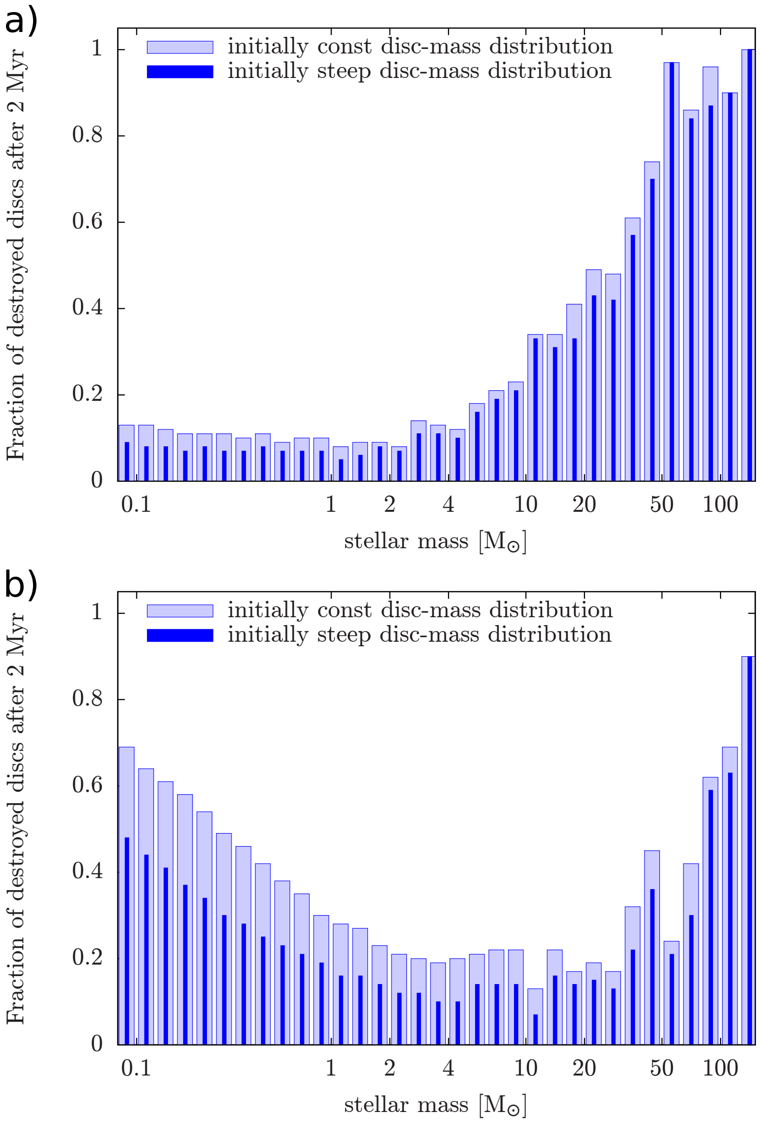

Figure 4.9: The fraction of destroyed discs after 2 Myr is plotted as a function of the mass of the central star for (a) Model *A* and (b) Model *F*. The results are presented for an initially constant (light blue) and $r^{-7/4}$ disc-mass distribution (dark blue). The errors are in general ≈ 2% but depend strongly on the mass range. Due to a lower number of massive stars per cluster the errors increase to 10% in the high-mass regime.

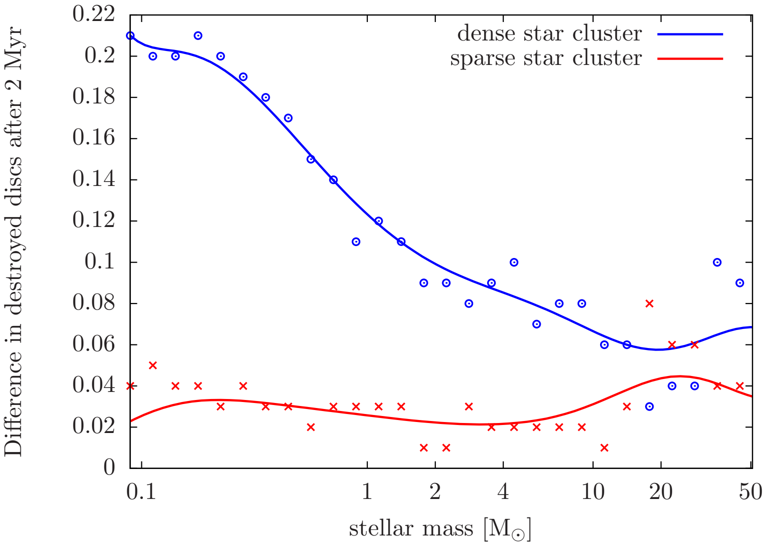

FIGURE 4.10: Shown is the difference in destroyed discs after 2 Myr between an initially constant and a $r^{-7/4}$ disc-mass distribution as a function of the stellar mass. The results are presented for Model A (red crosses) and Model F (blue circles). The lines represent Bezier curves. Stellar masses $> 50\,\mathrm{M}_\odot$ have been excluded due to a low number of stars in these mass regime and errors of up to 10%.

and $r_{\mathrm{peri}}/r_{\mathrm{disc}} = 1.0$. Such large encounter mass ratios are much more likely for low- and intermediate-mass stars so that the differences between the losses for the different initial disc-mass distributions increase to up to 20% for stellar masses $< 0.5\,\mathrm{M}_\odot$. Since the large fraction of the stellar cluster members is of low-mass, the differences in the losses are dominated by the low-mass stars.

As shown before, despite the stellar masses the effect strongly depends on the stellar density. The largest differences of $> 20\%$ are found for low-mass stars in dense cluster environments, while for sparse clusters the differences are generally below 5% (Figure 4.10). By contrast, the relevance of the initial disc-mass distribution for high-mass stars is rather unaffected by the stellar density. The crucial quantity here is the number of encounters per star. In general, a higher number of encounters provides larger differences in the fraction of disc-less stars between an initially constant and a $r^{-7/4}$ disc-mass distribution. However, as has been shown in Figure 3.6 the significance depends on the encounter mass ratio.

Figure 4.11a shows the averaged number of encounters as a function of the mass of the central star after 2 Myr for the inner cluster region of sparse clusters. It can be seen, that low-mass stars, which maintain their disc, experienced usually less than two encounters per star, while the number of perturbations for disc-less stars has been five times higher. Here, it can be deduced that the higher the mass of the central star the larger is the number of encounters. Due to an average of more than 500 encounters per star the discs of the most massive stars ($M_1 > 50\,\mathrm{M}_\odot$) are generally completely destroyed.

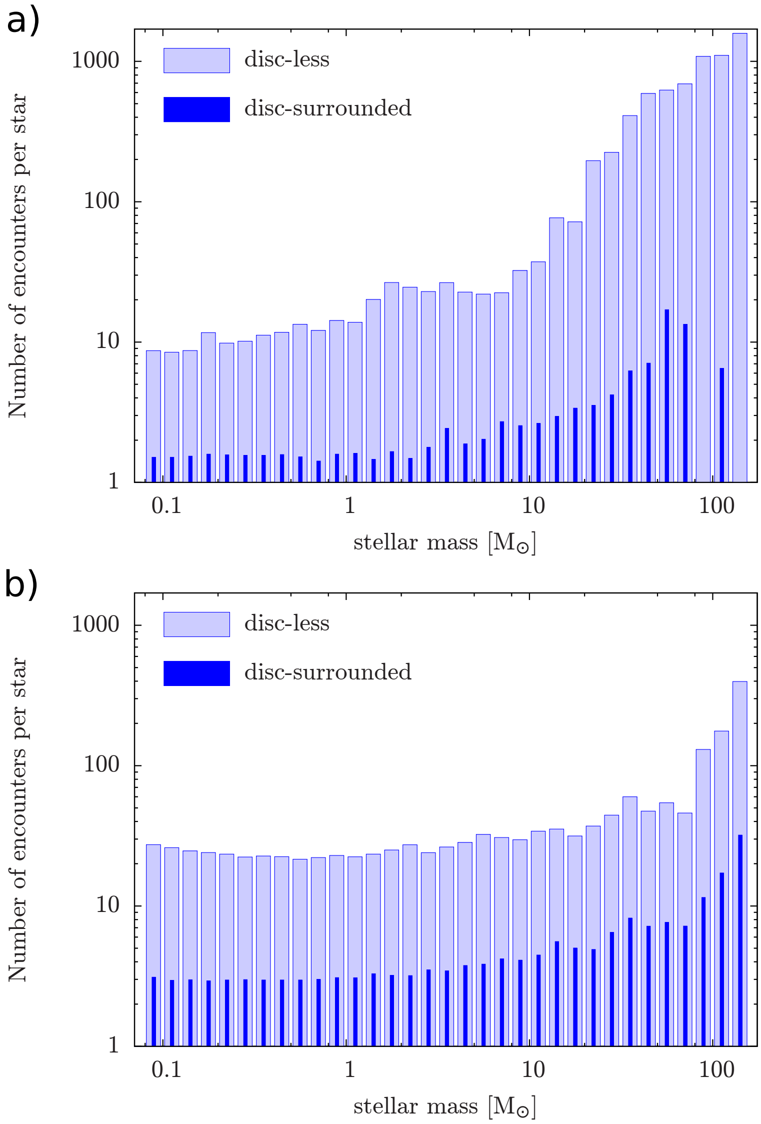

FIGURE 4.11: The averaged number of encounters per star after 2 Myr of evolution is plotted versus the mass of the central star for (a) Model *A* and (b) Model *F*. The results are shown for the fraction of disc-less stars (light blue bars) and the fraction of stars that maintain their discs (dark blue bars). A constant initial disc-mass distribution was used since the number of encounters does only slightly deviate for the different investigated initial disc-mass distributions.

For dense clusters, like Model *F*, shown in Figure 4.11b, the number of encounters for low- and intermediate-mass stars increases significantly. While all disc-less stars experienced on average > 25 encounter events, the fraction of encounters of the disc-surrounded stars is on average one magnitude smaller. For stellar masses $M_1 > 75\,\mathrm{M}_\odot$ gravitational focusing still leads to encounter rates of > 100 per star.

In summary, in sparse clusters differences in the fraction of destroyed discs due to varying initial disc-mass distributions are negligible. However, for densities $\rho_{\mathrm{core}} > 10^4\,\mathrm{pc}^{-3}$ the increasing number of encounters between low-mass stars results in considerably more discs being destroyed in case of initially flat disc-mass distributions. The disc fraction of massive stars remains rather unaffected since their discs are either completely destroyed or consistently perturbed.

4.5 Discussion

The here obtained results represent upper limits for the influence of encounters in the different stellar environments. The validity of assumptions made will be discussed in the following.

Although each star in the cluster is assumed to be initially surrounded by a disc, at the same time only encounters with a disc-less perturbing star have been investigated to obtain the disc losses. However, Pfalzner *et al.* (2005a) showed that star-disc encounter results can be generalised to disc-disc encounters as long as there is no significant mass exchange between the discs. In case of close encounters the discs might be replenished to some extend, which would lead to an overestimate of the losses in strong perturbing encounters.

Another simplification here is the focus on prograde, coplanar encounters. If the cluster is not highly rotating, an allignment of the disc and the encounter plane seems rather unlikely. Pfalzner *et al.* (2005b) showed that, as long as the inclination is not larger than 45 degrees, the disc losses are only slightly reduced in comparison to a coplanar encounter. Hence, if the orientations were completely randomly distributed the losses would be overestimated in 75% of the encounters.

Similarly, it has been assumed that the relative losses remain unchanged in a consecutive encounter. Pfalzner (2004) showed that for equal-mass perturbers a second encounter results not in the same absolute but relative losses as found for the first encounter (see also Tackenberg, 2009). However, since the perturbations also lead to a hardening of the remaining discs, our treatment of repeated encounters might lead to an overestimate of the losses.

Additionally, encounters have been generally treated as parabolic ($\epsilon = 1$) throughout this work. Due to the shorter interaction time scales the total disc losses would drop considerably for hyperbolic encounter orbits ($\epsilon > 1$). In sparse clusters such hyperbolic encounters can be generally neglected. By contrast, the average eccentricity of the stellar orbits is higher in case of dense stellar environments, where the massive stars loose their dominating role as encounter partners (Olczak *et al.*, 2010).

Another significant factor for disc losses is the initial disc size. Small disc sizes lead to higher relative periastron distances $r_{\text{peri}} = r/r_{\text{disc}}$ and therefore lower disc losses in our calculations. In this context, observations give no clear picture, providing a multitude of observed disc-mass distributions and sizes. Thus, here, the discs are assumed to have a radius with $r_{\text{disc}} = 150\,\text{AU}$, which is a typical observed value. However, a scaling of the disc size with the mass of the disc-surrounded star by $r_{\text{disc}} = 150\,\text{AU} \cdot \sqrt{M_1[\text{M}_\odot]/\,\text{M}_\odot}$, as it is obtained if a fixed force of the stars at the discs outer radius is assumed, would be equally likely. This would result in an increased disc diameter of massive stars ($m_{\text{star}} > 1\,\text{M}_\odot$) while the disc sizes of low-mass stars ($m_{\text{star}} < 1\,\text{M}_\odot$) are significantly reduced. In the consequence this would lead to a lower fraction of destroyed discs, since the majority of stars in the cluster is located in the low mass regime.

All of above simplifications might lead to an overestimating of the presented disc losses. However, some of the applied assumptions potentially lead to an underestimating.

First of all, sub-stellar objects ($M_{\text{star}} < 0.08\,\text{M}_\odot$) have been excluded in the present study. In general, the mass ratios in encounters with such low-mass objects are well below 0.1, which implies that the disc losses would be sufficiently small ($< 10\%$). Hence, the effect should be minor for massive stars. If the encounter is non-penetrating the effect can be neglected even for low-mass stellar objects.

Furthermore, all encounter processes have been treated as two-body encounters. Umbreit (2001) showed that multiple-body encounters result in larger disc losses. However, the effect strongly depends on the mass and periastron distance of the involved stars. For the present calculations the most destructive encounter has been used to obtain the disc losses, while the other encounter partners are most likely either distant or less massive, so that their influence on the losses is less significant.

Primordial binaries have not been included, which might significantly underestimate the destruction rates of stellar discs in the portion of tight binaries. While it is suggested that up to 100% of all stars (e.g. Kroupa, 1995, and references therein) might be initially part of a binary system, it remains unclear how their initial periods are distributed. Assuming the upper limit case of an initially log-uniform period distribution (e.g. Reipurth *et al.*, 2007) a fraction of 50% of all stars would have had a companion with a semi-major axis $\leq 100\,\text{AU}$. This would have a non-negligible effect on the disc fractions and stellar dynamics and further investigations are needed to give an estimate of the effect.

Finally, a large fraction of disc-less stars is ejected after an encounter event within the first few 10^5 yr with velocities larger than 20 pc/Myr, populating regions of > 20 pc distance from the cluster center. In the context of planet formation such stellar high-velocity escapers from embedded clusters are expected to show no infrared excess emission and to be less frequently surrounded by planets. Similar results have been obtained from observational (Hillenbrand, 1997; Lada *et al.*, 2004) and numerical studies that assumed primordial mass segregated populations (Olczak *et al.*, 2008). However, such high-velocity escapers are less frequent for primordial non-mass segregated clusters. Here, a first approach showed that in contrast to evenly distributed clusters, in mass-segregated clusters a lower fraction of disc-less stars remains in the core region as more stars are ejected due to gravitational focusing of the high-mass stars. The consequence is an increased fraction of disc-less stars in the core region of primordial non-mass segregated clusters of up to 10% in the tested extreme cases.

4.6 Summary

Stellar clusters spanning a large range of densities have been modeled and the influence of these different environments on the disc fraction has been investigated. The focus was on the effect of the initial disc-mass distribution. The main results are:

1. Surprisingly, even though the initial disc-mass distribution significantly influences individual disc losses induced by stellar interactions, the total number of perturbed discs remains virtually unaffected.
2. Similarly has the initial disc-mass distribution only a minor influence on the fraction of discs that are completely destroyed by encounters, as long as the cluster density is low ($\rho_{\text{core}} < 10^4\,\text{pc}^{-3}$). The reason is that for low-density clusters interactions with high-mass stars dominate, which are rather unaffected by the initial disc-mass distribution.
3. By contrast, for very high cluster densities the fraction of destroyed discs depends to some degree on the initial disc-mass distribution - e.g. 60% of discs are destroyed assuming initially constant disc-mass distributions while for an initially steep disc-mass distribution ($\Sigma \propto r^{-7/4}$) only 40% are destroyed. Here, interactions between low-mass stars are more frequent, which show the largest dependencies on the mass distribution. In general, the fraction of destroyed discs deviates at most $\approx 20\%$ from an initial r^{-1} disc-mass distribution.

We find evidence, that independent of the initial distribution of the disc material, almost all circumstellar discs (95%) in the core region ($r_{\text{core}} = 0.3\,\text{pc}$) of dense clusters are significantly perturbed. However, the prominent influence on the disc survivability around stars with $< 10\,\mathrm{M}_\odot$ would have a non-negligible effect on the frequency of sun-like planetary systems in dense cluster environments.

5 Cluster expansion phase

So far, embedded clusters in virial equilibrium have been investigated. But once a sufficient number of stars have been formed within such an embedded cluster, the remnant surrounding gas is rapidly expelled by stellar winds, ionizing UV radiation of the massive stars, and first supernovae explosions (Hills, 1980; Kroupa *et al.*, 2001; Fellhauer & Kroupa, 2005; Goodwin & Bastian, 2006; Bastian & Goodwin, 2006; Baumgardt & Kroupa, 2007; Dale *et al.*, 2012). This clearing up unveils the dense stellar regions of the cluster where presumably most star-disc encounters take place.

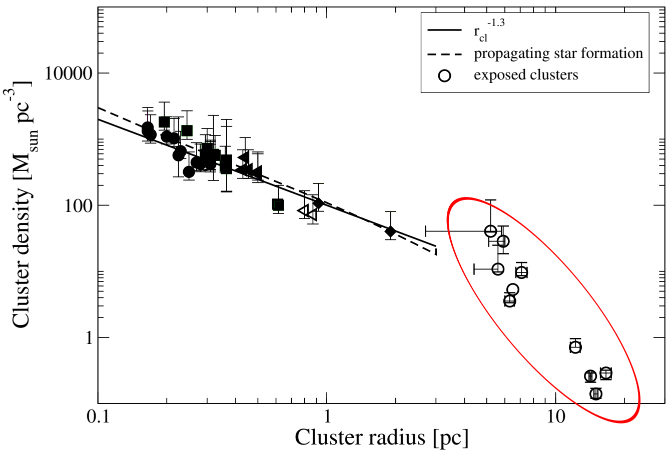

FIGURE 5.1: Same as Fig. 1.8 but here a red circle indicates the density space, which marks the here investigated parameter region assuming an initially super-virial cluster state.

In the following, we concentrate on the most massive clusters in the Milky Way, since these are the only ones where one can observationally determine the entire expansion process after the gas expulsion. The evolution of such clusters has been detailed in Section 1.5. In general, the picture is that some embedded clusters, indicated by the filled symbols in Figure 5.1, gain sufficient stellar mass before the gas expulsion to reach the branch of the leaky clusters, indicated by the open circles in Figure 5.1. Hereby, the leaky clusters provide an age sequence in the radius-density plane with young clusters evolving from the upper left towards the lower right part within 20 Myr. This evolutionary path, highlighted in red, denotes the clusters investigated in this chapter.

The process of star formation turns out to be rather inefficient with typical star formation efficiencies of $\leq 30\%$ for clusters in the solar neighbourhood (see Section 1.5.2). Therefore, in these clusters the ejection of the residual gas leads to a rapid decrease of the total cluster mass. The related reduction of the binding energy leads to a lower the escape velocity for the stars from the cluster and the residual cluster remains in a super-virial state. Stars becoming unbound from the remnant cluster cause a further depletion of its potential energy and, therefore, even more stars are expelled. The total fraction of stars that after ≈ 20 Myr remain bound as a cluster depends on the star formation efficiency ϵ, the ratio of the gas expulsion timescale to the crossing time $\tau_{\text{exp}}/t_{\text{cross}}$, and the cluster density.

If a rapid expulsion is assumed, the stars are not able to adapt their velocities to the new potential energy of the cluster, which results in a high loss of stellar members and a further decrease of the total cluster mass. Moreover, the high velocities of the bound stars will lead to an enlargement of the cluster radius since the stellar kinetic energies will be converted into potential energy until a new equilibrium state is reached and the expansion stops. In summary, the cluster expands, loses mass and thus its mass density decreases with time as indicated in Figure 5.1.

Here, as done by several previous studies (Goodwin, 1997; Goodwin & Bastian, 2006; Bastian & Goodwin, 2006; Pfalzner & Kaczmarek, 2013), the focus will be on an instantaneous gas expulsion from the clusters which has been specified in Section 2.2.2. Besides that, so far the effect of gravitational stellar interactions and their impact on circumstellar discs in such expanding stellar environments has not been investigated.

Pfalzner & Kaczmarek (2013) determined a fraction of around 4 to 7% of stars becoming unbound due to encounters in such expanded clusters. This indicates that after the gas expulsion despite the strong decrease of the stellar density encounters might exist.

5.1 Setup and method

The parameters used in this set of simulations are summarized in Table 5.1. The motivation for choosing these specific parameters is given in the following.

The masses of the youngest massive clusters shown in Figure 5.1 initially lie in a mass range from about 8 000 to 25 000 $\text{M}_\odot$ and an initial cluster radius $r_{\text{initial}} < r_{\text{evolved}} = 5-7\,\text{pc}$, where r_{evolved} is the observed radius found for the leaky clusters with age < 4 Myr. Pfalzner & Kaczmarek (2013) performed an extensive parameter study of expanding clusters, which they compared to the observational values. They found the best agreement between their simulations and the observations for an initial cluster size of $r_{\text{initial}} = 1-3\,\text{pc}$, total cluster

	variable	value
Number of star	N_{star}	30 000
Number of simulations	N_{sim}	15
Half-mass radius	r_{hm}	1.3 pc
King Parameter	W_0	9
Star formation efficiency	ϵ	0.3
Initial virial ratio	Q_0	0.5
Expulsion time	t_{exp}	instantaneous
Expulsion time delay	t_{delay}	0.0 Myr

TABLE 5.1: Properties of the leaky cluster models.

masses $> 10\,000\,\mathrm{M}_{\odot}$, and a star formation efficiency of $\epsilon \approx 0.3$. In this case at least half, but possibly all, massive leaky clusters follow the observed sequence.

Here, a similar parameter study is performed, but this time with the emphasis on the encounter history. Simulations were performed with an initial stellar mass of $18\,000\,\mathrm{M}_{\odot}$, corresponding to 30 000 stellar members, which represents the mean total stellar mass expected for young leaky clusters and lies well above the lower limit of $10\,000\,\mathrm{M}_{\odot}$ (Pfalzner, 2009). The half-mass radius of the cluster is set to $r_{\mathrm{hm}} = 1.3\,\mathrm{pc}$, which corresponds to the best fitting models in Pfalzner & Kaczmarek (2013). Assuming a low value for the half-mass radius seems reasonable since stellar evolution, primordial stellar binaries, and interactions with an external tidal field have not been taken into account in our study, which might lead to an underestimation of the cluster expansion after > 10 Myr (see Section 1.5.2 for more details). In the following, a star formation efficiencies of $\epsilon = 0.3$ will be assumed. The cases of $\epsilon = 0.2$, $\epsilon = 0.4$, and $\epsilon = 1.0$ have been simulated as well but will only be mentioned explicitly in the respective cases.

The focus here is on the post-embedded cluster phase after an instantaneous rapid expulsion of the residual gas component. The aim is to investigate the relevance of star-disc encounters during the induced dynamical expansion of the cluster. In Section 1.5.2 is outlined, that the timescales of the gas expulsion process strongly influence the development of the emerging remnant cluster. However, gas expulsion is expected to proceed rather quick (Goodwin, 1997; Fellhauer & Kroupa, 2005), which is why a first adequate estimate is an instantaneous gas expulsion from the cluster. In the massive clusters that is not only caused by the high stellar densities but also because the likelihood of massive stars increases. Due to strong stellar feedback, in particular from the massive stars, the gas ejection phase in such massive populations is significantly accelerated. Therefore, an instantaneous gas expulsion is investigated in the following simulations.

Furthermore, the clusters are assumed to be in virial equilibrium ($Q_0 = 0.5$) before the onset of the gas expulsion so that any star formation efficiency $\epsilon < 1.0$ will lead to an expanding cluster (Sec. 2.2.2). This has been done since it is supposed that gas expulsion occurs after a few crossing times ($t_{\text{cross}} = 0.3$ Myr) so that the stars had sufficient time to virialise (Lada *et al.*, 1984).

In contrast to the clusters being in virial equilibrium, as assumed here, a sub-virial dynamical state of the stellar clusters before gas expulsion has been suggested (Geyer & Burkert, 2001; Goodwin, 2009; Allison *et al.*, 2009). This would result in a higher finally bound cluster mass even in case of very low star formation efficiencies. According to Equation 2.32 it follows that even if an initially contracting stellar population would be assumed ($Q_0 < 0.5$) it might expand after the expulsion of the gas whenever $\epsilon < 2Q_0$. Furthermore, Equation 2.32 indicates that in case of an instantaneous gas expulsion the results can be applied to arbitrary initial virial ratios, so that the here termed star formation efficiency is in fact an *effective* star formation efficiency (Verschueren & David, 1989; Goodwin & Bastian, 2006), which is a measure of how much the cluster deviates from virial equilibrium after the remnant gas is expelled. Since in our case the clusters are initially in virial equilibrium, the effective star formation efficiency is equivalent to the star formation efficiency. Although only initially virialised clusters will be investigated in the following, the here presented results are therefore also applicable for observed non-virial clusters mentioned above.

Since, according to Equation 2.32, the virial ratio after the instantaneous gas loss can be simply adapted by the star formation efficiency, an initial virial ratio of $Q = Q_0/0.3 = 1.67$ is obtained in the present case of $\epsilon = 0.3$ and $Q_0 = 0.5$. Accordingly, the initial velocity dispersion σ is a factor of $\sqrt{1/\epsilon} = 1.83$ larger than obtained for virial equilibrium (see Eq. 1.6).

The stars have initially been distributed according to a King profile of $W_0 = 9$, which seems to be a reasonable estimate for young massive clusters in the late embedded stage (see Section 2.3). In previous studies the often used Plummer model generally leads to a strong decrease in the residual bound stellar mass due to its much flatter distribution in the central cluster regions. By contrast, the here used King distribution is much more concentrated in the inner cluster regions making such clusters prone to gravitational interactions of the stellar members. A detailed characterisation of Plummer and King profiles is presented in Appendix C.

5.2 Cluster survivability

Several studies investigated the fraction of stars that remain bound to their natal cluster after the gas expulsion process (see e.g. Figure 1.9). Here, a short overview of the cluster survivability in dependence on the star formation efficiency will be given for the here used model cluster described above.

In Figure 5.2 the fraction of bound stars is shown as a function of the simulation time t_{sim}, where $t_{\text{sim}} = 0$ denotes the time step of the instantaneous expulsion of the gas. Note, that the simulation time is not equal to the cluster age, since the evolution during the embedded phase has not been considered in this part of the study. Shown are the results for star formation efficiencies of $\epsilon = 0.2$ (blue), 0.3 (red), and 0.4 (green), as well as for a star formation efficiency of $\epsilon = 1.0$ (black) for comparison.

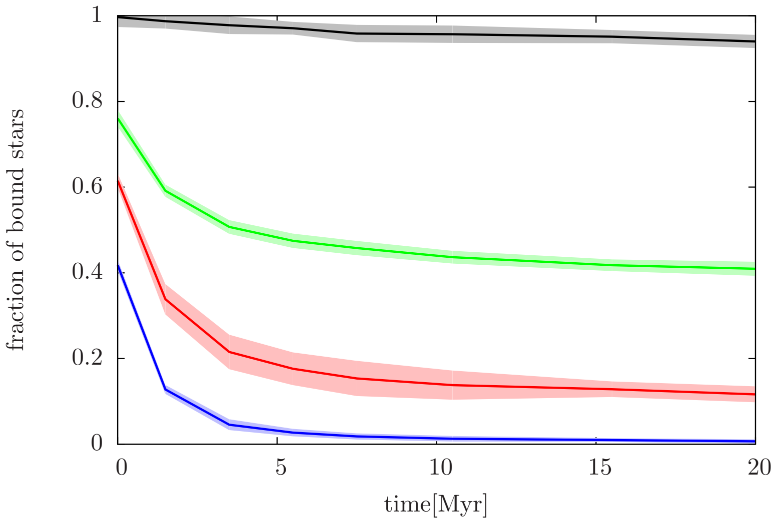

FIGURE 5.2: Shown is the fraction of bound stars as a function of the time. Here, for $t_{\text{sim}} = 0$ the gas is expelled instantaneously. Star formation efficiencies of 20% (blue), 30% (red), 40% (green), and 100% (black) are shown. The error bars are obtained by the standard deviation.

It can be seen that the bound fraction of stars rapidly decreases within the first 20 Myr. For a star formation efficiency of 100% the cluster is initially set up in virial equilibrium. Such a large star formation efficiency implies the unlikely case that all gas is converted into stars. However, a fraction of 5% of the stars is found to be ejected from the cluster in that case. Such ejections are caused by strong few body interactions with the massive cluster members. Here, the rather constant decrease of the fraction of bound stars indicates a steady ejection process for at least the first 20 Myr.

The fraction of bound stars depends strongly on the star formation efficiency. For the star formation efficiency $\epsilon = 0.2$ the fraction of bound stars decreases quickly within the first 5 Myr. Eventually, a remnant cluster of at most a few hundredth of its initial members remains. Directly after the gas expulsion ($t_{\mathrm{sim}} = 0$) already 60% of the stars are unbound because their velocities exceed the escape velocity of the cluster. Unbound stars leaving the cluster lead to a further decrease of the total cluster mass and, thus, a reduction of the escape velocity, which causes even more stars to leave the cluster. The result is a runaway process due to a gradual decrease of the residual stellar potential by the escaping stars, which ends in an almost total dissolution of the cluster.

For $\epsilon = 0.3$ a bound cluster remains, although significantly reduced in stellar members. Here, a final stellar population of ≈ 3000 stars (10%) is still bound after 20 Myr. For an even higher star formation efficiency of $\epsilon = 0.4$ the fraction of bound stars decreases only to about 40%. Further results of similar investigations are summarised in Section 1.5.2.

In the following the radial evolution of the stellar members will be further detailed and the overall importance of encounters will be investigated. Afterwards, the frequency of encounters will be specified for the two groups of bound and unbound stars as well as their radial dependence.

5.3 General cluster dynamics

Here, we are interested in the effect of gravitational star-disc interactions in rapidly expanding stellar populations. This has so far not been investigated since the importance of encounters in stellar clusters has been largely underestimated in the past (see Section 1.4). However, as shown in Chapter 4, even in sparse stellar clusters a significant number of encounters might occur.

In accordance with Section 3.2.5, a circumstellar disc is defined as being perturbed if $> 5\%$ of its angular momentum is removed by a stellar fly-by. As investigated in Section 4.4 the number of encounters is found to be independent of the initial disc-mass distribution in that case. Therefore, the following results are presented for initially constant disc-mass distributions.

Focusing on the dynamical cluster evolution after the dispersal of the gas two groups of stars can be distinguished: (i) stars that remain as a bound population and (ii) stars, whose velocities exceed the binding energy of the cluster. Immediately after the gas expulsion, these two superposed groups can hardly be distinguished by observations since a detailed determination of the stellar velocities for each spatial direction would be required. Even if the proper motion and radial velocities were determined, the escape velocity of the individual stars (see Equation 1.10 for a spherical, homogeneous mass distribution) remains hard to constrain. For any unbound star that is finally separated from the remnant cluster the cluster potential energy is further decreased so that the escape velocity strongly varies with time. However, numerically no such limitations are given. In the following the two groups will be treated separately while the effect of the initially overlying populations on observations will be investigated in Section 5.4.3.

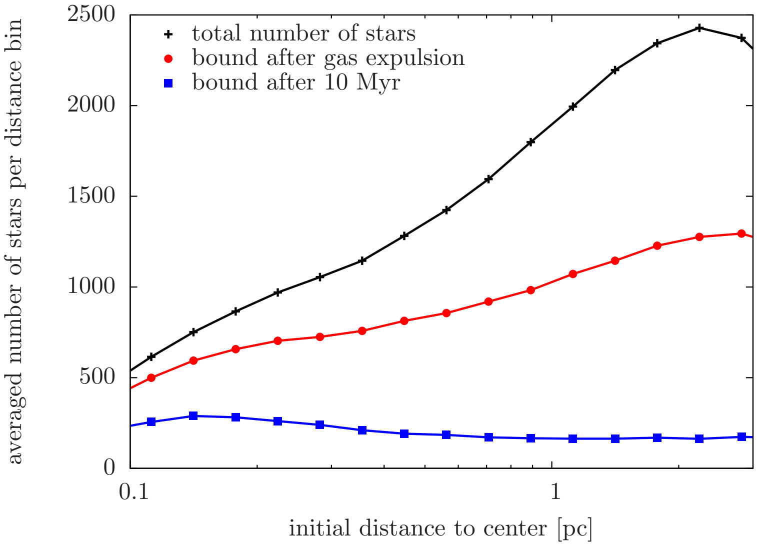

FIGURE 5.3: Averaged number of stars per radial bin as a function of the initial distance to the cluster center for $\epsilon = 0.3$. Black crosses indicate the total number of stars, red circles the number of stars that are bound to the cluster at the start of the simulation, and blue squares stars that remain bound after 10 Myr.

First, the cluster evolution is further detailed in terms of the temporal development of the two groups. Therefore, in Figure 5.3 the number of bound stars is shown as a function of the initial distance to the cluster center for the inner 3 pc. Comparing the total number of stars (black line) to the number of stars that are bound instantaneously after the gas expulsion (red line) shows that a large fraction of stars ($\approx$ 40%, Fig. 5.2) have high velocities that exceed their local escape velocities. The largest fraction of escapers is initially located in the outer cluster parts (> 1 pc) since their velocities are more likely to exceed the escape velocity. Contrary most of the innermost stars remain captured within the inner potential well. With time the number of bound stars further decreases. After 10 Myr (blue line) more than 90% of the stars initially located in the outer cluster region are expelled from the cluster. However, nearly half of the stars that are initially located within the innermost cluster part ($\approx$ 0.1 pc) remain bound, providing a peak in the number of stars which extends up to 0.4 pc from the cluster center.

The question arises how the positions of the bound and unbound particles change with time. In Figure 5.4 the averaged number of stars per radial bin is shown as a function of the distance to obtain the intrinsic distribution of the stars after 10 Myr. The core region is populated by a substantial number of bound stars that diffuse out to distances

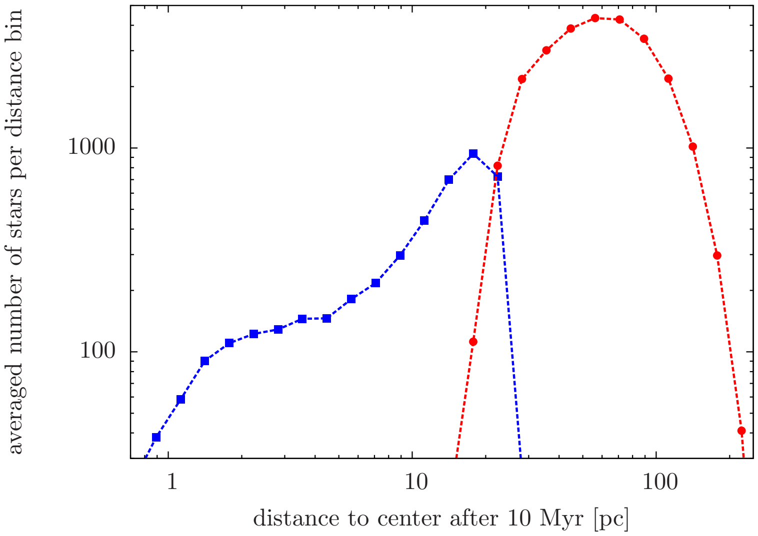

FIGURE 5.4: Shown is the average number of stars per radial bin versus the distance to the cluster center after 10 Myr with $\epsilon = 0.3$. Red circles indicate unbound stars, while blue squares represent bound stars. All shown data bins contain on average more than 30 star.

of up to 20 pc. Between $10 - 30$ pc a transition from mostly bound stars to an increasing fraction of unbound stars can be determined. Outside 30 pc all stars are unbound with the major fraction of unbound stars being expelled to distances > 50 pc. Due to the fact that the bound and unbound fraction of stars are nearly completely separated indicates that the enclosed mass, and therefore the escape velocity, will remain rather constant over time. However, some stars located in the outskirts of the remnant bound population, where bound and unbound stars still coexist, might become unbound during the following cluster development.

In Figure 5.5 the averaged initial distance to the cluster center is shown as a function of the distance after 10 Myr to reveal the movement of the bound and unbound stars. As pointed out before, within 10 pc a restructured bound cluster remains. Its innermost regions of < 6 pc mainly consist of stars that have been located within < 1 pc before the gas expulsion process. Moreover, the vast majority of the bound stars has been initially located within the inner 2 pc from the cluster center.

By contrast, the unbound stars are rapidly expelled from the cluster. In general, the process of stars becoming unbound can be divided in *two phases*. In the *first phase* the high velocity stars, which exceed the local escape velocities, are rapidly expelled from the cluster to distances > 30 pc. Some of the stars initially located close to the cluster center might reach large distances of up to 200 pc due to the high initial velocity dispersion in this regime and an accompanied prominent fraction of stars residing in the high velocity tail.

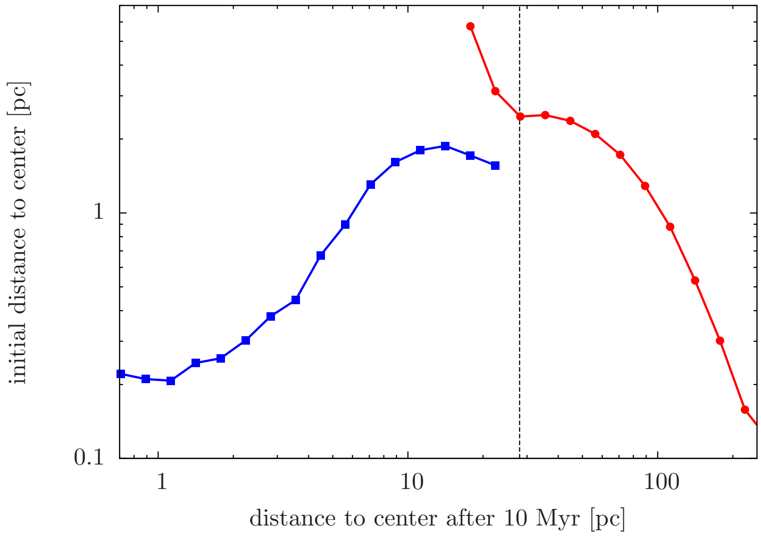

FIGURE 5.5: Shown is the averaged initial distance to the cluster center as a function of the distance to the cluster center after 10 Myr with $\epsilon = 0.3$. Red circles indicate unbound stars, while blue squares represent bound stars. All shown data bins contain on average more than 30 star.

Consequently, these high velocity stars have to pass the entire remaining stellar population early on.

The loss of stars during the *first phase* significantly reduces the binding energy of the cluster, which leads to a further dispersion of the population. Inferred by this *second phase* preferentially stars located in the outer regions are expelled from the cluster since the local escape velocity stabilises from inside out. In Figure 5.5 the sharp edge in the red line around 30 pc separates such recently expelled outer stars from the major population of unbound stars. For < 30 pc - the earlier stated transitional region where both groups of unbound and bound stars coexist - a distinctive peak in the distribution of the unbound population appears, with most stars initially located > 3 pc.

In total, it can be deduced that the remaining bound cluster consists of stars initially located in $1 - 2$ pc from the cluster center that are spread over several parsec after the gas expulsion, while in particular the number of stars in the outer cluster regions is largely reduced.

Figure 5.6 shows the temporal development of the Lagrange radii for stars that are bound to the cluster. Within the first Myr the cluster rapidly expands due to the super-virial velocities of the stars. For stars that are initially located inside 1 pc distance to the cluster center the radial distance increases by about one magnitude. This means that stars initially located within 0.1 pc reach a virial equilibrium state for 1 pc distance from the cluster center after about 1 to 2 Myr. It implies that after such short time scales

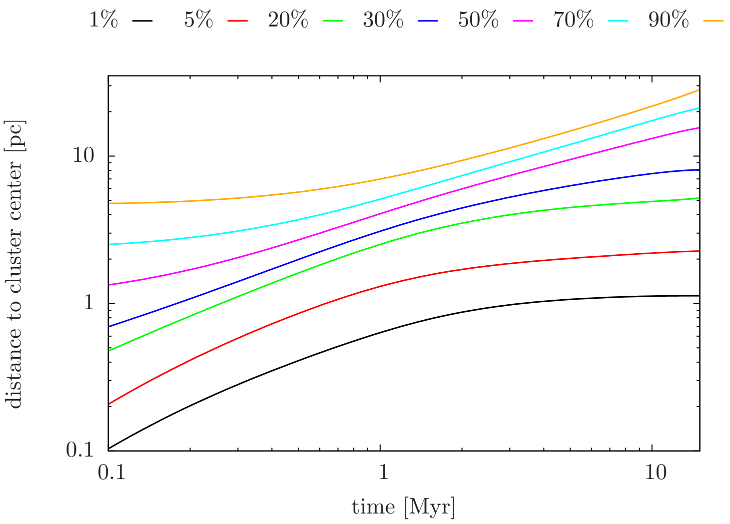

FIGURE 5.6: Lagrange radii as a function of the simulation time for the bound fraction of stars. The Lagrangian radii are presented for enclosed mass fractions of 1%, 5%, 20%, 30%, 50%, 70%, and 90%.

all unbound stars have been expelled from within this inner region. With time the cluster further expands and the unbound stars separate from the remnant bound population. After about 10 Myr the innermost 30% of the bound stellar mass are found virialised and the vast majority of the bound population is located within 20 pc from the cluster center.

Having investigated the motion of the stars, another important quantity of the stellar cluster is its local volume density, which is shown in Figure 5.7 for the bound fraction of stars as a function of the time. After the expulsion of the residual gas the local density drops rapidly below 10^4 stars per pc^{-3}. It can be seen that stars that have been part of a disc-perturbing encounter event (red line) are initially located in the dense parts of the cluster. By contrast, stars with unperturbed discs (black line) reside in regions, which are on average half as dense. After a few Myr the expansion of the cluster population decelerates since part of the high kinetic energy of the stars is converted into potential cluster energy. Stars with perturbed discs approach a new state of equilibrium after about 2 Myr while for stars with unperturbed discs the curve flattens slightly delayed. Considering that the major fraction of bound stars with perturbed discs remains in the innermost regions of the cluster this is in accordance with our previous results (Sec. 1.4.2).

5.4 Importance of encounters

A first step to qualify the importance of encounters during the expansion phase of the cluster is to investigate the actual number of perturbed discs as a function of the simulation time, which has been plotted in Figure 5.8. The results are presented for the total number of

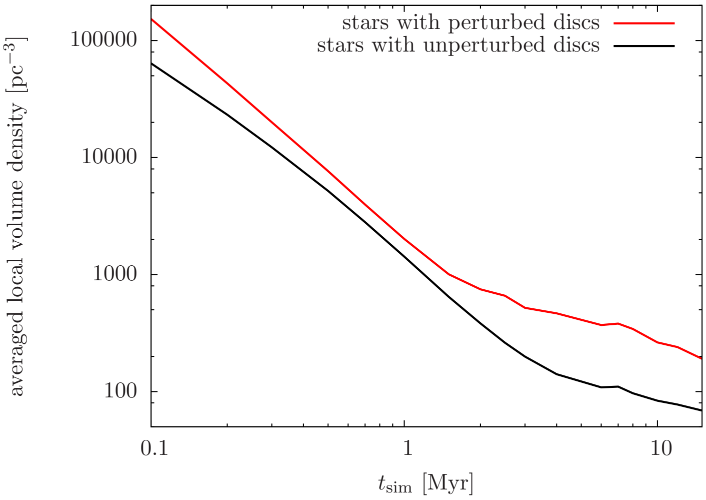

FIGURE 5.7: Shown is the averaged local number volume density as a function of the simulation time for the bound stellar population. The red line indicates stars that were part of a disc-perturbing encounter event and the black line represents stars with unperturbed discs.

stars ($N_{\mathrm{total,pert}}/N_{\mathrm{total}}$, dashed line) as well as the bound ($N_{\mathrm{bound,pert}}/N_{\mathrm{bound}}$, solid line) and unbound ($N_{\mathrm{unbound,pert}}/N_{\mathrm{unbound}}$, dotted line) fraction. It can be seen that the total fraction of perturbed discs increases rapidly within the first 10^5 yr, since the cluster density remains sufficiently high, but that the curve flattens subsequently to a total of around 10% of the discs being perturbed. During the further expansion of the cluster the total fraction of perturbed discs remains constant since the stellar density drops significantly (Fig. 5.7).

Focusing on the large fraction of unbound stars a similar picture is obtained. After a rapid increase shortly after the expulsion of the gas the fraction of perturbed discs remains constant at 9%.

For the fraction of stars that remain bound as a cluster, we find again a similar amount of around 10% of the bound stars being part of a recent disc-perturbing encounter event within the first 10^5 yr, where the cluster is still very compact. However, during the further expansion of the cluster the fraction of perturbed discs increases significantly to $> 25\%$ until the cluster reaches its new equilibrium state. This might either indicate that encounters of the bound residual cluster members *after* the gas expulsion phase are a frequent event or that an increased fraction of stars with unperturbed discs becomes unbound. Although the total number of stars has been found to remain rather constant the former has to be considered due to the much lower number of bound stars.

To frame the prominent process the sub-group of stars that remain bound after 20 Myr has been plotted in Figure 5.9. It is found that the majority of discs surrounding finally bound stars (24%) are perturbed early on. However, a rather small amount of 2% is part

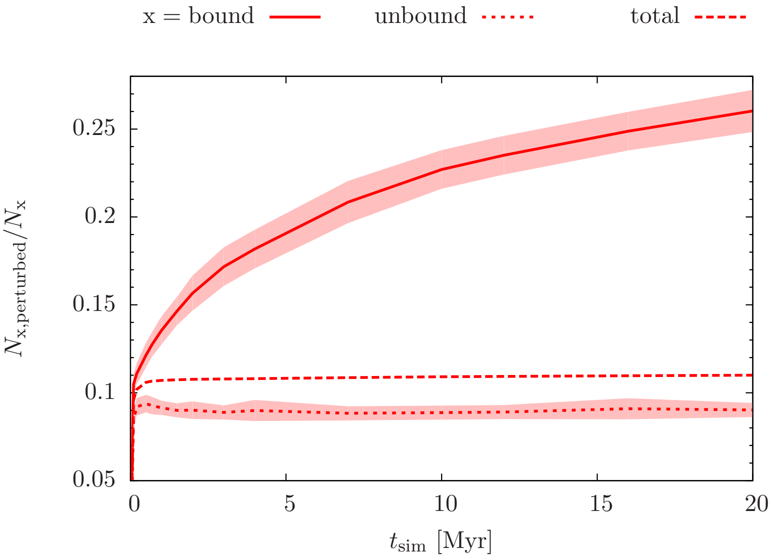

FIGURE 5.8: Shown is the fraction of stars with perturbed discs as a function of the time for the sub-samples of bound (solid line), unbound (dotted line), and total number of stars (dashed line). The filled curves indicate the standard deviation. For the total fraction the error is below 0.5%.

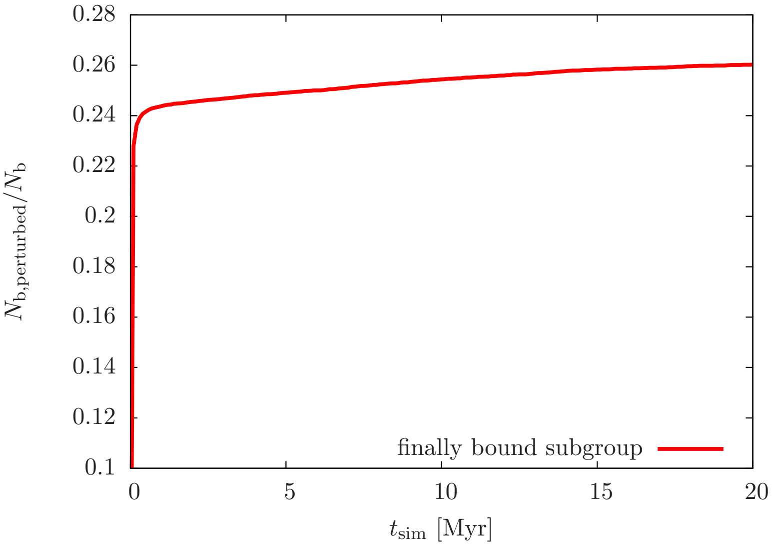

FIGURE 5.9: Like Figure 5.8 but focusing only on the sub-group of stars that are bound after 20 Myr.

of an encounter in the subsequent developmental phase as can be deduced from the slightly increasing fraction of perturbed discs.

Hence, supported by the results for the dynamical cluster evolution, here, it can be concluded that the significantly differing fraction of perturbed discs, as seen in Figure 5.9, is caused by preferentially stars in the cluster outskirts becoming unbound.

5.4.1 Dependence on stellar mass

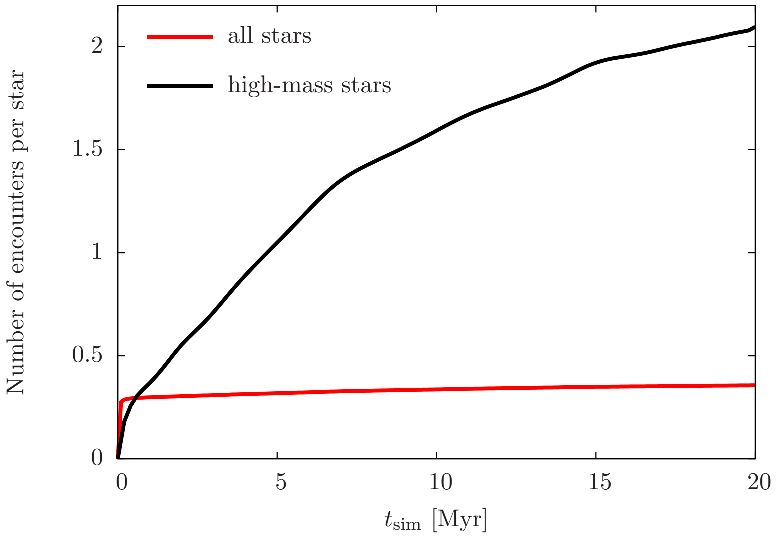

FIGURE 5.10: The number of encounters per star as a function of the time. Here, the focus is on the sub-samples of the high-mass stars ($m_{\rm star} > 7\,\mathrm{M}_\odot$, black line) and the total number of stars that are bound after 20 Myr (red line).

Investigating stellar interactions in sparse environments, the fraction of high-mass stars is of unique importance (see also Section 4.4.2). Figure 5.10 shows the average number of encounters per star as a function of the time after gas expulsion for the total number of stars and explicitly for the number of high-mass stars ($m_{\rm star} > 7\,\mathrm{M}_\odot$, which equate to a number fraction of 1% of the total number of stars). As before, the focus here is on the sub-group of finally bound stars. From the total number of bound stars can be deduced that multiple encounter events are very rare with on average one out of four stars being part of an encounter, which is in accordance with the previously determined absolute fraction of perturbed discs (solid line in Fig. 5.8).

However, the number of encounters per high-mass star deviates considerably from these results. Within the first 10^5 yr on average a smaller fraction of massive stars are found being part of a disc-perturbing encounter, which can simply be explained by the much weaker perturbations of their discs due to the on average lower encounter mass ratios.

With time the number of encounters increases significantly so that after 20 Myr the bound high-mass stars are on average part of around two encounter events. One explanation might be that significantly more massive stars remain bound. However, we compared the fraction of escaping high-mass stars to the total fraction of unbound stars as well as the half-mass radii of these two groups and determined no differences between the two mass groups. This is not surprising since the stellar velocities are scaled independent of the stellar mass and dynamical mass segregation can be excluded on such short time scales. Consequently, the apparent increase in encounters per high-mass stars can be retraced as gravitational focusing.

It can be concluded, that massive stars might be part of an encounter event even after the dispersion of the remaining population due to gravitational focusing while the vast majority of all encounters occurs at the start of the expansion phase.

5.4.2 Evidence for disc destruction

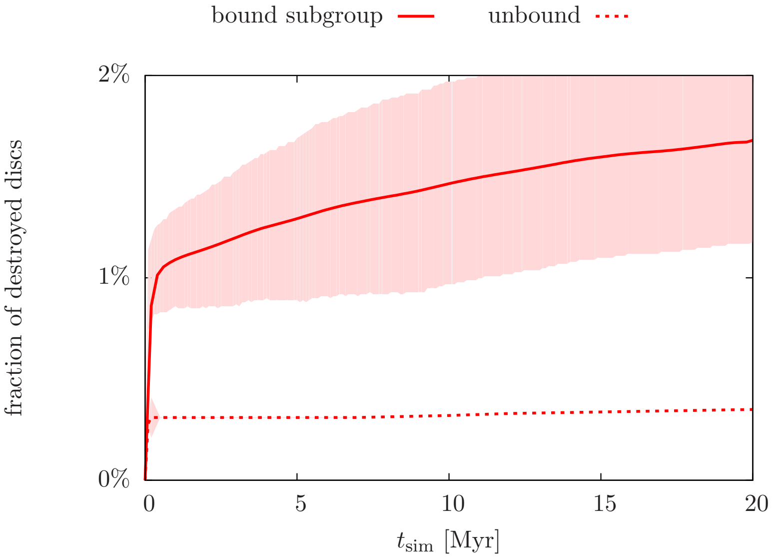

FIGURE 5.11: Shown is the fraction of destroyed discs as a function of the time after the gas expulsion. The fraction of unbound stars is shown as a dotted line and the sub-group of stars that remain bound after 20 Myr is shown in solid line. The filled curves indicate the standard deviation.

So far the focus was on gravitational perturbations of the circumstellar discs in expanding cluster environments. However, the resolution of today's observational instruments is not precise enough to dissolve such weak interaction features. As discussed in Section 1.3 a fundamental quantity observed is the cluster disc fraction. In Figure 5.11 the fraction discs that are destroyed after the gas expulsion is shown as a function of the time. Besides the group of finally unbound stars (dotted line) the sub-group of finally bound stars is presented.

For the latter, the bound stars after 20 Myr were determined and their evolution was traced back in time.

While only a minor fraction of $< 1\%$ of the unbound stars loose their disc in an encounter we find an increasing fraction of $1 - 2\%$ for the bound stars. Although the total fraction of destroyed discs remains rather low a clearly diverse evolution can be determined for the fraction of bound and unbound stars. Again, the bound stars being more frequently located in the dense inner cluster regions leads to strong encounter events early on and even some encounters during the further development as indicated by the slightly increasing number of perturbed discs.

This picture is completely opposite to what is found for virialised clusters, where stars preferentially become unbound by ejections, loosing their discs most likely in the appendant encounter event (Sec. 4.3).

5.4.3 Dependence on distance to cluster center

Observations reveal that stellar clusters might expand to $r_{\mathrm{cluster}} > 10\,\mathrm{pc}$ within the first 10 Myr of their lifetime (Fig. 1.8). While the definition of the size of a cluster appears very straightforward in case of numerical simulations, since the bound and the unbound stars can be simply separated by calculating the kinetic and potential energies of the cluster members, the definition of a cluster size (or even of a cluster itself) for comparisons to observations is very challenging in the first Myrs since bound and unbound stars can be rarely distinguished.

Observed cluster sizes are usually estimated by the half-mass radius or the median radius of a certain stellar mass range, like done by Wolff *et al.* (2007) for B-type stars. In general, a limiting surface density threshold to the surrounding field stars (Borissova *et al.*, 2008) or alternatively a fixed maximum radius (Goodwin & Bastian, 2006) is required to constrain the considered cluster area (see also Pfalzner & Kaczmarek, 2013). However, observations of circumstellar discs are in most cases restricted to the inner cluster regions of $< 5\,\mathrm{pc}$ (e.g. Lada *et al.*, 1993; Hillenbrand *et al.*, 1998; Haisch *et al.*, 2001a; Sung *et al.*, 2009) due to the high number of stellar candidates but depend considerably on the observed cluster and used instruments. Due to the lack of a beneficial parameter range for comparisons to observations, here, the focus will be on the radial dependence of the fraction of perturbed discs.

Figure 5.12 shows the influence of the considered cluster region on the total fraction of perturbed discs for different time steps. The fraction of perturbed discs is shown in red and the cumulative number of stars is shown in blue. 0.1 Myr after the gas expulsion (Fig. 5.12a) a strong radial dependence of the fraction of perturbed discs can be determined with more than 30% perturbed discs in the cluster core region ($r_{\mathrm{core}} = 0.3\,\mathrm{pc}$). If the entire cluster

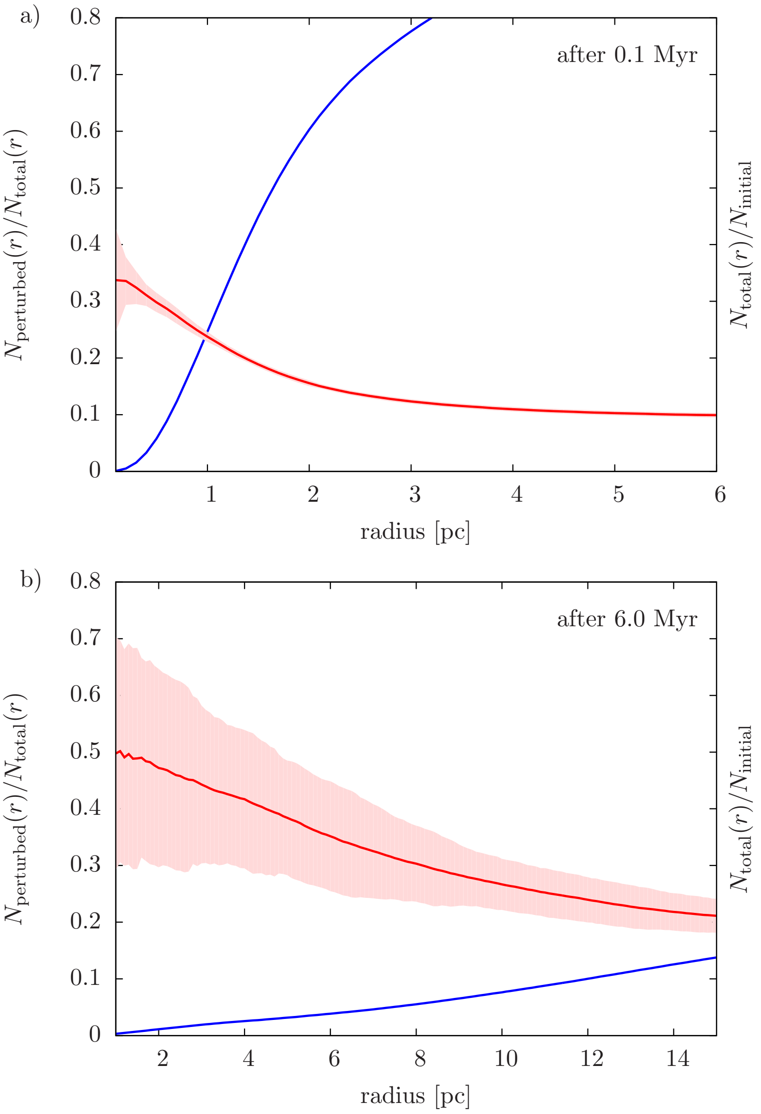

FIGURE 5.12: The fraction of perturbed discs within a sphere of radius r (red line, left y-label) and the cumulative number of stars (blue line, right y-label) as a function of the distance to the cluster center within the first (a) 0.1 Myr and (b) 6 Myr after the gas expulsion.

is considered their fraction drops down to only 10%. Hence, as expected, the majority of stellar interactions takes place in the dense central region.

With time the unbound stars are expelled from the cluster and the remnant bound population expands significantly so that after 6 Myr (Fig. 5.12b) less than 15% of the total initial population remain located within 15 pc distance to the cluster center, while the half-mass radius for the bound population is found around 10 pc. However, more than 300 stars ($\sim$ 10% of the remnant cluster) remain bound within the inner 2 pc. Although it takes several Myr for the cluster to completely separate the bound from the unbound stars, the re-virialisation process is completed at first in the inner cluster parts while the cluster outskirts might still contain a few escapers.

Focusing on the inner 1 pc of the remnant cluster, half of the discs are found disrupted, while a perturbed fraction of around 20% is obtained if all stars within the full cluster size of 15 pc would be considered. The rare cases of encounters after the gas expulsion preferentially take place in the dense central region of the cluster preserving an increase of the total fraction of perturbed discs towards the cluster center. Due to the cluster expansion these stars have most likely been initially located even closer to the cluster center where encounter events were prominent, e.g. stars within 1 pc from the center are initially found within an average distance of 0.2 pc (Fig. 5.5). The spread of the stellar population consequently leads to an outward increasing fraction of perturbed discs with time.

5.5 Discussion

Prior to the here studied gas expulsion phase the stars were exposed to the cluster dynamics in the embedded phase. However, in this chapter, all stars deliberately started out with an unperturbed disc. The benefit of this approach is that the effect of encounters during the expansion process can be separated from the prior development during the embedded phase. Considering the early interaction history before the gas expulsion would naturally provide larger values for the fraction of perturbed and destroyed discs than obtained here. The prior evolution in a virial cluster has been investigated in the previous chapter and its impact on the overall disc losses will be discussed in Chapter 6.

Stellar evolution has been neglected since it only becomes significant on much longer time scales than investigated here. The first supernovae explosions of the most massive stars are expected after a few Myr. However, the fraction of massive stars compared to the remnant population is very low, so that the mass reduction would be of the order of 5% during the first 10 Myr. The mass reduction is expected to proceed steadily so that the induced cluster expansion would be nearly adiabatic and, thus, insignificant. Nevertheless, stellar evolution eventually leads to a further dispersion of the remnant cluster and an increasing fraction of outer stars becoming unbound. This implies that the present results underestimate the expansion process on larger time scales ($>$ 10 Myr).

Another simplification is the neglect of primordial binaries. This will additionally underestimate the expansion process since the cluster dynamics are generally influenced by few-body interactions (Hills, 1975; Heggie, 1975). Again, the consequence would be a further dispersion of the stellar population, which would increase the here investigated expansion effect. However, the released energy would be small since few-body interactions become increasingly rare in the expanding clusters. Pfalzner & Kaczmarek (2013) determined a total fraction of about 5% of the stellar members being ejected from the clusters due to stellar interactions without considering primordial binaries. Including primordial binaries would presumably increase this fraction. Future investigations are needed to constrain the importance of binaries.

In this work, the focus was on the effect of the cluster expansion on encounter-induced disc losses. However, the rapid drop of the local density implies that not only encounters but as well other external disc destruction processes like photo-evaporation due to massive stars (e.g. Scally & Clarke, 2001; Clarke *et al.*, 2001; Johnstone *et al.*, 2004; Drake *et al.*, 2009) become less important for expanding clusters. Here, the reduced destruction rates are induced by the increasing radial distances to the O-stars (Johnstone *et al.*, 1998; Scally & Clarke, 2001, and references therein). So the question arises how (or if at all) circumstellar discs further disperse after the expulsion of the gas.

5.6 Summary

Not only in the embedded phase but as well in the gas expulsion phase circumstellar disc properties are influenced by stellar encounters. After the gas expulsion, which usually occurs in less than a crossing time for the here investigated massive clusters, only a small fraction of stars remains bound as a cluster, whereas the larger part of the stellar population is expelled. The super-virial cluster rapidly expands while preferentially the outer stars with unperturbed discs become unbound. The main results are the following:

1. The average distance of the remnant bound stars to the cluster center increases rapidly by about a factor of ten during the first 5 Myr after the gas expulsion. Consequently, stellar interactions are only prominent during the first few 10^5 yr after the gas expulsion. Afterwards, the local stellar densities drop rapidly below 10^4 stars per pc^{-3} where encounters are rare.

2. 25% of the stellar members that remain bound experience an encounter during the

cluster expansion phase. By contrast, only 10% of the stars that become unbound are part of an encounter event in this phase.

3. As preferentially stars from the sparsely populated cluster outskirts become unbound the field star population has a higher disc frequency than those typical observed in clusters of age > 5 Myr.
4. As an artifact of cluster expansion the observed disc frequency seems to drop. Consequently, the cluster disc fractions might provide strong upper limits for the survivability of circumstellar discs.

For the most massive clusters in the solar neighbourhood it takes ~ 3 Myr for the stars that initially populated the dense cluster core region ($r_{\text{core}} = 0.3\,\text{pc}$) to fill the inner 3 pc of the remnant cluster. As the disc fraction increases with distance to the cluster center the cluster expansion mimics a non-existent decrease in the disc fraction with cluster age. In how far this influences the results of the disc destruction as a function of cluster age requires further investigation as here not only external processes but as well internal disc destruction processes, like viscous torques, turbulent effects, and magnetic fields, play a role.

Nevertheless, early external destruction processes in the dense cluster core region might have to a large degree indirectly shaped observational results for the lifetime of circumstellar discs.

6 Conclusion

There is strong observational evidence that in stellar clusters the protoplanetary discs surrounding new born stars disappear within ~ 6 Myr after their formation (Haisch *et al.*, 2001b; Hillenbrand, 2002; Sicilia-Aguilar *et al.*, 2006; Hernández *et al.*, 2007; Currie *et al.*, 2008; Hernández *et al.*, 2008; Mamajek, 2009; Massi *et al.*, 2010). One of the key questions in this context is: Which physical mechanism dominates the rapid evolutionary disc destruction processes?

Among the established processes are *internal* processes such as viscous torques (e.g. Shu *et al.*, 1987), turbulent effects (Klahr & Bodenheimer, 2003), and magnetic fields (Balbus & Hawley, 2002), as well as *external* disc destruction processes like photoevaporation and winds from the massive stars (e.g. Scally & Clarke, 2001; Johnstone *et al.*, 2004; Ercolano *et al.*, 2008), as well as the here investigated gravitational star-disc interactions (e.g. Hall *et al.*, 1996; Pfalzner, 2004; Moeckel & Bally, 2006). However, an effect that has so far been neglected when comparing disc fractions in different star clusters is their rapid expansion after the gas expulsion. This expansion significantly influences the interpretation of observed cluster disc frequencies on time scales > 3 Myr.

In this study, the focus has been on the most massive clusters in the solar neighbourhood, since for these clusters the entire expansion process can be followed by observations (Pfalzner, 2009; Portegies Zwart *et al.*, 2010), whereas clusters of lower mass probably dissolve after the expulsion of their natal gas. In the light of our results one can conclude that the disc destruction process can be separated in an early phase, where the influence of the external processes plays a significant role, as well as a phase after the expulsion of the remnant gas, where the cluster expands and internal destruction processes might dominate. Here, the losses during the two separated evolutionary phases, namely the embedded and the expanding cluster phase, have been quantified by investigating the effect of the initial disc-mass distribution in star-disc encounters.

It remains unclear, which process dominates during the early embedded destruction phase. An often favoured destruction mechanism is photoevaporation by the surrounding massive stars, which according to numerical simulations might destroy some of the discs in the near vicinity of the high-mass stars on time scales as short as $< 10^5$ yr (Scally & Clarke, 2001; Gorti & Hollenbach, 2009). By contrast, recent observations of evaporating discs in young star clusters found that even in strong radiation fields the circumstellar material might remain bound much longer than previously assumed (Vicente *et al.*, 2013). Disc destruction by photoevaporation of the surrounding massive stars is prominent in the outer disc parts (Balog *et al.*, 2008). Therefore, assuming an initially steep distribution of the disc material would suggest a minor effect of photoevaporation on the relative mass losses of circumstellar discs, while the effect would be potentially larger if an initially flat disc-mass distributions is assumed.

Stellar encounters, although often discarded as probably unimportant, are another significant destruction process during the early embedded phase (e.g. Pfalzner *et al.*, 2005b; Moeckel & Bally, 2006; Olczak *et al.*, 2010). In contrast to what would be expected for the disc destruction by photoevaporation, in this study it has been found that the effect of encounters on the cluster disc fraction is *independent* of the initial disc-mass distribution (Chapter 4), with a large fraction of stars losing their discs completely. The highest influence on the disc losses has been found in dense cluster environments, where interactions between the low-mass stars become increasingly important. In such dense environments the time scales for individual disc destruction can be considerably short ($\sim 10^4$ yr, Eq. 1.12) and stellar interactions are frequent.

After the gas expulsion the local stellar density drops considerably. Consequently, in the later disc destruction phase external processes become less important and internal processes might dominate. The remnant gas is usually expelled quickly from the cluster ($<$ 5 Myr Whitworth, 1979; Leisawitz *et al.*, 1989; Lada & Lada, 2003). For the here investigated massive clusters this time scale might be even shorter due to a significantly high fraction of massive stars that are primarily responsible for blowing out the residual gas, thus, an expulsion of the remnant gas within the first 1 Myr seems reasonable. The gas expulsion leads to a spreading of the core regions of massive clusters from 0.3 pc to about 3 pc in $2-3$ Myr, which translates into a cluster age of $3-4$ Myr if we assume an age of 1 Myr at the end of the gas expulsion phase.

A comparison of the present results to observations has to be done carefully, since our results are limited to massive clusters and, thus, provide a lower limit for the time scales of the expansion effect. The star clusters, which shape the observed cluster disc frequency, are typically not as massive ($< 10^4\,\mathrm{M}_\odot$, e.g. Haisch *et al.*, 2001b) as the here investigated populations. In such less massive clusters the number of high-mass stars is reduced and the gas expulsion process lasts longer ($\sim$ 3 Myr), so that the effect might become apparent after $\sim$ 5 Myr.

The observations of the circumstellar disc frequencies are generally limited to the inner parts of the stellar clusters. Hereby, the typical sizes and the number of stars considered in the surveys vary between 0.3 to 3 pc and a few to several hundredths of stars, respectively

(Haisch *et al.*, 2001b; Hernández *et al.*, 2008; Mamajek, 2009). The dimensions of the observed regions are in most cases simply determined by the beam size of the telescopes and the distances to the observed populations. A consequence is that generally more stars are observed for young compact clusters (> 100), while for the sparse, expanding populations the fraction of observed stars is significantly reduced (< 50) (see e.g. Haisch *et al.*, 2001b). This might naturally result in a decreasing disc fraction - simply explained by the expansion of the dense cluster core.

Two typical clusters that are massive and old enough to have expelled their gas and reached the leaky cluster sequence are NGC 2244 and NGC 6611. Balog *et al.* (2007) analysed the spatial distribution of circumstellar discs in the $3-4$ Myr-old cluster NGC 2244, which is situated in the young part of the leaky cluster sequence. They found a cluster disc fraction of 44.5% for the innermost 2.5 pc of the cluster. Oliveira *et al.* (2005) performed a similar study for NGC 6611 and found a cluster disc fraction of 58% in the inner 3 pc of the cluster. As these clusters already expelled their gas, the disc frequencies determined for these clusters are fundamentally altered by the cluster expansion process. The core of the clusters most likely has been much more compact ($> 10^4\,\mathrm{pc}^{-3}$) before the gas expulsion, so that densities have been large enough for external processes to substantially shape the currently visible disc frequency.

Another consequence of the gas expulsion is that the large fraction of stars, that are expelled into the field, remain surrounded by a circumstellar discs. This suggests a higher probability of planetary systems around stars in the field than in stellar clusters. In this context, Gilliland *et al.* (2000) performed extensive observations of 34 000 stars in the 13 Gyr old cluster 47 Tucanae but found no evidence for planetary systems, which was contrary to what has been expected according to its present stellar density. Despite the general explanations like crowding or a low metallicity of the cluster (Weldrake *et al.*, 2005) the present results emphasise that these clusters have been much more compact with most of today observed stars having formed much closer to the cluster center so that the cluster expansion itself provides an additional, non-negligible effect for the absence of planetary systems and promotes an early on destruction of the discs.

Concludingly, the present results provide valuable information for the further interpretation of observational data from upcoming telescopes. The *Atacama Large Millimeter Array* in Chile, which just recently started operating, and the *James Webb Space Telescope* to be launched in 2018 will both provide unprecedented high-resolution data that will for the first time allow a detailed mapping of protoplanetary discs. In particular, a qualitatively and quantitatively enhancement of observational samples of circumstellar disc in massive clusters might provide new insights in the dynamical cluster evolution.

7 Summary

In this study the relevance of star-disc encounters in massive star clusters during the crucial first 15 Myr after their formation has been investigated. The emphasise of the investigation was on the influence of the initial disc-mass distribution and the cluster expansion phase after the gas expulsion process. The most relevant results are the following:

1. Performing a parameter study of individual star-disc encounters, significant differences between the investigated disc-mass distributions were only found for interactions with high-mass stars that mainly perturbed the outer parts of the disc. In addition it was found that independent of the initial distribution encounters may produce steep density profiles of $p > 2$ as possibly required for the formation of planetary systems like our own Solar System.

2. Nevertheless, the simulations of the early embedded phase demonstrated that the fraction of disc-less stars is largely unaffected by the initial disc-mass distribution. Only for very high cluster densities differences become apparent with 60% of discs being destroyed in case of initially constant disc-mass distributions while for initially steep disc-mass distributions ($\Sigma \propto r^{-7/4}$) only 40% are destroyed. The reason is that in very dense clusters stellar interactions interactions of low-mass stars dominate, which show the largest dependency on the initial disc-mass distribution due to the generally high encounter mass ratios.

3. After the expulsion of the residual gas the stellar density drops rapidly and the initial core region of the cluster spreads by about a factor of ten. As a result, star-disc encounters are only prominent during the first few 10^5 yr after gas expulsion. In this phase the initial disc-mass distribution is of minor importance for the results, since usually no discs are destroyed and the total number of encounters is sufficiently low. Preferentially stars from the outer cluster regions become unbound during the expulsion process and are, thus, to a much lower degree affected by encounters.

4. The rapid expansion of the star clusters mimics a drop in the observed cluster disc frequency, which has so far been largely neglected when comparing disc fractions in different clusters. Furthermore, observations of the cluster disc fraction in populations older than 3 Myr likely provide strong upper limits for the survivability of

circumstellar discs since the large fraction of disc-surrounded stars is expelled from the cluster. Consequently, the formation of planetary systems is benefited around stars in the field population.

A Analytical investigations of star formation efficiencies

Hills (1980) analysed the evolution of the total cluster energy during the gas expulsion phase. If the system is assumed to be in a virialised state before gas expulsion the virial theorem is given by $2T_0 + W_0 = 0$, with initial kinetic energy $T_0 = \frac{1}{2} M_{\rm tot} \left\langle \sigma_0^2 \right\rangle$ and initial potential energy $W_0 = GM_{\rm tot}^2/2R_0$. Here, $M_{\rm tot} = M_{\rm stars} + M_{\rm gas}$ represents the initial total mass of the cluster and R_0 the effective cluster radius. If a system of equal mass stars is assumed, R_0 would be obtained by the mean distance between each pair of stars in the cluster. The velocity dispersion prior to the gas mass loss is obtained as

$$\left\langle \sigma_0^2 \right\rangle = GM_{\rm tot}/2R_0. \tag{A.1}$$

The total energy instantaneously after gas expulsion is given by

$$E = T + W = \frac{1}{2}\left[M \left\langle \sigma_0^2 \right\rangle - \left(\frac{GM^2}{R_0} \right) \right] = \frac{1}{2}\left[\epsilon M_{\rm tot} \left\langle \sigma_0^2 \right\rangle - \left(\frac{G\epsilon^2 M_{\rm tot}^2}{R_0} \right) \right], \tag{A.2}$$

where $\epsilon = M/(M_{\rm stars} + M_{\rm gas}) = M/M_{\rm tot}$ is the star formation efficiency of the cluster, M defines the cluster mass after the gas is expelled. If an adiabatic gas expulsion process, on timescales larger than the crossing time, is assumed, the cluster will remain in a virial equilibrium state with the stars adapting to the reduced gravitational potential. However, if the gas is expelled instantaneously the velocity dispersion will be similar to the primordial dispersion before gas expulsion.

If the new state of equilibrium is reached, the total energy is given by

$$E = -W/2 = -\frac{GM^2}{4R}., \tag{A.3}$$

where R is the new equilibrium cluster radius. Combining Equation A.1, A.2, and A.3 results in

$$\frac{R}{R_0} = \frac{1}{\epsilon} \tag{A.4}$$

in case of a gradual gas mass loss while rapid gas expulsion leads to

$$\frac{R}{R_0} = \frac{\epsilon}{2\epsilon - 1}. \tag{A.5}$$

It can easily be deduced that in case of an impulsive mass loss a star formation efficiency of $\epsilon > 0.5$ is required for a subsequently bound cluster (see e.g. Hills, 1980, for further details).

Boily & Kroupa (2003a) reviewed the analytical approach by Hills (1980) and showed that the fraction of bound stars is not only a function of the star formation efficiency but also of the initial stellar distribution function $F(r, v)$. The fraction of bound stellar mass $N_{\text{bound}}/N_{\text{total}}$ at radius r is defined as

$$\frac{N_{\text{bound}}}{N_{\text{total}}} = \frac{\int_{v_{e,\star}}^{v_e} F(r,v)\,\mathrm{d}^3v\,v^2\,\mathrm{d}v}{\int_0^{v_e} F(r,v)\,\mathrm{d}^3v\,v^2\,\mathrm{d}v} - 1 = \frac{\int_{v_{e,\star}}^{v_e} f(v)\,v^2\,\mathrm{d}v}{\int_0^{v_e} f(v)\,v^2\,\mathrm{d}v} - 1, \tag{A.6}$$

where v_e and $v_{e,\star}$ are the local escape velocities before and after the gas expulsion, respectively. $f(v)$ is the stellar velocity distribution function defined by the stellar distribution function at constant radius r. Assuming a power-law velocity distribution function of

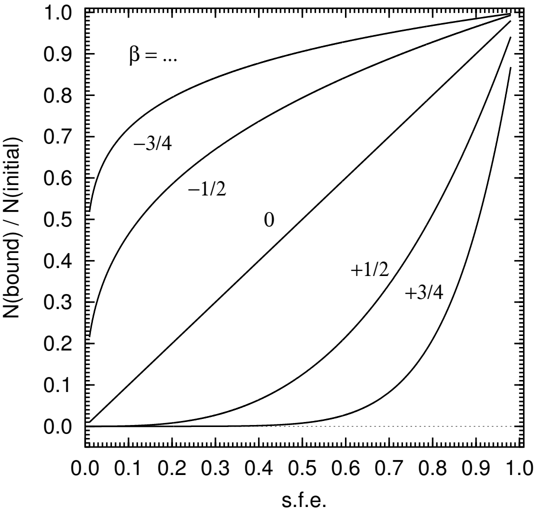

FIGURE A.1: Relative fraction of bound stars as a function of the star formation efficiency for power-law velocity distribution functions with exponent $\beta - 2$. The figure is taken from Boily & Kroupa (2003a).

$$f(v)\,\mathrm{d}^3v \propto v^{\beta-2}\,\mathrm{d}^3v \propto v^{\beta}\,\mathrm{d}v \tag{A.7}$$

the fraction of bound stars can now be calculated by using $v_{e,\star}(r) = \epsilon^{1/2} v_e(r)$ and Equation A.6. For j iterations with $j \rightarrow \infty$ the fraction of bound stars is given by

$$\frac{N_{\mathrm{bound}}}{N_{\mathrm{total}}} = \epsilon^{\frac{1+\beta}{1-\beta}}. \tag{A.8}$$

The dependence of the bound stellar fraction on the exponent β of the stellar velocity distribution is shown in Figure A.1. It can be seen, that the fraction of bound stars decreases rapidly if the velocity distribution is prone to high-velocity stars with $\beta > 0$. In case of a Plummer velocity distribution function Boily & Kroupa (2003a) find a bound fraction of 86% for $\epsilon = 0.5$. However, although a crucial improvement to the investigations of Hills (1980) has been found, numerical simulations are indispensable to obtain proper rates of bound stars (Boily & Kroupa, 2003a,b).

B Numerics of individual star-disc encounters

The Runge-Kutta Cash-Karp Integrator

Since only low-mass discs are investigated in this work, gravitational interactions between the disc particles are neglected, which reduces the simulation effort to $2N+1$ calculations (between the N disc particles and each star as well as between the two stars). In the single star-disc encounter simulations the ordinary differential equations with given initial conditions $y(t_0) = y_0$ have been solved via a Runge-Kutta Cash-Karp integrator as described in Press *et al.* (1992). This integrator is based on the Runge-Kutta method but has been extended by an adaptive time step size control.

In contrast, the Runge-Kutta method propagates a solution over the interval $[t_n, t_n + \Delta t]$ by combining the information from several Euler method steps and then using the information obtained to match a Taylor series expansion up to some higher order. So the approximation for y_{n+1} is given by a weighted average of approximated values of f_k at several time steps within the interval $[t_n, t_n + \Delta t]$ with intermediate values

$$k_i = f(t_n + c_i\Delta t,\, y_n + \sum_{j=1}^{i-1} a_{ij}k_j) \cdot \Delta t \qquad \text{with } i = 1, ..., s. \tag{B.1}$$

The next coordinate of the phase space can now be interpolated by

$$y_{n+1} = y_n + \sum_{i=1}^{s} b_i k_i. \tag{B.2}$$

To specify this particular method, one needs to provide the number of stages s, and the coefficients a_{ij} (for $1 \leq j < i \leq s$), b_i (for $i = 1, 2, ..., s$) and c_i (for $i = 2, 3, ..., s$). These data are usually arranged in a mnemonic device, known as a Butcher tableau (see Fig. B.1).

$$\begin{array}{c|ccccc}
0 & & & & & \\
c_2 & a_{21} & & & & \\
c_3 & a_{31} & a_{32} & & & \\
\vdots & \vdots & & \ddots & & \\
c_s & a_{s1} & a_{s2} & \cdots & a_{s,s1} & \\
\hline
 & b_1 & b_2 & \cdots & b_{s-1} & b_s
\end{array}$$

Figure B.1: Structure of a Butcher tableau.

For example, the fourth-order Runge-Kutta method will lead to

$$\begin{aligned}
k_1 &= \Delta t f(t_n, y_n) \\
k_2 &= \Delta t f(t_n + \frac{\Delta t}{2}, y_n + \frac{k_1}{2}) \\
k_3 &= \Delta t f(t_n + \frac{\Delta t}{2}, y_n + \frac{k_2}{2}) \\
k_4 &= \Delta t f(t_n + \Delta t, y_n + k_3) \\
\Rightarrow y_{n+1} &= y_n + \frac{k_1}{6} + \frac{k_2}{3} + \frac{k_3}{3} + \frac{k_4}{6} + \mathcal{O}(h^5).
\end{aligned}$$

where k_i with $i = 1, 2, 3, 4$ are the intermediate steps and y_{n+1} is the approximation for time step t_{n+1}.

This integrator is much more expensive in computation time than the Euler method, yet leads to much smaller errors and therefore to stable orbits of the particles.

Adaptive time step control

As already mentioned in Section 2.1.1 a time step control can significantly enhance the computational effort of an inhomogeneous system and at the same time maintain a certain accuracy of the simulation code. A high order integrator, using an adaptive time step scheme, is given by the Runge-Kutta Cash-Karp integrator (*RKCK*), which combines a fifth- and fourth-order method to obtain an error estimate. Moreover, it uses six function evaluations to calculate fourth- and fifth-order accurate solutions. The difference between these solutions provides the error estimate of the fourth order solution which is very convenient for adaptive step size integration algorithms. If the error exceeds a specific value the integration can be repeated with a smaller time step, which is derived from the error estimate.

The corresponding Butcher tableau is shown in Fig. B.2 where the first row of b coefficients (see configuration of a Butcher tableau in Fig. B.1) gives the fifth-order accurate

$$\begin{array}{c|cccccc}
0 & & & & & & \\
\frac{1}{5} & \frac{1}{5} & & & & & \\
\frac{3}{10} & \frac{3}{40} & \frac{9}{40} & & & & \\
\frac{3}{5} & \frac{3}{10} & -\frac{9}{10} & \frac{6}{5} & & & \\
1 & -\frac{11}{54} & \frac{5}{2} & -\frac{70}{27} & \frac{35}{27} & & \\
\frac{7}{8} & \frac{1631}{55296} & \frac{175}{512} & \frac{575}{13824} & \frac{44275}{110592} & \frac{253}{4096} & \\
\hline
 & \frac{37}{378} & 0 & \frac{250}{621} & \frac{125}{594} & 0 & \frac{512}{1771} \\
 & \frac{2825}{27648} & 0 & \frac{18575}{48384} & \frac{13525}{55296} & \frac{277}{14336} & \frac{1}{4}
\end{array}$$

FIGURE B.2: Butcher tableau for a *RKCK* integrator.

solution z_{n+1}, and the second row indicates the fourth-order solution y_{n+1}. The error estimate is given by

$$\Delta_i = z_{n+1} - y_{n+1} = \sum_{i=1}^{6} (b_{zi} - b_{yi}) k_i, \tag{B.3}$$

where Δ scales as $(\Delta t)^5$. If a step size Δt_1 is taken, which produces an error of Δ_1, the step size Δt_0, that would produce another error Δ_0, can be estimated as

$$\Delta t_0 = \Delta t_1 \left| \frac{\Delta_0}{\Delta_1} \right|^{1/5}. \tag{B.4}$$

The desired accuracy can now be denoted by Δ_0. On the one hand, if Δ_1 is larger than Δ_0 in magnitude, the equation tells how much to decrease the step size for retrying the present step, on the other hand, if Δ_1 is smaller than Δ_0, the equation tells how much the step size can be safely increased for the next step. In particular, the accuracy is adjusted to the strength of the particle interaction, which is in the performed simulations given by the nearness of the particles relative to the stars, e.g. close particles require a smaller global time step. Here, the minimum step size was set to $\Delta t_{\mathrm{min}} = 0.1\, t_{\mathrm{sim}}$ and the maximum to $\Delta t_{\mathrm{max}} = 100\, t_{\mathrm{sim}}$.

One has to note that a reduction of the time step size does not always increase the accuracy because it increases simultaneously the accumulated (round-off) error due to the larger number of integration steps.

The tree method

For the single encounter simulations the method used to adopt the physical problem to the spatial domain is based on the hierarchical tree algorithm originally developed by Barnes & Hut (1986). The technique involves a tree-like hierarchical subdivision of the simulation space into cubic cells, each of which is recursively divided into 2^3 sub-cells or twigs whenever more than one particle is found to occupy the same cell. The process starts from a root cell, which contains all particles, and is successively subdividing the cells until each particle has its own cube and therefore is representing a leaf. For each sub-cell the total mass, the center of mass coordinates, and even higher multipole moments are computed. Since here only gravitational forces are considered odd order multipole moments vanish.

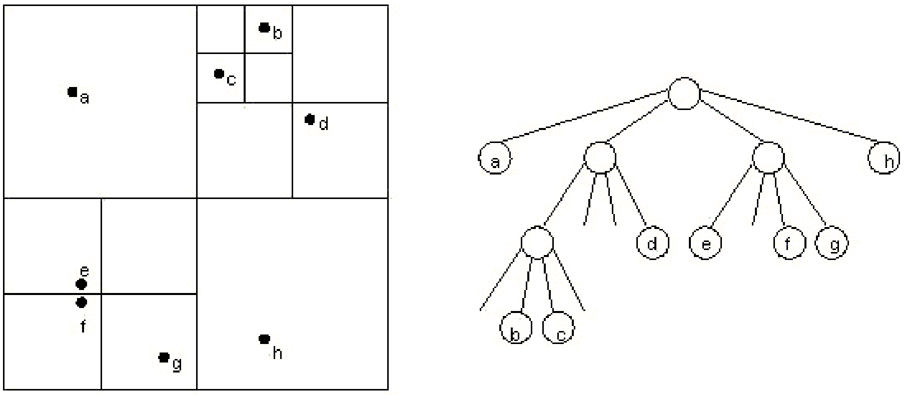

FIGURE B.3: Example of the sub-division of the simulation space (left) and corresponding tree-like structure (right) of Barnes & Hut (1986) with eight bodies.

In the force evaluation step only particles from nearby cells of a particle need to be treated directly, while particles in distant cells are grouped to pseudo-particles located at their center of mass. This can dramatically reduce the number of required force calculations. The force of the pseudo-particles is usually expanded into multipoles so that the accuracy of the algorithm can be controlled via the order of expansion. Other advantages of this method are the freedom from geometrical assumptions and restrictions as well as the applicability to a wide class of systems.

The force on each particle is computed by traversing the tree from the root. The spatial group size r_{group} of particles that are confined to a single pseudo-particle is compared to the spatial distance r_{dist} between the current particle and the pseudo-particle. This occurs via the *Multipole Acceptance Criterion* (MAC),

$$\frac{r_{\text{group}}}{\theta} < r_{\text{dist}}, \tag{B.5}$$

that is controlled by the accuracy parameter θ. If the current particle is more distant than r_{group}/θ, the cell is used to compute the force on the chosen particle. If not, then the algorithm is recursively applied to the cells on the next level (children). The choice of θ determines a compromise between accuracy ($\theta \ll 1$) and computational speed ($\theta \geq 1$). The recommended range of values for the threshold parameter is given by $0.1 < \theta < 1.0$. Larger values will result in low accuracy whereas for a much lower value the scheme will approach the $\mathcal{O}(N^2)$ limit.

In case of a homogeneous distribution the computational effort of this method scales as $\mathcal{O}(N \log N)$, because n divisions of a volume V with N particles are required to place one particle per box of average volume V/N,

$$\frac{V}{N} \sim \frac{V}{8^n} \Rightarrow 8^n \sim N \Rightarrow n \sim \frac{\log N}{\log 8} \sim \log N \ . \tag{B.6}$$

In this work the Treecode is not used to investigate particle-particle interactions, because these can be neglected due to the low-mass of the concerned discs, but the effects of the disc particles on the stars are calculated by this method as they are altering the orbit of the stars. For more details of the implementation of the code see Pfalzner & Gibbon (1996).

C Stellar number density profiles

The choice of an initial density profile after the gas expulsion is not straight forward due to the rapid evolution and limited observations. An isothermal density distribution function as used for the embedded clusters seems misrepresenting since encounters in the early lifetime of the clusters significantly change the profiles within these first Myr of the embedded phase, as demonstrated in Section 4.2. The mostly used distribution functions for observations and numerical models are described in the following.

Plummer model

Plummer (1911) showed that stellar density profiles of observed globular clusters can be fitted by a potential, today known as *Plummer potential*, which is given by

$$\phi(r) = -\frac{GM_{\text{cluster}}}{a}\left(1+\frac{r^2}{a^2}\right)^{-1/2} \tag{C.1}$$

with gravitational constant G, total mass of the cluster M_{cluster}, and the Plummer scale length a, which defines the size of the inner core. Furthermore, a is related to the half-mass radius by $r_{\text{rm}} \approx 1.305a$. The according Plummer density distribution is given by

$$\rho_{\text{Plummer}}(r) = \frac{3M_{\text{cluster}}}{4\pi a^3}\left(1+\frac{r^2}{a^2}\right)^{-5/2}. \tag{C.2}$$

Such Plummer potentials represent globular clusters that are up to several Gyrs (!) old, they are not necessarily a good description for younger clusters. Nevertheless, it is one of the most common used stellar cluster models to sample stellar distributions of any stellar age because of its simplicity (e.g. Aarseth *et al.*, 1974; Kroupa *et al.*, 2001; Goodwin & Bastian, 2006; Bastian & Goodwin, 2006; Baumgardt & Kroupa, 2007; Allison *et al.*, 2009; Brasser *et al.*, 2012).

King model

Another often used model is the set of so-called King models. They were first introduced by Michie & Bodenheimer (1963) and intensively discussed in King (1962) and King (1966) who use them to fit old globular clusters like it was done by Plummer (1911). The idea is based on the model of the isothermal spheres but considers a finite tidal radius of the cluster r_{tide}, beyond which the cluster ceases. It is called tidal radius because for distances $r > r_{\mathrm{tide}}$ from the cluster center, the tidal forces of the hosting galaxy are able to remove stars from the cluster. The energy distribution function of the King model in dependence of the relative energy $\varepsilon = \Phi - 1/2v^2$ and relative potential energy of the particles $\Psi = -\Phi + \Phi_0$ is given by

$$f_{\mathrm{King}}(\varepsilon) = \begin{cases} \rho_1 (2\pi\sigma_K^2)^{-3/2} (e^{\varepsilon/\sigma_K^2} - 1) & \varepsilon > 0; \\ 0 & \varepsilon \leq 0 \end{cases} \tag{C.3}$$

which represents the distribution function of an isothermal sphere but less dense at large cluster radii, where ε is small. The distribution function can be integrated over the stellar velocities to obtain the density in dependence of the relative King cluster potential $\Psi(r)$

$$\rho_{\mathrm{King}}(\Psi(r)) = \rho_1 \left[e^{\Psi(r)/\sigma_K^2} \mathrm{erf}\left(\frac{\sqrt{\Psi(r)}}{\sigma_K} \right) - \sqrt{\frac{4\Psi(r)}{\pi\sigma_K^2}} \left(1 + \frac{2\Psi(r)}{3\sigma_K^2} \right) \right], \tag{C.4}$$

where σ_K is the King velocity dispersion and erf the error function. For setting up a cluster with a King density distribution ρ_{King} one needs to numerically integrate the Poisson equation for $\Psi(r)$ (see Binney & Tremaine, 2008, for a complete introduction into King models).

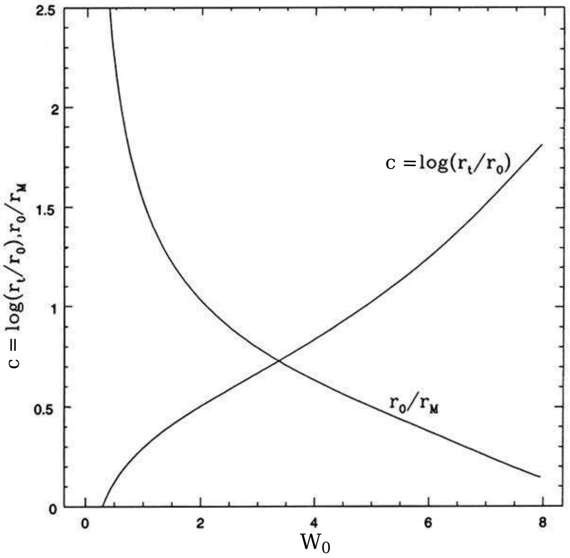

FIGURE C.1: King concentration parameter c and King radius r_0 relative to half-mass radius as a function of the dimensionless King Parameter W_0 adapted from Vesperini (1994).

Furthermore, the King models can be parametrised by their concentration $c = \log_{10}(r_{\mathrm{tide}}/r_0)$ or the ratio of

$$W_0 = \frac{\Psi(0)}{\sigma_K}, \tag{C.5}$$

with the King radius of the cluster given by

$$r_0 = \sqrt{\frac{9\sigma_K^2}{4\pi G\rho_0}}, \tag{C.6}$$

which defines the size of the core of the model. The relation between the King concentration c and the King parameter W_0 is plotted in Figure C.1.

The advantage of the King models hereby is that the King parameter W_0 can now be chosen according to the desired cluster type. For a high King parameter W_0 (or concentration c) a rather flat distribution in the core region and a quick drop in density at the outer cluster region is obtained, making such King models an ideal candidate to fit observed surface brightness profiles of old globular clusters (King, 1962, 1966). Moreover, Plummer models can even be approximated by a King model with King parameter $W_0 = 4$. In the limit $W_0 \to \infty$ ($c \to \infty$) the King models converge to the isothermal sphere model.

D Gas expulsion models

Varying background potential

One further approach to simulate a surrounding gas cloud is the implementation of a background potential, which increases the total potential energy of the cluster. In NBODY6 this has been done by implementing a constant background Plummer profile, which depends on the initial gas mass m_{gas} and the Plummer radius a (a detailed description of Plummer density profiles is given in Appendix C). However, after a reasonable time span the gas is expelled from the cluster, thus, the background potential has to decrease after a predefined time delay t_{delay}. Furthermore, the expulsion is not inevitably instantaneous but might be elongated over several crossing times. Geyer & Burkert (2001) assumed a linear decay of the external gas potential by a time-dependent multiplier

$$\xi = \begin{cases} 1 & t < t_{\mathrm{delay}} \\ 1 - c \cdot (t - t_{\mathrm{delay}})/t_{\mathrm{exp}} & t_{\mathrm{delay}} < t < t_{\mathrm{delay}} + t_{\mathrm{exp}} \;, \\ 0 & t > t_{\mathrm{delay}} + t_{\mathrm{exp}} \end{cases} \tag{D.1}$$

where t_{exp} is the time scale for the expulsion process and $c = 1$ in their study.

There are two intuitive methods to truncate the gas profile, i.e. to simulate the expulsion of the gas: (i) a temporally varying gas mass $m_{\mathrm{gas}}(t)$, which is consistent with the approach of Geyer & Burkert (2001), as well as (ii) a spatially evolving gas model $a(t)$. So far there are no science-based restrictions for the profile of the gas loss. One such approach to define a time-dependent gas mass loss is given by (Eq. D.1)

$$m_{\mathrm{gas}}(t) = m_{\mathrm{gas}}(0) \cdot \xi(t, c) \qquad \text{with } c = 1, \tag{D.2}$$

and a linearly increasing Plummer radius

$$a(t) = a(0) \cdot \xi(t, c) \qquad \text{with } c = -1, \tag{D.3}$$

while e.g. Kroupa *et al.* (2001) assumed an exponential decay of the gas mass and $c = -1/2$ for a time-varying Plummer radius.

Radially-varying star formation efficiency

For simplicity reasons numerical studies use a global star formation efficiency for embedded cluster models. In fact, the star formation efficiency is rather a function of the radius $\epsilon_{\mathrm{SFE}} := \epsilon(r)$, with a higher star formation efficiency in the central cluster regions.

Recently, Parmentier & Pfalzner (2012) analysed the evolution of the local star formation efficiency ϵ_{SFE} in young clusters as a function of the cluster age and the local gas density (radius). Assuming the cluster as a symmetric sphere, its initial volume density ρ_0 is given by

$$\rho_0(r) = \frac{3-p_0}{4\pi} \frac{M_{\mathrm{tot}}}{R_{\mathrm{tot}}^{3-p_0}} r^{-p_0} \tag{D.4}$$

with total cluster mass M_{tot} ($= M_{\mathrm{gas}}$ initially), cluster radius R_{tot}, and density distribution index $p_0 \in [1.4, 2.2]$ (Beuther *et al.*, 2002; Mueller *et al.*, 2002; Pirogov, 2009).

The spherical molecular cloud can be discretised into infinitesimal mass shells. The mass of these shells can be described by

$$dm_{\mathrm{gas}}(t_i, r) = dm_{\mathrm{gas}}(t_{i-1}, r) - \epsilon_{ff} \cdot \frac{t_i - t_{i-1}}{\tau_{ff}(t_{i-1}, r)} \cdot dm_{\mathrm{gas}}(t_{i-1}, r) \tag{D.5}$$

$$dm_{\mathrm{star}}(t_i, r) = dm_{\mathrm{star}}(t_{i-1}, r) + \epsilon_{ff} \cdot \frac{t_i - t_{i-1}}{\tau_{ff}(t_{i-1}, r)} \cdot dm_{\mathrm{gas}}(t_{i-1}, r), \tag{D.6}$$

where the initial shell mass is assumed to be $dm_0(0, r) = dm_{\mathrm{gas}}(t, r) + dm_{\mathrm{star}}(t, r)$ for any time step t and shell radius r. $dm_{\mathrm{gas}}(t, r)$ is the gas mass of an infinitesimal shell and $dm_{\mathrm{star}}(t, r)$ the stellar mass fraction, respectively. The star formation efficiency per free-fall time ϵ_{ff}, which gives the fraction of gas mass that is turned into stars per local free-fall time $\tau_{ff}(t, r)$, is defined constant while the local free-fall time is density-dependent, given by

$$\tau_{ff}(t, r) = \sqrt{\frac{3\pi}{32G\rho_{\mathrm{gas}}(t, r)}}. \tag{D.7}$$

The star formation in the center of the cloud proceeds much faster than in the outer parts due to the much denser natal gas. Here, this yields a steeper density profile of the stars than in the case of the initial molecular cloud. The dependence of ρ_{gas} on the evolved time is due to the depletion of the surrounding gas resulting in a deceleration of the star formation process.

Equations D.5 and D.6 are first order differential equations which translate to

$$\frac{\partial \rho_{\mathrm{gas}}(t, r)}{\partial t} = -\frac{\epsilon_{ff}}{\tau_{ff}(t, r)} \rho_{\mathrm{gas}}(t, r) \tag{D.8}$$

$$\frac{\partial \rho_{\mathrm{star}}(t,r)}{\partial t} = \frac{\epsilon_{ff}}{\tau_{ff}(t,r)} \rho_{\mathrm{gas}}(t,r). \tag{D.9}$$

By using Eq. D.7 and integrating one obtains

$$\rho_{\mathrm{gas}}(t,r) = \left(\rho_0(r)^{-1/2} + \sqrt{\frac{8G}{3\pi}} \cdot \epsilon_{ff} \cdot t \right)^{-2} \tag{D.10}$$

$$\rho_{\mathrm{star}}(t,r) = \rho_0(r) - \left(\rho_0(r)^{-1/2} + \sqrt{\frac{8G}{3\pi}} \cdot \epsilon_{ff} \cdot t \right)^{-2}. \tag{D.11}$$

Finally, this results in a local star formation efficiency of

$$\epsilon_{\mathrm{SFE}}(r) = \frac{\rho_{\mathrm{star}}(r)}{\rho_{\mathrm{star}}(r) + \rho_{\mathrm{gas}}(r)} = 1 - \frac{\left(\rho_0(r)^{-1/2} + \sqrt{\frac{8G}{3\pi}} \cdot \epsilon_{ff} \cdot t \right)^{-2}}{\rho_0(r)}. \tag{D.12}$$

Considering Eq. D.4 the local star formation efficiency in Eq. D.12 now depends only on the initial (total) mass M_{tot}, the cluster radius R_{tot}, the initial gas density distribution index p_0, the star formation efficiency per free-fall time ϵ_{ff}, and the time of evolution t.

Similar to the instantaneous gas expulsion process the virial ratio, given by Eq. 2.32, can be used to implement the radial dependence of the star formation efficiency in NBODY6 by

$$Q(r) = \frac{Q_0}{\epsilon(r)}. \tag{D.13}$$

Due to a subsequently implemented scaling routine the modified velocity profile can in addition be scaled to *arbitrary global* star formation efficiency ϵ.

Bibliography

Aarseth, S. J., 1963, MNRAS **126**, 223.

Aarseth, S. J., 1974, A&A **35**, 237.

Aarseth, S. J., 1985, in *Multiple time scales, p. 377 - 418*, edited by J. U. Brackbill & B. I. Cohen, pp. 377–418.

Aarseth, S. J., 2003, *Gravitational N-Body Simulations* (http://adsabs.harvard.edu/abs/2003gnbs.book.....A).

Aarseth, S. J., M. Henon, & R. Wielen, 1974, A&A **37**, 183.

Adams, F. C., 2000, ApJ **542**, 964.

Adams, F. C., 2010, ARA&A **48**, 47.

Akeson, R. L., D. R. Ciardi, G. T. van Belle, & M. J. Creech-Eakman, 2002, ApJ **566**, 1124.

Alexander, R. D., C. J. Clarke, & J. E. Pringle, 2005, MNRAS **358**, 283.

Alexander, R. D., C. J. Clarke, & J. E. Pringle, 2006, MNRAS **369**, 229.

Allen, P. R., D. W. Koerner, I. N. Reid, & D. E. Trilling, 2005, ApJ **625**, 385.

Allen, R. L., G. M. Bernstein, & R. Malhotra, 2001, ApJ **549**, L241.

Allison, R. J., S. P. Goodwin, R. J. Parker, R. de Grijs, S. F. Portegies Zwart, & M. B. N. Kouwenhoven, 2009, ApJ **700**, L99.

Alonso-Albi, T., A. Fuente, R. Bachiller, R. Neri, P. Planesas, L. Testi, O. Berné, & C. Joblin, 2009, A&A **497**, 117.

Ambartsumian, V. A., 1954, Memoires of the Societe Royale des Sciences de Liege **1**, 293.

Andrews, S. M., & J. P. Williams, 2007a, ApJ **671**, 1800.

Andrews, S. M., & J. P. Williams, 2007b, ApJ **659**, 705.

Ascenso, J., J. Alves, & M. T. V. T. Lago, 2009, A&A **495**, 147.

Balbus, S. A., & J. F. Hawley, 2002, ApJ **573**, 749.

Balog, Z., J. Muzerolle, G. H. Rieke, K. Y. L. Su, E. T. Young, & S. T. Megeath, 2007, ApJ **660**, 1532.

Balog, Z., G. H. Rieke, J. Muzerolle, J. Bally, K. Y. L. Su, K. Misselt, & A. Gáspár, 2008, ApJ **688**, 408.

Barnes, J., & P. Hut, 1986, Nature **324**, 446.

Bastian, N., 2011, in *Stellar Clusters & Associations: A RIA Workshop on Gaia*, pp. 85–97, `1107.2140`.

Bastian, N., B. Ercolano, M. Gieles, E. Rosolowsky, R. A. Scheepmaker, R. Gutermuth, & Y. Efremov, 2007, MNRAS **379**, 1302.

Bastian, N., & S. P. Goodwin, 2006, MNRAS **369**, L9.

Bate, M. R., 2011, MNRAS , 1310`1108.0009`.

Bate, M. R., I. A. Bonnell, & V. Bromm, 2002, MNRAS **336**, 705.

Baumgardt, H., & P. Kroupa, 2007, MNRAS **380**, 1589.

Baumgardt, H., & J. Makino, 2003, MNRAS **340**, 227.

Beuther, H., P. Schilke, K. M. Menten, F. Motte, T. K. Sridharan, & F. Wyrowski, 2002, ApJ **566**, 945.

Binney, J., & S. Tremaine, 2008, *Galactic Dynamics: Second Edition* (Princeton University Press).

Blitz, L., 1993, in *Protostars and Planets III*, edited by E. H. Levy & J. I. Lunine, pp. 125–161.

Boffin, H. M. J., S. J. Watkins, A. S. Bhattal, N. Francis, & A. P. Whitworth, 1998, MNRAS **300**, 1189.

Boily, C. M., & P. Kroupa, 2003a, MNRAS **338**, 665.

Boily, C. M., & P. Kroupa, 2003b, MNRAS **338**, 673.

Bonnell, I. A., & M. B. Davies, 1998, MNRAS **295**, 691.

Borissova, J., V. D. Ivanov, M. M. Hanson, L. Georgiev, D. Minniti, R. Kurtev, & D. Geisler, 2008, A&A **488**, 151.

Bouwman, J., W. A. Lawson, C. Dominik, E. D. Feigelson, T. Henning, A. G. G. M. Tielens, & L. B. F. M. Waters, 2006, ApJ **653**, L57.

Box, G. E. P., & M. E. Muller, 1958, Annals of Mathematical Statistics **29**, 610.

Brasser, R., M. J. Duncan, H. F. Levison, M. E. Schwamb, & M. E. Brown, 2012, ICARUS **217**, 1.

Bressert, E., N. Bastian, R. Gutermuth, S. T. Megeath, L. Allen, N. J. Evans, II, L. M. Rebull, J. Hatchell, D. Johnstone, T. L. Bourke, L. A. Cieza, P. M. Harvey, *et al.*, 2010, MNRAS **409**, L54.

Bronfman, L., L. Nyman, & P. Thaddeus, 1989, in *The Physics and Chemistry of Interstellar Molecular Clouds - mm and Sub-mm Observations in Astrophysics*, edited by G. Winnewisser & J. T. Armstrong, volume 331 of *Lecture Notes in Physics, Berlin Springer Verlag*, pp. 139–140.

Carpenter, J. M., M. H. Heyer, & R. L. Snell, 2000, ApJS **130**, 381.

Carpenter, J. M., E. E. Mamajek, L. A. Hillenbrand, & M. R. Meyer, 2006, ApJ **651**, L49.

Casey, B. W., R. D. Mathieu, L. P. R. Vaz, J. Andersen, & N. B. Suntzeff, 1998, AJ **115**, 1617.

Chabrier, G., 2003a, PASP **115**, 763.

Chabrier, G., 2003b, ApJ **586**, L133.

Chandar, R., S. M. Fall, & B. C. Whitmore, 2006, ApJ **650**, L111.

Chen, H.-C., & C.-M. Ko, 2009, ApJ **698**, 1659.

Chiang, E., & G. Laughlin, 2012, ArXiv e-prints `1211.1673`.

Chiosi, C., & A. Maeder, 1986, ARA&A **24**, 329.

Cieza, L. A., D. L. Padgett, L. E. Allen, C. E. McCabe, T. Y. Brooke, S. J. Carey, N. L. Chapman, M. Fukagawa, T. L. Huard, A. Noriga-Crespo, D. E. Peterson, & L. M. Rebull, 2009, ApJ **696**, L84.

Clarke, C. J., 2007, MNRAS **376**, 1350.

Clarke, C. J., A. Gendrin, & M. Sotomayor, 2001, MNRAS **328**, 485.

Clarke, C. J., & J. E. Pringle, 1993, MNRAS **261**, 190.

Crowther, P. A., O. Schnurr, R. Hirschi, N. Yusof, R. J. Parker, S. P. Goodwin, & H. A. Kassim, 2010, MNRAS **408**, 731.

Currie, T., S. J. Kenyon, Z. Balog, G. Rieke, A. Bragg, & B. Bromley, 2008, ApJ **672**, 558.

Currie, T., & A. Sicilia-Aguilar, 2011, ApJ **732**, 24.

Dale, J. E., B. Ercolano, & I. A. Bonnell, 2012, MNRAS **424**, 377.

Damineli, A., A. Kaufer, B. Wolf, O. Stahl, D. F. Lopes, & F. X. de Araújo, 2000, ApJ **528**, L101.

Desch, S. J., 2007, ApJ **671**, 878.

D'Onghia, E., M. Vogelsberger, C.-A. Faucher-Giguere, & L. Hernquist, 2010, ApJ **725**, 353.

Drake, J. J., B. Ercolano, E. Flaccomio, & G. Micela, 2009, ApJ **699**, L35.

Dullemond, C. P., D. Hollenbach, I. Kamp, & P. D'Alessio, 2007, in *Protostars and Planets V*, edited by B. Reipurth, D. Jewitt, & K. Keil, pp. 555–572.

Duquennoy, A., & M. Mayor, 1991, A&A **248**, 485.

Elmegreen, B. G., 1983, MNRAS **203**, 1011.

Elmegreen, B. G., 2000, ApJ **530**, 277.

Elmegreen, B. G., D. M. Elmegreen, R. Chandar, B. Whitmore, & M. Regan, 2006, ApJ **644**, 879.

Er, X.-Y., Z.-B. Jiang, & Y.-N. Fu, 2009, ChA&A **33**, 139.

Ercolano, B., J. J. Drake, J. C. Raymond, & C. C. Clarke, 2008, ApJ **688**, 398.

Evans, N. J., II, M. M. Dunham, J. K. Jørgensen, M. L. Enoch, B. Merín, E. F. van Dishoeck, J. M. Alcalá, P. C. Myers, K. R. Stapelfeldt, T. L. Huard, L. E. Allen, P. M. Harvey, *et al.*, 2009, ApJS **181**, 321.

Fall, S. M., R. Chandar, & B. C. Whitmore, 2005, ApJ **631**, L133.

Fang, M., R. van Boekel, J. Bouwman, T. Henning, W. A. Lawson, & A. Sicilia-Aguilar, 2013, A&A **549**, A15.

Fellhauer, M., & P. Kroupa, 2005, ApJ **630**, 879.

Fűrész, G., L. W. Hartmann, S. T. Megeath, A. H. Szentgyorgyi, & E. T. Hamden, 2008, ApJ **676**, 1109.

Figer, D. F., 2005, Nature **434**, 192.

Figer, D. F., 2008, in *IAU Symposium*, edited by F. Bresolin, P. A. Crowther, & J. Puls, volume 250 of *IAU Symposium*, pp. 247–256, `0801.4178`.

Figer, D. F., S. S. Kim, M. Morris, E. Serabyn, R. M. Rich, & I. S. McLean, 1999, ApJ **525**, 750.

Figer, D. F., F. Najarro, D. Gilmore, M. Morris, S. S. Kim, E. Serabyn, I. S. McLean, A. M. Gilbert, J. R. Graham, J. E. Larkin, N. A. Levenson, & H. I. Teplitz, 2002, ApJ **581**, 258.

Geyer, M. P., & A. Burkert, 2001, MNRAS **323**, 988.

Gieles, M., N. Moeckel, & C. J. Clarke, 2012, MNRAS **426**, L11.

Giersz, M., & D. C. Heggie, 1994, MNRAS **268**, 257.

Giersz, M., & D. C. Heggie, 1996, MNRAS **279**, 1037.

Gilliland, R. L., T. M. Brown, P. Guhathakurta, A. Sarajedini, E. F. Milone, M. D. Albrow, N. R. Baliber, H. Bruntt, A. Burrows, D. Charbonneau, P. Choi, W. D. Cochran, *et al.*, 2000, ApJ **545**, L47.

Gomes, R., H. F. Levison, K. Tsiganis, & A. Morbidelli, 2005, Nature **435**, 466.

Goodwin, S. P., 1997, MNRAS **284**, 785.

Goodwin, S. P., 2009, Ap&SS **324**, 259.

Goodwin, S. P., & N. Bastian, 2006, MNRAS **373**, 752.

Gorti, U., & D. Hollenbach, 2009, ApJ **690**, 1539.

Grabelsky, D. A., R. S. Cohen, L. Bronfman, & P. Thaddeus, 1988, ApJ **331**, 181.

Greene, 2001, *NASA/JPL* (http://ssc.spitzer.caltech.edu/documents/compendium/galsci/).

Gutermuth, R. A., S. T. Megeath, J. L. Pipher, J. P. Williams, L. E. Allen, P. C. Myers, & S. N. Raines, 2005, ApJ **632**, 397.

Haisch, K. E., Jr., E. A. Lada, & C. J. Lada, 2001a, AJ **121**, 2065.

Haisch, K. E., Jr., E. A. Lada, & C. J. Lada, 2001b, ApJ **553**, L153.

Hall, S. M., 1997, MNRAS **287**, 148.

Hall, S. M., C. J. Clarke, & J. E. Pringle, 1996, MNRAS **278**, 303.

Harfst, S., S. Portegies Zwart, & A. Stolte, 2010, MNRAS **409**, 628.

Hartmann, L., 2003, ApJ **585**, 398.

Hartmann, L., N. Calvet, E. Gullbring, & P. D'Alessio, 1998, ApJ **495**, 385.

Heggie, D., & P. Hut, 2003, *The Gravitational Million-Body Problem: A Multidisciplinary Approach to Star Cluster Dynamics* (Cambridge University Press, 2003, 372 pp.).

Heggie, D. C., 1975, MNRAS **173**, 729.

Heller, C. H., 1993, ApJ **408**, 337.

Heller, C. H., 1995, ApJ **455**, 252.

Hénault-Brunet, V., M. Gieles, C. J. Evans, H. Sana, N. Bastian, J. Maíz Apellániz, W. D. Taylor, N. Markova, E. Bressert, A. de Koter, & J. T. van Loon, 2012, A&A **545**, L1.

Henon, M., 1969, A&A **2**, 151.

Hernández, J., N. Calvet, C. Briceño, L. Hartmann, A. K. Vivas, J. Muzerolle, J. Downes, L. Allen, & R. Gutermuth, 2007, ApJ **671**, 1784.

Hernández, J., L. Hartmann, N. Calvet, R. D. Jeffries, R. Gutermuth, J. Muzerolle, & J. Stauffer, 2008, ApJ **686**, 1195.

Heyer, M., C. Krawczyk, J. Duval, & J. M. Jackson, 2009, ApJ **699**, 1092.

Hillenbrand, L. A., 1997, AJ **113**, 1733.

Hillenbrand, L. A., 2002, ArXiv Astrophysics e-prints `arXiv:astro-ph/0210520`.

Hillenbrand, L. A., & J. M. Carpenter, 2000, ApJ **540**, 236.

Hillenbrand, L. A., & L. W. Hartmann, 1998, ApJ **492**, 540.

Hillenbrand, L. A., S. E. Strom, N. Calvet, K. M. Merrill, I. Gatley, R. B. Makidon, M. R. Meyer, & M. F. Skrutskie, 1998, AJ **116**, 1816.

Hillenbrand, L. A., S. E. Strom, F. J. Vrba, & J. Keene, 1992, ApJ **397**, 613.

Hills, J. G., 1975, AJ **80**, 809.

Hills, J. G., 1980, ApJ **235**, 986.

Hueso, R., & T. Guillot, 2005, A&A **442**, 703.

Ida, S., J. D. Larwood, & A. Burkert, 1999, in *Bulletin of the American Astronomical Society*, volume 31 of *Bulletin of the American Astronomical Society*, pp. 1095–+.

Isella, A., J. M. Carpenter, & A. I. Sargent, 2009, ApJ **701**, 260.

Johnstone, D., D. Hollenbach, & J. Bally, 1998, ApJ **499**, 758.

Johnstone, D., I. Matsuyama, I. G. McCarthy, & A. S. Font, 2004, in *Revista Mexicana de Astronomia y Astrofisica Conference Series*, edited by G. Garcia-Segura, G. Tenorio-Tagle, J. Franco, & H. W. Yorke , volume 22 of *Revista Mexicana de Astronomia y Astrofisica Conference Series*, pp. 38–41, `arXiv:astro-ph/0402655`.

Jones, B. F., & M. F. Walker, 1988, AJ **95**, 1755.

Kaczmarek, T., C. Olczak, & S. Pfalzner, 2011, A&A **528**, A144.

Kennedy, G. M., & S. J. Kenyon, 2009, ApJ **695**, 1210.

Kenyon, S. J., & B. C. Bromley, 2004, Nature **432**, 598.

King, I., 1962, AJ **67**, 471.

King, I. R., 1966, AJ **71**, 64.

Kitamura, Y., M. Momose, S. Yokogawa, R. Kawabe, M. Tamura, & S. Ida, 2002, ApJ **581**, 357.

Kitaura, F. S., H.-T. Janka, & W. Hillebrandt, 2006, A&A **450**, 345.

Kitayama, T., & N. Yoshida, 2005, ApJ **630**, 675.

Klahr, H. H., & P. Bodenheimer, 2003, ApJ **582**, 869.

Kley, W., J. C. B. Papaloizou, & G. I. Ogilvie, 2008, A&A **487**, 671.

Köhler, R., M. G. Petr-Gotzens, M. J. McCaughrean, J. Bouvier, G. Duchêne, A. Quirrenbach, & H. Zinnecker, 2006, A&A **458**, 461.

Kroupa, P., 1995, MNRAS **277**, 1491.

Kroupa, P., 2001, MNRAS **322**, 231.

Kroupa, P., S. Aarseth, & J. Hurley, 2001, MNRAS **321**, 699.

Kruijssen, J. M. D., 2012, MNRAS **426**, 3008.

Kuchner, M. J., 2004, ApJ **612**, 1147.

Kudritzki, R. P., A. Pauldrach, & J. Puls, 1987, A&A **173**, 293.

Kudryavtseva, N., W. Brandner, M. Gennaro, B. Rochau, A. Stolte, M. Andersen, N. Da Rio, T. Henning, E. Tognelli, D. Hogg, S. Clark, & R. Waters, 2012, ApJ **750**, L44.

Kustaanheimo, P., & E. Stiefel, 1965, Journal für die Reine und Angewandte Mathematik **218**, 204.

Lada, C. J., & E. A. Lada, 2003, ARA&A **41**, 57.

Lada, C. J., M. Lombardi, & J. F. Alves, 2010, ApJ **724**, 687.

Lada, C. J., M. Margulis, & D. Dearborn, 1984, ApJ **285**, 141.

Lada, C. J., A. A. Muench, K. E. Haisch, Jr., E. A. Lada, J. F. Alves, E. V. Tollestrup, & S. P. Willner, 2000, AJ **120**, 3162.

Lada, C. J., A. A. Muench, E. A. Lada, & J. F. Alves, 2004, AJ **128**, 1254.

Lada, C. J., A. A. Muench, K. L. Luhman, L. Allen, L. Hartmann, T. Megeath, P. Myers, G. Fazio, K. Wood, J. Muzerolle, G. Rieke, N. Siegler, *et al.*, 2006, AJ **131**, 1574.

Lada, C. J., E. T. Young, & T. P. Greene, 1993, ApJ **408**, 471.

Lada, E. A., 1999, in *NATO ASIC Proc. 540: The Origin of Stars and Planetary Systems*, edited by C. J. Lada & N. D. Kylafis, p. 441.

Lamers, H. J. G. L. M., & J. P. Cassinelli, 1999, *Introduction to Stellar Winds* (http://adsabs.harvard.edu/abs/1999isw..book.....L).

Larson, R. B., 1990, in *Physical Processes in Fragmentation and Star Formation*, edited by R. Capuzzo-Dolcetta, C. Chiosi, & A. di Fazio, volume 162 of *Astrophysics and Space Science Library*, pp. 461–463.

Larson, R. B., 2003, Reports on Progress in Physics **66**, 1651.

Larson, R. B., 2009, ArXiv e-prints `0901.4325`.

Larwood, J. D., 1997, MNRAS **290**, 490.

Lay, O. P., J. E. Carlstrom, & R. E. Hills, 1997, ApJ **489**, 917.

Leisawitz, D., F. N. Bash, & P. Thaddeus, 1989, ApJS **70**, 731.

Lin, D. N. C., & J. E. Pringle, 1990, ApJ **358**, 515.

Lin, S.-Y., N. Ohashi, J. Lim, P. T. P. Ho, M. Fukagawa, & M. Tamura, 2006, ApJ **645**, 1297.

Luhman, K. L., L. E. Allen, P. R. Allen, R. A. Gutermuth, L. Hartmann, E. E. Mamajek, S. T. Megeath, P. C. Myers, & G. G. Fazio, 2008, ApJ **675**, 1375.

Luhman, K. L., E. E. Mamajek, P. R. Allen, & K. L. Cruz, 2009, ApJ **703**, 399.

Luhman, K. L., & O'Dell, 2000, NASA `http://hubblesite.org/newscenter/newsdesk/archive/releases/2000/19`.

Makino, J., 1991, ApJ **369**, 200.

Makino, J., & S. J. Aarseth, 1992, PASJ **44**, 141.

Mamajek, E. E., 2009, in *American Institute of Physics Conference Series*, edited by T. Usuda, M. Tamura, & M. Ishii, volume 1158 of *American Institute of Physics Conference Series*, pp. 3–10, `0906.5011`.

Massey, P., & D. A. Hunter, 1998, ApJ **493**, 180.

Massi, F., E. di Carlo, C. Codella, L. Testi, L. Vanzi, & J. I. Gomes, 2010, A&A **516**, A52+.

Mathieu, R. D., 1983, ApJ **267**, L97.

Matsuyama, I., D. Johnstone, & L. Hartmann, 2003, ApJ **582**, 893.

Matzner, C. D., 2002, ApJ **566**, 302.

McCaughrean, M. J., & C. R. O'dell, 1996, AJ **111**, 1977.

McCaughrean, M. J., & J. R. Stauffer, 1994, AJ **108**, 1382.

McDonald, M., S. Veilleux, D. S. N. Rupke, R. Mushotzky, & C. Reynolds, 2011, ApJ **734**, 95.

McKee, C. F., & E. C. Ostriker, 2007, ARA&A **45**, 565.

Menten, K. M., M. J. Reid, J. Forbrich, & A. Brunthaler, 2007, A&A **474**, 515.

Meru, F., & M. R. Bate, 2011, MNRAS **410**, 559.

Meyer, M. R., & B. A. Wilking, 2009, PASP **121**, 350.

Michie, R. W., & P. H. Bodenheimer, 1963, MNRAS **126**, 269.

Mitchell, T. R., & G. R. Stewart, 2010, ApJ **722**, 1115.

Moeckel, N., & J. Bally, 2006, ApJ **653**, 437.

Moeckel, N., & I. A. Bonnell, 2009, MNRAS **396**, 1864.

Morbidelli, A., & H. F. Levison, 2004, AJ **128**, 2564.

Morbidelli, A., H. F. Levison, K. Tsiganis, & R. Gomes, 2005, Nature **435**, 462.

Motte, F., & P. André, 2001, A&A **365**, 440.

Mueller, K. E., Y. L. Shirley, N. J. Evans, II, & H. R. Jacobson, 2002, ApJS **143**, 469.

Mundy, L. G., L. W. Looney, W. Erickson, A. Grossman, W. J. Welch, J. R. Forster, M. C. H. Wright, R. L. Plambeck, J. Lugten, & D. D. Thornton, 1996, ApJ **464**, L169+.

Murray, N., 2011, ApJ **729**, 133.

Muto, T., C. A. Grady, J. Hashimoto, M. Fukagawa, J. B. Hornbeck, M. Sitko, R. Russell, C. Werren, M. Curé, T. Currie, N. Ohashi, Y. Okamoto, *et al.*, 2012, ApJ **748**, L22.

Myers, P. C., T. M. Dame, P. Thaddeus, R. S. Cohen, R. F. Silverberg, E. Dwek, & M. G. Hauser, 1986, ApJ **301**, 398.

Nisini, B., S. Antoniucci, T. Giannini, & D. Lorenzetti, 2005, A&A **429**, 543.

Nürnberger, D. E. A., & M. G. Petr-Gotzens, 2002, A&A **382**, 537.

O'dell, C. R., Z. Wen, & X. Hu, 1993, ApJ **410**, 696.

Oey, M. S., & C. J. Clarke, 2005, ApJ **620**, L43.

Olczak, C., T. Kaczmarek, S. Harfst, S. Pfalzner, & S. Portegies Zwart, 2012, ApJ **756**, 123.

Olczak, C., S. Pfalzner, & A. Eckart, 2008, A&A **488**, 191.

Olczak, C., S. Pfalzner, & A. Eckart, 2010, A&A **509**, A63+.

Olczak, C., S. Pfalzner, & R. Spurzem, 2006, ApJ **642**, 1140.

Olczak, C., R. Spurzem, & T. Henning, 2011, A&A **532**, A119.

Oliveira, J. M., R. D. Jeffries, J. T. van Loon, S. P. Littlefair, & T. Naylor, 2005, MNRAS **358**, L21.

Oliveira, J. M., R. D. Jeffries, J. T. van Loon, & M. T. Rushton, 2006, MNRAS **369**, 272.

Ostriker, E. C., 1994, ApJ **424**, 292.

Palla, F., & S. W. Stahler, 1999, ApJ **525**, 772.

Palla, F., & S. W. Stahler, 2000, ApJ **540**, 255.

Parmentier, G., & S. Pfalzner, 2012, ArXiv e-prints `1211.1383`.

Pfalzner, S., 2003, ApJ **592**, 986.

Pfalzner, S., 2004, ApJ **602**, 356.

Pfalzner, S., 2009, A&A **498**, L37.

Pfalzner, S., 2011, A&A **536**, A90.

Pfalzner, S., 2012, ArXiv e-prints `1210.8255`.

Pfalzner, S., & P. Gibbon, 1996, *Many-Body Tree Methods in Physics* (http://adsabs.harvard.edu/abs/1981csup.book.....H).

Pfalzner, S., & T. Kaczmarek, 2013, A&A, submitted .

Pfalzner, S., T. Kaczmarek, & C. Olczak, 2012, A&A **545**, A122.

Pfalzner, S., & C. Olczak, 2007, A&A **462**, 193.

Pfalzner, S., & C. Olczak, 2008, in *IAU Symposium*, edited by E. Vesperini, M. Giersz, & A. Sills, volume 246 of *IAU Symposium*, pp. 69–70.

Pfalzner, S., C. Olczak, & A. Eckart, 2006, A&A **454**, 811.

Pfalzner, S., J. Tackenberg, & M. Steinhausen, 2008, A&A **487**, L45.

Pfalzner, S., S. Umbreit, & T. Henning, 2005a, ApJ **629**, 526.

Pfalzner, S., P. Vogel, J. Scharwächter, & C. Olczak, 2005b, A&A **437**, 967.

Pirogov, L. E., 2009, Astronomy Reports **53**, 1127.

Plummer, H. C., 1911, MNRAS **71**, 460.

Porras, A., M. Christopher, L. Allen, J. Di Francesco, S. T. Megeath, & P. C. Myers, 2003, AJ **126**, 1916.

Portegies Zwart, S. F., S. L. W. McMillan, & M. Gieles, 2010, ARA&A **48**, 431.

Press, W. H., S. A. Teukolsky, W. T. Vetterling, & B. P. Flannery, 1992, *Numerical recipes in FORTRAN. The art of scientific computing* (Press, W. H. and Teukolsky, S. A. and Vetterling, W. T. and Flannery, B. P.).

Pringle, J. E., 1981, ARA&A **19**, 137.

Raboud, D., & J.-C. Mermilliod, 1998, A&A **333**, 897.

Reipurth, B., M. M. Guimarães, M. S. Connelley, & J. Bally, 2007, AJ **134**, 2272.

Rochau, B., W. Brandner, A. Stolte, M. Gennaro, D. Gouliermis, N. Da Rio, N. Dzyurkevich, & T. Henning, 2010, ApJ **716**, L90.

Salpeter, E. E., 1955, ApJ **121**, 161.

Sandstrom, K. M., J. E. G. Peek, G. C. Bower, A. D. Bolatto, & R. L. Plambeck, 2007, ApJ **667**, 1161.

Scally, A., & C. Clarke, 2001, MNRAS **325**, 449.

Scally, A., C. Clarke, & M. J. McCaughrean, 2005, MNRAS **358**, 742.

Schaller, G., D. Schaerer, G. Meynet, & A. Maeder, 1992, A&AS **96**, 269.

Shakura, N. I., & R. A. Sunyaev, 1973, A&A **24**, 337.

Sharma, S., A. K. Pandey, D. K. Ojha, W. P. Chen, S. K. Ghosh, B. C. Bhatt, G. Maheswar, & R. Sagar, 2007, MNRAS **380**, 1141.

Shu, F. H., F. C. Adams, & S. Lizano, 1987, ARA&A **25**, 23.

Shu, F. H., D. Galli, S. Lizano, A. E. Glassgold, & P. H. Diamond, 2007, ApJ **665**, 535.

Sicilia-Aguilar, A., L. Hartmann, N. Calvet, S. T. Megeath, J. Muzerolle, L. Allen, P. D'Alessio, B. Merín, J. Stauffer, E. Young, & C. Lada, 2006, ApJ **638**, 897.

Solomon, P. M., A. R. Rivolo, J. Barrett, & A. Yahil, 1987, ApJ **319**, 730.

Spitzer, L., 1987, *Dynamical evolution of globular clusters* (http://adsabs.harvard.edu/abs/1987degc.book.....S).

Spitzer, L., Jr., & M. H. Hart, 1971, ApJ **164**, 399.

Stolte, A., W. Brandner, B. Brandl, H. Zinnecker, & E. K. Grebel, 2004, AJ **128**, 765.

Stolte, A., M. R. Morris, A. M. Ghez, T. Do, J. R. Lu, S. A. Wright, C. Ballard, E. Mills, & K. Matthews, 2010, ApJ **718**, 810.

Sundman, K. F., 1912, Acta Math. **36**, 105.

Sung, H., & M. S. Bessell, 2004, AJ **127**, 1014.

Sung, H., J. R. Stauffer, & M. S. Bessell, 2009, AJ **138**, 1116.

Tackenberg, J., 2009, Diploma Thesis, Univ. zu Köln .

Tenorio-Tagle, G., P. Bodenheimer, D. N. C. Lin, & A. Noriega-Crespo, 1986, MNRAS **221**, 635.

Testi, L., A. Natta, D. S. Shepherd, & D. J. Wilner, 2001, ApJ **554**, 1087.

Tsiganis, K., R. Gomes, A. Morbidelli, & H. F. Levison, 2005, Nature **435**, 459.

Umbreit, S., 2001, Diploma Thesis, Univ. Jena .

Verschueren, W., & M. David, 1989, A&A **219**, 105.

Vesperini, E., 1994, *Scuola Normale Superiore* (Ph.D Thesis, Figure taken from `http://ned.ipac.caltech.edu/level5/Sept02/Bertin/Bertin22_2.html`).

Vicente, S., O. Berné, A. G. G. M. Tielens, N. Huélamo, E. Pantin, I. Kamp, & A. Carmona, 2013, ApJ **765**, L38.

Vorobyov, E. I., & S. Basu, 2005, ApJ **633**, L137.

Vorobyov, E. I., & S. Basu, 2007, MNRAS **381**, 1009.

Webb, R. A., B. Zuckerman, I. Platais, J. Patience, R. J. White, M. J. Schwartz, & C. McCarthy, 1999, ApJ **512**, L63.

Weidenschilling, S. J., 1977, Ap&SS **51**, 153.

Weidner, C., & P. Kroupa, 2006, MNRAS **365**, 1333.

Weidner, C., P. Kroupa, D. E. A. Nürnberger, & M. F. Sterzik, 2007, MNRAS **376**, 1879.

Weintraub, D. A., D. Saumon, J. H. Kastner, & T. Forveille, 2000, ApJ **530**, 867.

Weldrake, D. T. F., P. D. Sackett, T. J. Bridges, & K. C. Freeman, 2005, ApJ **620**, 1043.

Whitmore, B. C., R. Chandar, & S. M. Fall, 2007, AJ **133**, 1067.

Whitworth, A., 1979, MNRAS **186**, 59.

Wilking, B. A., M. Gagné, & L. E. Allen, 2008, *Star Formation in the ρ Ophiuchi Molecular Cloud* (Reipurth, B.), pp. 351–+.

Wilner, D. J., P. T. P. Ho, J. H. Kastner, & L. F. Rodríguez, 2000, ApJ **534**, L101.

Wolff, S. C., S. E. Strom, D. Dror, & K. Venn, 2007, AJ **133**, 1092.

Zinnecker, H., & H. W. Yorke, 2007, ARA&A **45**, 481.

Erklärung

“Ich versichere, dass ich die von mir vorgelegte Dissertation selbständig angefertigt, die benutzten Quellen und Hilfsmittel vollständig angegeben und die Stellen der Arbeit – einschließlich Tabellen, Karten und Abbildungen –, die anderen Werken im Wortlaut oder dem Sinn nach entnommen sind, in jedem Einzelfall als Entlehnung kenntlich gemacht habe; dass diese Dissertation noch keiner anderen Fakultät oder Universität zur Prüfung vorgelegen hat; dass sie – abgesehen von unten angegebenen Teilpublikationen – noch nicht veröffentlicht worden ist sowie, dass ich eine solche Veröffentlichung vor Abschluss des Promotionsverfahrens nicht vornehmen werde. Die Bestimmungen der Promotionsordnung sind mir bekannt. Die von mir vorgelegte Dissertation ist von Frau Prof. Dr. Susanne Pfalzner betreut worden.”

Bonn, den 25. März 2013

(Manuel Steinhausen)

Acknowledgements

First and foremost, I would like to express my special thanks and deepest gratitude to Prof. Dr. Susanne Pfalzner for giving me the opportunity to write my PhD dissertation under her supervision. Her constant support and valuable guidance have been a remarkable source of motivation during all this time. I would like to express my gratitude for her invaluable scientific insight, comprehensive knowledge and penetrative approach, that have on all counts shaped my dissertation.

Furthermore, I am sincerely grateful to Prof. Dr. Andreas Eckart, head of the *I. Physikalisches Institut* in Cologne, and Prof. Dr. Karl Menten, head of the *Max-Planck Institut für Radioastronomie* in Bonn, for their hospitality and their financial support. In particular, I would like to thank the Max-Planck Foundation for awarding me with a stipend of the *Max-Planck-Gesellschaft.*

I am indebted to Christina Korntreff, Andreas Breslau, Kirsten Vincke, Anastasia Tsitali and Guang-Xing Li for many enlightening conversations and helpful comments on my work. It was a pleasure to work and socialize with you on a daily basis. Special thanks go to Dr. Thomas Kaczmarek and Dr. Christoph Olczak for their expert advice and instructive suggestions since the start of my studies until today.

I would like to extend my gratitude to the entire *Eckart workgroup* and *Menten workgroup* for the friendly atmosphere and for offering me an insightful glance into the exciting work in their respective fields.

Last but not least, I would like to thank my family, my girlfriend and everyone who supported me in one way or another in the different stages of my research.

Curriculum Vitae

Manuel Steinhausen

Personal Data

Birth Date	Feburary 20th, 1984
Nationality	german
Marital Status	single
Place of birth	Solingen, Germany

Education

Since 05/2011	**Ph.D., Physics** **Max-Planck-Institut für Radioastonomie, Bonn, Germany** Concentrations: Theoretical Astrophysics
01/2010 – 04/2011	**Ph.D., Physics** **University of Cologne, Cologne, Germany** Concentrations: Theoretical Astrophysics
10/2003 – 09/2009	**Diploma, Physics (1,3)** **University of Cologne, Cologne, Germany** **Thesis (1,0):** *'Numercial investigations of star-disc encounters - Analysis of the loss mechanisms in dependence of the disc-mass distribution'*
08/1994 – 06/2003	**Abitur (final secondary-school examinations) (1,6)** **Gymnasium Leichlingen**

Working Experience

08/2008 – 04/2011	**Tutor for bachelor students** I. Physikalisches Institut, University of Cologne
09/2006 – 07/2008	**Student Research Assistant** I. Physikalisches Institut Universität zu Köln Work group of Prof. Dr. Susanne Pfalzner
04/2006 – 03/2007	**Tutor for bachelor students** II. Physikalisches Institut, University of Cologne
08/2006– 09/2006	**Working student** Development and production of high-precision spindles Precise,Am Wallgraben 2,42799 Leichlingen(Germany)

Manuel Steinhausen ---------------- D-50674 Köln
Tel. ---------------- e-mail: mstein@mpifr-bonn.mpg.de

08/2005 – 09/2005	**Working student** Production of insulations for first-class cars Carcoustics,Neuenkamp 8,51381 Leverkusen(Germany)
08/2004	**Working student** Production of first-class car seats C. Hammerstein,42679 Solingen(Germany)
08/2003	**Working student** Production of first-class car seats C. Hammerstein,42679 Solingen(Germany)

Stipends

Since 05/2011	**Ph.D. scholarship of the Max-Planck-Society**

Skills and Qualification

Language Skills	German: native language English: fluent in writing and speech French: basic knowledge
IT-Skills	Operating Systems: Linux, MS Windows Programming: Fortran77, 90 & 2003

Publications

08/2008	Pfalzner, S.; Tackenberg, J.; Steinhausen, M. *'Accretion bursts in young stars driven by the cluster environment'* Astronomy & Astrophysics
11/2011	Steinhausen, M.; Olczak, C.; Pfalzner, S. *'Disc-mass distribution in star-disc encounters'* Astronomy & Astrophysics
in prep.	Breslau, A.; Steinhausen, M.; Pfalzner, S. *'Sizes of protoplanetary discs after star-disc encounters'* Astronomy & Astrophysics

Activities

Associations	Founding member of the Viva Wupper KG e.V. Registered association of carnival (since January 2004)
Additional Interests	Traveling, reading, playing guitar